SAPIENZA
UNIVERSITÀ DI ROMA

SCUOLA DI DOTTORATO "VITO VOLTERRA"
DOTTORATO DI RICERCA IN FISICA– XXIII CICLO

Study of the $pp \to Z \to \mu^+\mu^-$ Process at ATLAS: Detector Performance and First Cross-Section Measurement at 7 TeV

THESIS SUBMITTED TO OBTAIN THE DEGREE OF
DOCTOR OF PHILOSOPHY ("DOTTORE DI RICERCA") IN PHYSICS
DECEMBER 2010

BY

Sara Borroni

Program Coordinator
Prof. Enzo Marinari

Thesis Advisors
Prof. Cesare Bini
Dott. Stefano Rosati

Contents

Chapter 1

Introduction

After many years of development and building, the CERN proton - proton collider LHC is running at the center of mass energy of 7 TeV since March 30th of this year, reaching the peak luminosity of $10^{32}\ cm^{-2}s^{-1}$.

In the next years this accelerator will open a wide range of exploration possibilities, from the precise measurements of Standard Model parameters to the search for new physics phenomena up to the TeV scale. To reach these goals is definitely important first of all to perform the measurement of the well known Standard Model processes, which can be used as standard candles both for the detectors understanding and performance assessment, and the theoretical predictions tuning at a new unexplored energy. Particularly suitable to this extent is the study of the production of the $W^{\pm}$ and Z^0 bosons, because they are copiously produced at LHC and the theoretical predictions, performed at the next-to-next-to-leading order (NNLO) in the perturbation theory have a small uncertainty (about 5%), mainly due to the uncertainty on the Particle Distribution Functions (PDF), which is meant to be reduced with the LHC observations.

Between April and the end of October 2010, the ATLAS experiment have already recorded about 42 pb^{-1} of integrated luminosity of data and the first cross-section measurements of the $W^{\pm}$ and Z^0 bosons have already been performed and more detailed studies are on-going.

This thesis is focused on the study of the $Z \rightarrow \mu^+ \mu^-$ process. As explained in chapter 2, this process is quite interesting. From the detector performance point of view, it can be used to measure from data muon trigger and reconstruction efficiencies. To extract these efficiencies, in the past three years I developed and optimized a method, called *Tag&Probe* , using Monte Carlo simulation. This method is described in chapter 3. In the past few months, with the first ATLAS data, it allowed to measure the muon efficiencies from data for the first time. A data sample of 1.3 pb^{-1} of integrated luminosity has been used and the results have been compared with the MC expectations. This measurement is described in chapter 4.

The efficiencies estimation is also relevant for the cross-section measurement of all processes involving muons. In fact, when comparing the measured cross-section from data with the theoretical expectations, one has to correct for the detector inefficiencies, which at the start-ip are not perfectly reproduced in the simulation. In this thesis, these muon efficiencies have been used for a first data/MC comparison of the $Z \rightarrow \mu^+ \mu^-$ cross-section, both inclusive and differential as a function of the jet multiplicity. This is described in chapter 5.

This measurement, performed with a data sample of an integrated luminosity of 1.3 pb^{-1}, is just the first step towards more detailed studies currently on-going. In this thesis a detector-level data/MC comparison is shown and the cross-sections for a $Z \rightarrow \mu^+ \mu^-$ production in association with 0 to 4 jets are calculated. In the next few weeks the same measurement will be updated using the full 2010 ATLAS data sample.

Chapter 2

Physics and Detectors at LHC

2.1 The Standard Model of Particle Physics

The past century has seen a really big step forward for the elementary particle physics. The Standard Model (SM) has been developed which describes the behavior of matter and its interactions [1]. This theoretical framework managed to give a unified description of strong, electromagnetic and weak interactions but the gravity, describing the matter as point-like spin-1/2 fermions and the interactions as spin-1 *gauge* bosons.

The model is based on the gauge symmetry group

$$SU_c(3) \times SU_L(2) \times U_Y(1) \tag{2.1}$$

where the first factor describes the strong *colour* interactions, carried by 8 gluons, while $SU_L(2) \times U_Y(1)$ is the symmetry group of unified electro-weak interactions, carried by the photon and the Z^0 and $W^\pm$ bosons. The form of the interaction and the dynamics of such bosons is fixed by the gauge symmetry.

In gauge theories all the gauge bosons should be massless, but experimentally the weak $W^\pm$ and Z^0 bosons, have mass. The Standard Model solves this problem introducing a scalar particle, the Higgs boson, which couples to massive particles and gives them masses through a spontaneous symmetry breaking mechanism. To our experimental knowledge there are three families of fermions, each containing two quarks, a charged lepton and a neutrino. Fermion masses are also obtained by the Higgs mechanism through Yukawa couplings between the fermion and the Higgs.

The Standard Model has been extensively tested in the last decades at LEP and Tevatron [2] and it turned out that it successfully explains most of the known phenomena in elementary particle physics. Nevertheless a number of open questions are still left which need for further studies to be done.
There is, for example, evidence that neutrinos have non-zero masses, which the SM does not allow. The measurement of the ordinary matter density in our universe gives a hint that physics even beyond the SM should exist. Astrophysics observations make it clear for example that either our understanding of gravity based on Einstein's theory of General Relativity is wrong, or that particles forming dark matter, which have so far escaped our detection, must exist, and the SM does not furnish any viable candidate. Moreover the observed matter-antimatter asymmetry is not explained in the SM framework.

There also are theoretical motivations for thinking that the SM needs to be extended. One such example is the hierarchy problem concerning the quadratically divergent fermion loop corrections to the Higgs boson mass. New physics is required to happen at the TeV scale to constrain the Higgs mass in the area of a few hundred GeV and thus make the SM consistent with recent W and top mass measurements [3]. The unification of the gauge couplings is something which is aimed but it does not happen in the SM. In addition the unification of gravity with the other forces is still missing.

The *Large Hadron Collider* has been built, with its four experiments, *ATLAS, CMS, LHCb* and *ALICE*, to answer this kind of questions. The composite nature of the proton-proton collisions, despite of the difficult experimental environment which generates, opens a wide range of exploration possibilities, from the precise measurements of Standard Model parameters to the search for new physics phenomena up to the TeV scale.

Nevertheless, all these searches should be preceeded by the measurement of the well known Standard Model processes. These can be used as standard candles both for the detectors understanding and performance assessment, and the theoretical predictions tuning at a new unexplored energy. Particularly suitable to this extent is the study of the production of the $W^\pm$ and Z^0 bosons, because the theoretical predictions have a small uncertainty. They have also been measured at LEP and at Tevatron with big precision.

Being the gauge bosons so relevant for the LHC physics, a deeper look into their production process will be given in the next section, before coming back to the LHC physics program and to the consequent detectors requirements.

2.1.1 $W^\pm$ and Z^0 Bosons Physics: the Drell-Yan process

The Drell-Yan process [4] is likely to be the standard candle which is both theoretically calculable and experimentally measurable with highest accuracy at hadron colliders, in particular at the LHC. It consists in the production of a neutral or charged lepton pair, $\ell\bar{\ell}$ or $\ell\bar{\nu}$, in the collision of two initial hadrons H_1 and H_2:

$$H_1(p_1) + H_2(p_2) \to \ell(k_1) + \bar{\ell}(k_2) + X(q) \qquad \text{(neutral)} \tag{2.2}$$

$$\to \ell(k_1) + \bar{\nu}(k_2) + X(q) \qquad \text{(charged)} \tag{2.3}$$

where p_i are the momenta of the incoming partons, k_i are the momenta of the outgoing partons and X is the entire set of other hadronic objects produced in the event. In the parton model [5], the generic differential cross-section for the process is

$$d\sigma(p_1,p_2) = \sum_{i,j} \int_\tau^1 dx_1 \int_{\tau/x_1}^1 dx_2\; f_i^{(1)}(x_1)\, f_j^{(2)}(x_2)\, d\hat{\sigma}_{ij}(x_1 p_1, x_2 p_2), \tag{2.4}$$

where

- $f_i^{(H)}(x)$ are the parton density functions of parton i in the initial hadron H, carrying a momentum fraction x, and $\tau = M^2/s$

- $d\hat{\sigma}_{ij}(\hat{p}_1, \hat{p}_2)$ is the parton-level cross-section, which depends on the initial parton momenta $\hat{p}_1, \hat{p}_2$ and on the parton species i, j
- the sum extends to all quarks and gluons in the initial hadrons.

The process is sketched in Fig. 2.1. At leading order in both electroweak and QCD

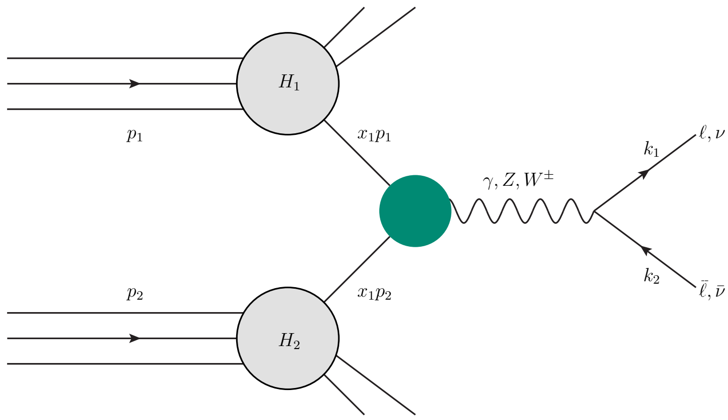

Figure 2.1. The Drell-Yan process at leading order in electroweak interactions. The green ball contains the QCD corrections to the process, including real emissions of gluons.

the partonic process consists of a quark and an antiquark annihilating into a virtual vector boson γ, Z or $W^\pm$, which subsequently decays into the lepton pair. At this order all the available partonic center-of-mass energy $\sqrt{\hat{s}}$,

$$\hat{s} = x_1 x_2 s, \qquad s = (p_1 + p_2)^2, \tag{2.5}$$

goes into the lepton pair invariant mass M,

$$M^2 = (k_1 + k_2)^2. \tag{2.6}$$

When QCD correction on the initial partons are considered, real emission of gluons and quarks must be taken into account, in order to remove infrared divergences coming from virtual corrections. These emissions can be soft (hence undetectable, making this process indistinguishable from the process with no emission) or hard (producing jets). In this case the available partonic center-of-mass energy is no longer equal to the final state mass.

The current QCD theoretical accuracy for this process is NNLO, both for the integrated cross-section [6] and the rapidity-distributions [7]; the impact of threshold resummation at next-to-next-to-leading log (NNLL) level is discussed in Refs. [8, 9].

A large number of events collected at the LHC, combined with a very precise theoretical determination of the process, can be a very useful test of perturbative QCD. Moreover, the high LHC energy will allow for detailed measurements at a previously unexplored kinematic domain of low parton momentum fraction at a high energy scale, significantly improving the precision on the determination of the PDFs.

Besides the measurements of the W and Z boson production cross-sections, the measurement of their ratio R and of the asymmetry between the W^+ and W^- cross sections constitute important tests of the Standard Model. The ratio R can be measured with a higher relative precision since both experimental and theoretical uncertainties partially cancel. With larger data sets this ratio can be used to provide interesting constraints on the W-boson width Γ_W.

From the experimental point of view, the cross-section measurement can be performed in different ways. The *inclusive* measurement is done studying the boson production and decay channel in a certain mass range, no matter what else is produced in the final state. In the following, when nothing else is specified, with Z or W cross-section measurement we refer to the inclusive one. The W and Z boson production cross-section and decay into two leptons (muons and electrons), at $\sqrt{s} = 7$ TeV center of mass energy, are theoretically predicted at the NNLO to be[1]:

$$\sigma_{\text{NNLO}}(W^+ \to l^+\nu) = 6.16 \pm 0.31 \text{ nb} \tag{2.7}$$
$$\sigma_{\text{NNLO}}(W^- \to l^-\bar{\nu}) = 4.30 \pm 0.21 \text{ nb} \tag{2.8}$$
$$\sigma_{\text{NNLO}}(W \to l\nu) = 10.46 \pm 0.52 \text{ nb} \tag{2.9}$$
$$\sigma_{\text{NNLO}}(Z^0 \to l^+l^-) = 0.96 \pm 0.05 \text{ nb} \tag{2.10}$$

where the invariant mass range for the Z is defined between $66 < m_{ll} < 116$ GeV.

Otherwise it is possible to study the boson production in association with some other object in the final state. This is an *exclusive* measurement and it is usually distinguished by the inclusive one just specifying the object in the final state. For example $Z + jets$ means the production of a Z boson in association with jets.
Despite of the fact they are measurements of the same physical process, they are treated separately because they imply different experimental issues to deal with, thus two different analyses.

2.2 Large Hadron Collider and Physics Program

The Large Hadron Collider at CERN will extend the frontiers of particle physics with its unprecedented high energy and luminosity. Inside the LHC, bunches of up to 10^{11} protons will collide 40 million times per second to provide 14 TeV proton-proton collisions at a design luminosity of $10^{34} cm^{-2}s^{-1}$. The LHC will also collide heavy ions, in particular lead nuclei, at 5.5 TeV per nucleon pair, at a design luminosity of $10^{27} cm^{-2}s^{-1}$. The high interaction rates, radiation doses, particle multiplicities and energies, as well as the requirements for precision measurements have set new standards for the design of particle detectors. ATLAS (A Toroidal LHC ApparatuS) is one of the two general purpose detectors that have been built for probing p-p collisions in this environment.

Requirements for the ATLAS detector system [12] have been defined using a set of processes, covering much of the new phenomena which one can hope to observe at the TeV scale.

For example, the top quark will be produced at the LHC at a rate of a few tens of Hz (figure 2.2), providing the opportunity to test its couplings and spin.
The Higgs boson (H) search and the determination of its properties also implies a

[1]Using program FEWZ[7] with the MSTW2008 NNLO structure function parameterisation[11]

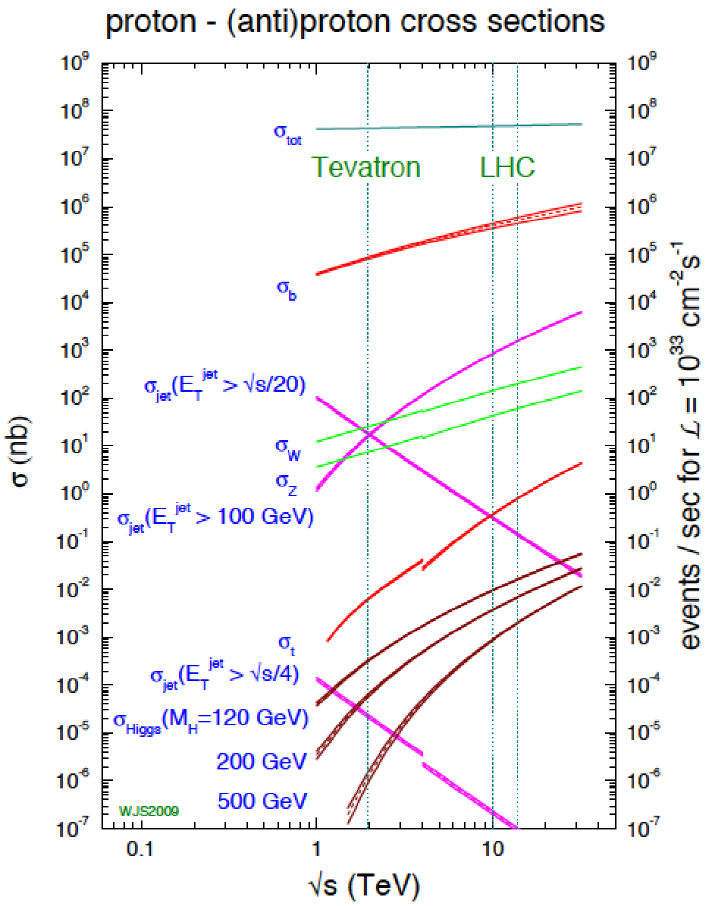

Figure 2.2. Cross-sections of some of the most ineteresting SM processes at Tevatron and LHC.

number of detector requirements, depending on the Higgs mass value.
At low masses ($m_H < 2m_Z$), the natural width would only be a few MeV (figure 2.3), and so the observed width would be defined by the instrumental resolution. The predominant decay mode into hadrons would be difficult to detect due to QCD backgrounds, and the two-photon decay channel would be an important one. Other promising channels could be, for example, the associated production of H such as $t\bar{t}H$, W/ZH with $H \to b\bar{b}$ (figure 2.4), using a lepton from the decay of one of the top quarks or of the vector boson for triggering and background rejection. For masses above 130 GeV, Higgs boson decays, $H \to ZZ^*$, where each Z decays to a pair of oppositely charged leptons (figure 2.5), would provide the experimentally cleanest channel to study the properties of the Higgs boson. For masses above approximately 600 GeV, WW and ZZ decays into jets or involving neutrinos would be needed to extract a signal. The tagging of forward jets from the vector bosons fusion production mechanism has also been shown to be important for the discovery of the Higgs boson. Searches for the Higgs boson beyond the Standard Model, for such particles as the A and $H^{\pm}$ of the minimal supersymmetric extension of the Standard Model, require sensitivity to processes involving τ-leptons and good b-tagging performance. Should the Higgs boson be discovered, it would need to be studied in several modes, regardless of its mass, in order to fully disentangle its properties and establish its credentials as belonging to the Standard Model or an extension.

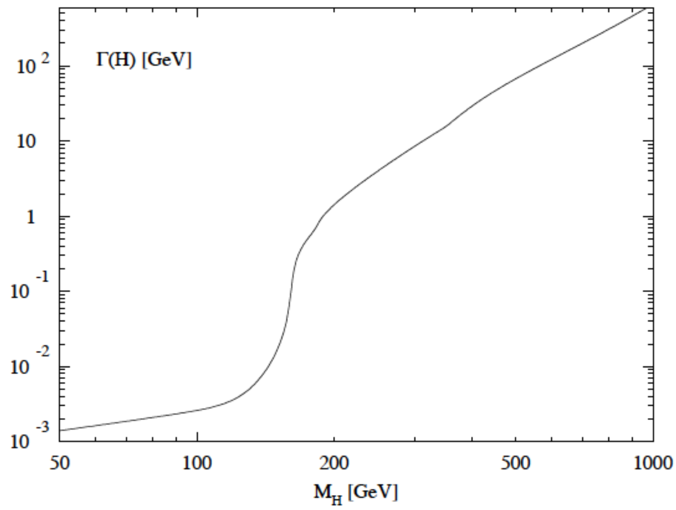

Figure 2.3. Total decay width of the Standard Model Higgs boson as a function of its mass.

New heavy gauge bosons W' and Z' could be accessible for masses up to ~6 TeV. To study their leptonic decays, high-resolution lepton measurements and charge identification are needed in the p$_T$-range of a few TeV. Another class of signatures of new physics may be provided by very high-p$_T$ jet measurements. As a benchmark process, quark compositeness has been used, where the signature would be a deviation in the jet cross-sections from the QCD expectations. Searches for flavour-changing

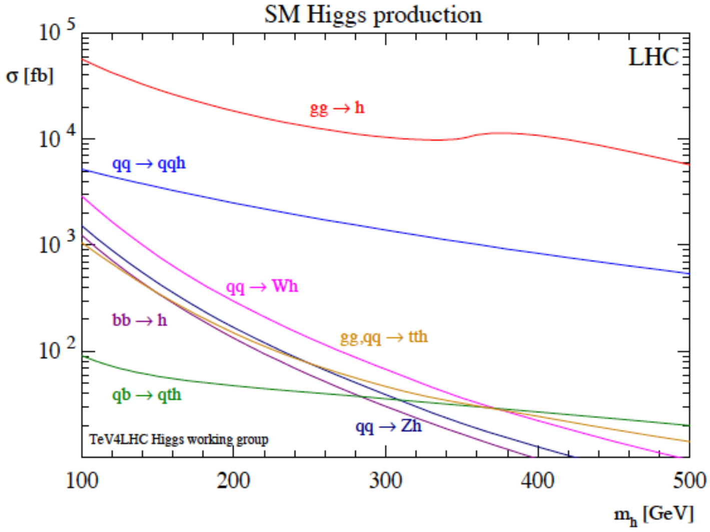

Figure 2.4. Higgs boson production NLO cross-sections at the LHC, $\sqrt{s}$ =14 TeV , for the most relevant production mechanisms as a function of the Higgs boson mass. No branching ratios or acceptance cuts are included.

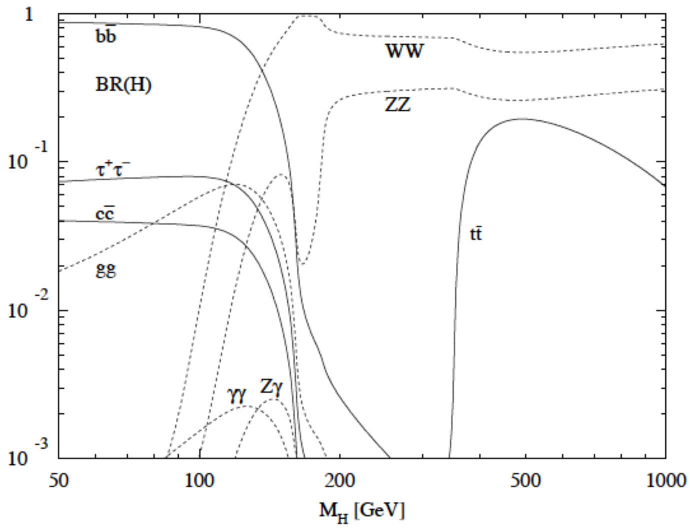

Figure 2.5. Main branching ratios of the Standard Model Higgs decay channels.

neutral currents and lepton flavour violation through $\tau \to 3\mu$ or $\tau \to \mu\gamma$, as well as measurements of $B_s^0 \to \mu\mu$ and triple and quartic-gauge couplings may also open a window onto new physics.

The decays of supersymmetric particles, such as squarks and gluinos, would involve cascades which, if R-parity is conserved, always contain a lightest stable supersymmetric particle (LSP). As the LSP would interact very weakly with the detector, the experiment would measure a significant missing transverse energy, in the final state. The rest of the cascade would result in a number of leptons and jets. In schemes where the LSP decays into a photon and a gravitino, an increased number of hard isolated photons is expected.

The very high LHC luminosity and resulting interaction rate are needed because of the small cross-sections expected for many of the processes mentioned above. However, with an inelastic proton-proton cross-section of about 80 mb, the LHC will produce a total rate of 10^9 inelastic events per second at design luminosity. This is experimentally challenging as it implies that every candidate event for new physics will on the average be accompanied by 23 inelastic events per bunch-crossing.
The nature of proton-proton collisions imposes another difficulty. QCD jet production cross-sections dominate over the rare processes mentioned above, requiring the identification of experimental signatures characteristic of the physics processes in question, such as missing transverse energy or secondary vertices. Identifying such final states for these rare processes imposes further demands on the integrated luminosity needed, and on the particle-identification capabilities of the detector.

2.3 ATLAS Detector

2.3.1 Detector Requirements

To fulfill the illustrated physics requirements, the detector has been designed to have some fundamental characteristics:

- Good charged-particle momentum resolution and reconstruction efficiency are essential. For offline tagging of τ-leptons and b-jets, vertex detectors close to the interaction region are required to observe secondary vertices.

- Very good electromagnetic (EM) calorimetry for electron and photon identification and measurements, complemented by full-coverage hadronic calorimetry for accurate jet and missing transverse energy measurements, are important requirements.

- Good muon identification and momentum resolution over a wide range of momenta and the ability to determine unambiguously the charge of high-p_T muons are also fundamental requirements.

- Highly efficient triggering on low transverse-momentum objects with sufficient background rejection, is a prerequisite to achieve an acceptable trigger rate for most physics processes of interest.

- Due to the experimental conditions fast electronics and high detector granularity are needed to handle the particle fluxes and to reduce the influence of overlapping events.

The ATLAS detector, described in the following, has been designed to fullfil all these requirements

2.3.2 Detector Overview

The ATLAS detector [12] has the typical structure of a collider detector experiment (fig. 2.6). It has a cylindrical multi-layer shape around the beam pipe and it is forward-backward symmetric with respect to the interaction point.

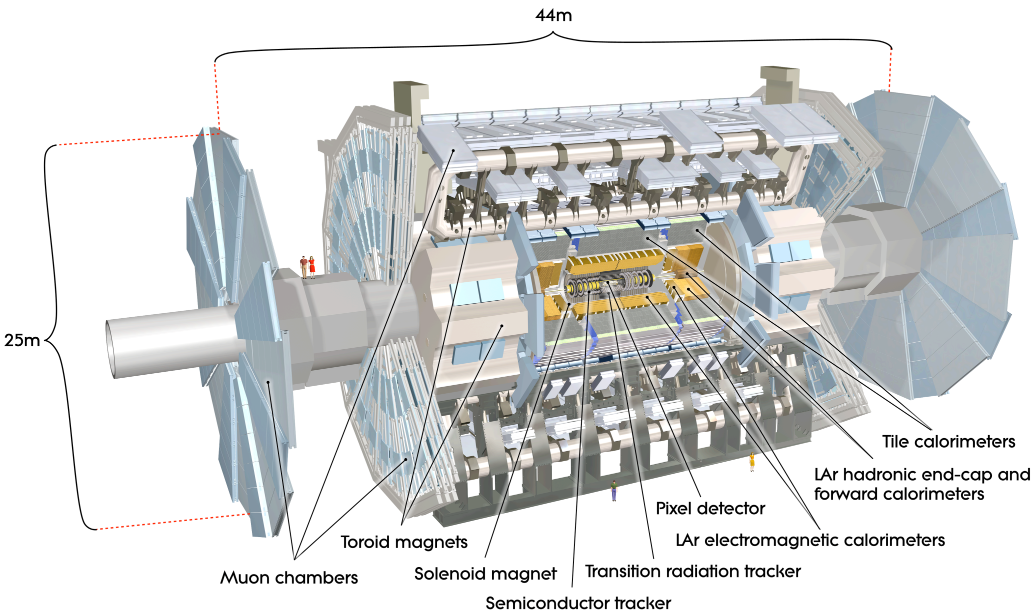

Figure 2.6. Overview of ATLAS detector.

The nominal interaction point is defined as the origin of the coordinate system, while the beam direction defines the z-axis and the x-y plane is transverse to the beam direction. The positive x-axis is defined as pointing from the interaction point to the centre of the LHC ring and the positive y-axis is defined as pointing upwards. The side-A of the detector is defined as that one with positive z and side-C is that one with negative z.
The azimuthal angle ϕ is measured as usual around the beam axis while the polar angle θ is the colatitude with respect to the beam axis. More than θ angle, the rapidity y is used, which is defined as $y = 1/2 \ln\left[(E + p_z)/(E - p_z)\right]$, where E is the overall energy of the particle and p_z is the momentum of the particle in z-direction. The reason to use the rapidity y is that it is an additive quantity under the Lorentz transformations and one expects an approximately uniform particle distribution dN/dy in this variable. In the limit of vanishing masses, the rapidity simplifies to $\eta = \ln\tan(\theta/2)$, the so-called pseudo-rapidity. The distance ΔR between two

reconstructed objects in the pseudorapidity-azimuthal angle space is defined as $\Delta R = \sqrt{\Delta\eta^2 + \Delta\phi^2}$.

Three sub-systems are used to reconstruct different kinds of objects, from the inner to the outer of the detector:

Inner Detector (ID) : tracking and measurement of the charge and the transverse momentum of charged particles;

Calorimetric System : identification of electrons, photons and hadrons and measurement of their energies;

Muon Spectrometer (MS) : identification, tracking and measurement of charge and momentum of muons.

The whole detector is then dipped into two magnetic fields: a central solenoidal one and a toroidal external one. The toroidal field is a unique ATLAS feature, unusual for this kind of experiments. The reasons for this choice will be explained in the next section.

In the following a brief description of the various systems is given. A more detailed description is given of the Muon Spectrometer, being this thesis focused on muon efficiencies measurement.

Finally we note that the hadronic nature of the interactions makes the effective center of mass energy of the colliding partons unknown at each bunch crossing. Nevertheless the transverse momentum component of each parton is generally negligible with respect to the longitudinal one. This means that the total transverse energy, *i.e.* that one defined in the $x - y$ plane, is zero and each event can be fully reconstructed in this plan. This is the reason why *transverse* quantities are used in hadron collider physics rather than the total ones, such as the transverse momentum p_T , the transverse energy E_T, and the missing transverse energy E_{Tmiss}.

2.3.3 Magnet System

The magnet system is used to measure the momentum of the charged particles passing trough the detector. Magnetic fields bend the trajectory of charged particles proportionally to their field strength: a stronger magnetic field implies a stronger bending of the particle tracks, which enhances the precision of the momentum measurement.

To reach the best performance the ATLAS Inner Detector is dipped into a solenoidal magnetic field provided by superconducting NbTi/Cu-magnets cooled down to 4.5 K in a cryostat, which is shared with the calorimeter to minimize the usage of material. This magnet system has a diameter of 2.5 meters and is 5.3 meters long. It is shorter by 80 cm than the Inner Detector, which leads to an inhomogeneous magnetic field over the edge region of the Inner Detector. The field strength is 2 T at the interaction point and 0.5 T at the end of the Inner Detector.

The toroid magnet system instead provides the magnetic field for the Muon Spectrometer. It covers an η-range up to 2.7 and has an average magnetic field strength of 0.5 T. The magnetic field lines are toroidal and perpendicular to the magnetic field of the solenoid magnet system. The magnetic field is created by eight superconducting coils in the barrel and by two toroids with eight coils each in the end-cap region. The inner radius in the barrel region is 5 m, the outer radius is 10.7 m. These large extensions of the magnetic field allow a track measurement with a long lever arm and hence improve the precision of the momentum measurement. The magnet coils are not placed in iron, which would increase the magnetic field strength, but are surrounded by air to minimize multiple scattering effects. This is the reason why the toroid magnet system is also labelled as air-core toroid system.

2.3.4 Inner Detector

The Inner Detector is the closest subsystem to the interaction point. Its primary task is the precise reconstruction of the trajectories (tracks) of charged particles. Knowing the trajectory and the magnetic field in the Inner Detector, one can calculate the charge, the initial momentum, the direction of flight and the impact parameter of charged particles. The impact parameter describes the point of closest approach of the trajectory to the beam line. The design of the Inner Detector must fulfill several requirements to allow an optimal search for rare physics processes. The track reconstruction efficiency of the Inner Detector must be larger than 90%.

The design of the Inner Detector ensures a coverage in η up to 2.5 and a full ϕ-coverage. The transverse momentum resolution is of the order of 1-2 % below $\sim$ 100 GeV and increase up to 30% above. Moreover, the Inner Detector must provide a precise primary and secondary vertex reconstruction, which is important for the identification of B-mesons and converted photons.

The resolution of the Inner Detector can be parameterized by [43]

$$\frac{\Delta p_T}{p_T} \sim 0.00036 \times p_T[GeV] \oplus \frac{0.013}{\sqrt{\sin\theta}}$$

The first term corresponds to the intrinsic resolution, while the second term parameterizes the multiple scattering effects. This has an η dependence due to the increasing material budget in the forward region. The high multiplicity of charged particles per collision, which leads to many overlapping tracks and therefore introduces ambiguities in the track reconstruction, is one of the biggest issues the Inner Detector has to cope with. The idea to minimize this problem is the combination of a high precision measurement of few points and a nearly continuous low precision measurement of many points along the particle trajectory.

Thus, the Inner Detector (fig. 2.7) is built of three subsystems:

The pixel detector has a very high granularity and allows a high precision measurement of three dimensional interaction points along the particle trajectory

The semi conducting tracker (SCT) , measures at least four three dimensional space-points along the trajectory also to high precision

The transition radiation tracker (TRT) , provides on average 36 measurements in the bending plane of the particle

These three subsystems are discussed in the following.

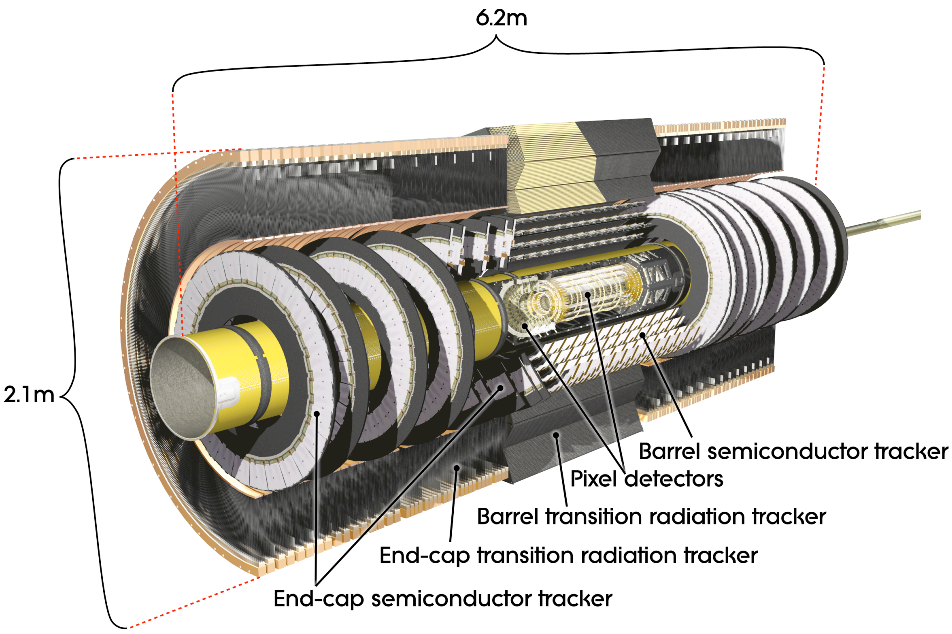

Figure 2.7. Overview of ATLAS Inner Detector

Pixel Detector

The active material of the pixel detector is silicon, which is structured in rectangular cells with a size of $40 \times 400\ \mu m^2$. These cells are called pixels and can be compared to the pixels of a usual digital camera. Charged particles which pass through silicon produce electron hole pairs. A bias voltage, which is applied to each cell, causes the electrons and holes to drift to the readout-side of the cell. The threshold on single cell-level is a charge corresponding to 3000 e^-. The amount of charge above this threshold, which was deposited in one cell, is stored. The cells are placed in three cylindrical layers in the barrel region, with distances to the beam-line of r = 5.05 cm, r = 8.85 cm and r = 12.25 cm. The endcap-region is covered by three disks of cells on each side. The pixel detector has in total 80 million cells, with an efficiency of nearly 100%, which was tested in the H8 test-beam setup [44]. The test-beam measurements revealed an expected resolution of 12 μm in the $r - \phi$ plane and 110 μm in z-direction. This high precision of the pixel detector drives the measurement of the impact parameter of each reconstructed track.

Semi Conducting Tracker

The SCT is responsible for the tracking at radii from 30 cm to 60 cm. It is important for the determination of the z-position of the vertex, the momentum resolution and also for the pattern recognition of the reconstruction algorithms. Silicon was also used here as active material and it is structured in strips with a width of 80 μm. A sensor is formed of 768 strips and covers an area of $6 \times 12\ cm^2$. A SCT module is a combination of the readout-electronic and two sensors, which are glued together with a relative angle of 40 $mrad$. The readout-electronics for one module allows only a binary information from each strip, in contrast to the pixel detector, where also the amount of charges is accessible. This limits the spatial resolution to 23 μm per module. The relative angle between the two sensors allows the measurement of the second coordinate of the sensor's plane to a precision of 800 μm. The 2112 SCT modules are placed in four cylindrical layers in the barrel region and 988 modules in four disks in each endcap-side.

Transition Radiation Tracker

The number of precision layers is constrained by the high cost per unit area of semiconductor layers and their relative high radiation length. Hence it was decided to use a third sub-detector type, for radii larger than 60 cm, which consists of straw tubes with a diameter of 4 mm. These tubes are filled with a gas mixture of $Xe : CO_2 : O_2$ at $70 : 27 : 3$ and have a gold-plated tungsten wire in the middle. Charged particles, which traverse trough the tube, lead to a ionization of the gas mixture. In addition, the walls of the straw tubes contain radiator material (polyethylene) which enhances the production of transition radiation photons. These photons can be detected in Xe-gas. The number of produced photons by a particle is proportional to the relativistic correction factor $\gamma = E/m$ of the particles [45]. Electrons produce most of these photons due to their small mass. This allows an additional identification of electrons. The roughly 50,000 tubes of the TRT, which are arranged in 73 cylindrical layers, provide roughly 36 track points for the track reconstruction. The expected occupancy of 50% of the TRT tubes is challenging for the pattern recognition. Nevertheless, the track points are rather important for the resolution of the Inner Detector, since they are positioned along a relative large level arm.

2.3.5 Calorimetric System

The calorimetric system of ATLAS measures the energy and position of particles by sampling the energy deposit in the calorimeter. The main goal is the identification of photons, electrons and jets with energies from 10 GeV to 1 TeV. Moreover it is used for the determination of missing energy. This requires a large η-coverage of the calorimetric system. The main calorimetric system consists of one barrel and two endcap parts which cover the area up to $|\eta| < 3.2$. A special forward calorimeter is placed at $3.1 < |\eta| < 4.9$, which is resistant against hard radiation coming directly from the proton beam and is used to improve the measurement of the missing transverse energy. The calorimetric system itself has two basic components (fig. 2.8): the inner component is the electromagnetic calorimeter for the measurement of electrons and photons, the outer component is the hadronic calorimeter for the measurement of hadrons.

Electromagnetic Calorimeter

The Electromagnetic Calorimeter (LAr) [13] makes use of the interaction of electrons and photons with matter. The most important effect for electrons at high energies ($E >> m_e c^2$) is bremsstrahlung which leads to the production of an additional

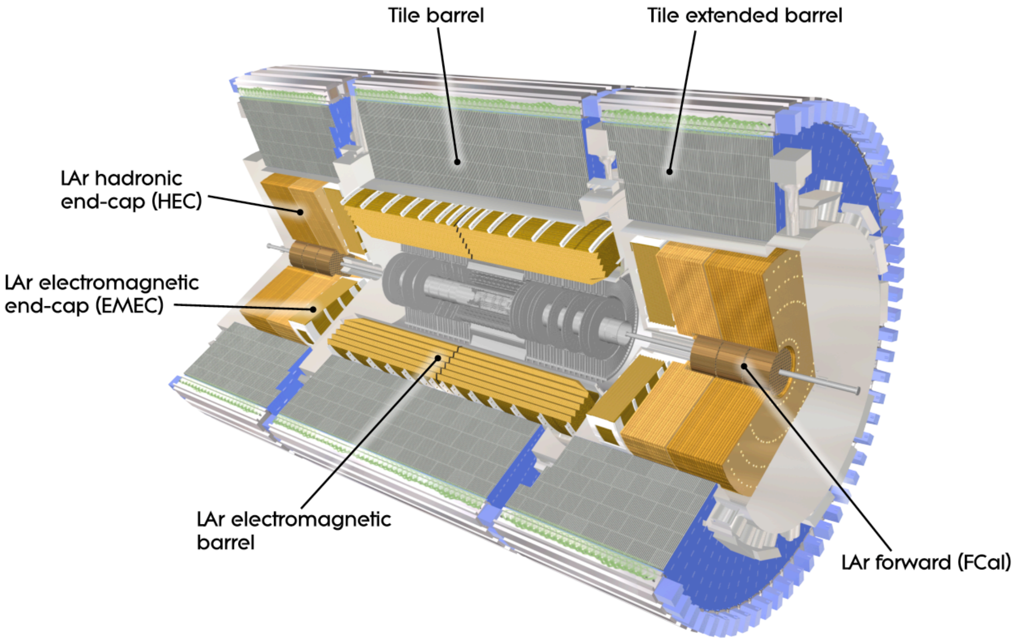

Figure 2.8. Overview of ATLAS calorimetric system

photon. The probability of interaction depends on the square of the number of protons of the nucleus Z and to the energy of the incident electron E_e

$$\sigma \sim Z^2 E_e$$

The photons themselves produce electron pairs via pair production, which is the dominant process for high energetic photons. Its cross-section depends also on Z^2 and to the photon energy E_γ

$$\sigma_p \sim Z^2 \ln E_\gamma$$

This leads to a cascade of electrons and photons. The ATLAS Electromagnetic Calorimeter uses lead absorber plates as passive medium, due to the high Z-number of lead, for the shower production of photons and electrons. Liquid argon acts as a ionisation chamber. The corresponding readout electrodes are made of copper and kapton.

The accordion shape of the lead plates (figure 2.9) was chosen to prevent cracks in azimuthal angle ϕ and hence allow a full ϕ-coverage. Moreover, this design ensures that approximately all tracks transverse the same amount of material. This method is called sampling technique, since not all tracks of the electron shower are detected. The liquid argon is kept in the same cryostat as the Inner Detector solenoid. The energy of incident electrons or photons can be determined in this way, since the number of produced electrons is proportional to the energy of incident electrons or photons. Test-beam measurements showed, that the energy resolution of the ATLAS EC can be parameterized roughly by

$$\frac{\Delta E}{E} = \frac{11.0\%}{\sqrt{E[GeV]}} \oplus 0.4\%$$

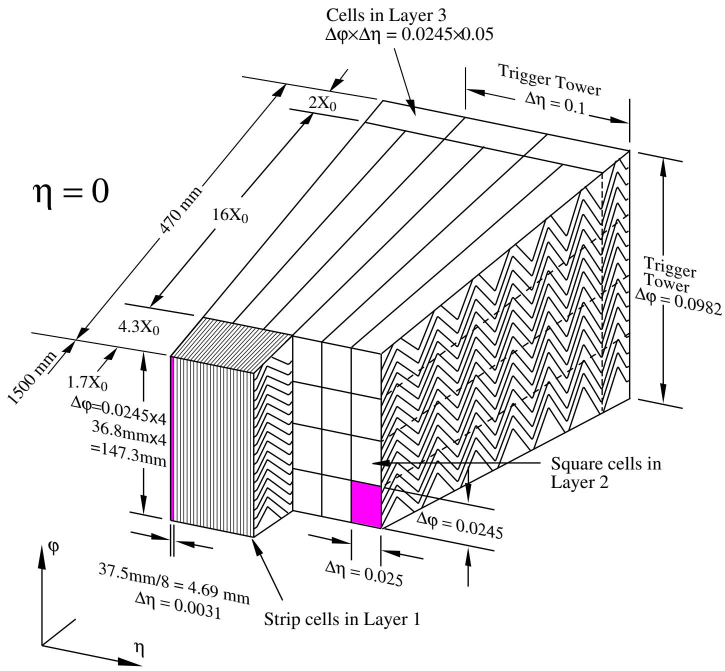

Figure 2.9. Sketch of the Electromagnetic Calorimeter.

The first term describes the statistical fluctuations of the sampling method, the second term stands for systematic uncertainties, which arises from inhomogeneities in the response of the calorimeter. The barrel region of the EC covers an η-range up to ± 1.475, the end-cap region is covered in the range $1.375 < |\eta| < 3.2$. An important aspect for the performance is the material budget in front of the EC because a significant fraction of the particles energy is lost in the inactive material in front of the EC thus causing a systematic uncertainty. The radiation length of material in front of the EC at $\eta = 0$ is 2.3 X_0. The Electromagnetic Calorimeter is preceded by a pre-sampling detector to correct for energy loss effects, in those regions which have a too large radiation length. In the overlap region between barrel and endcap, the material length is in the order of 7 X_0, which makes the insertion of a scintillator slab between barrel and endcap cryostat necessary.

Hadronic Calorimeter

The purpose of the Hadronic Calorimeter [14] is the identification, reconstruction and energy measurement of particle jets, which result from the hadronization of quarks and gluons, and the measurement of the missing transverse energy in an event. Hadronic showers are more penetrating in matter than electromagnetic ones, since the interaction length λ is tipical ten times larger.

The major difference between the Hadronic Calorimeter and the Electromagnetic Calorimeter is that the hadronic showers are produced via strong interactions. The incoming hadrons interact with the atomic nuclei and produce further neutrons, protons and primarily π^0 and $\pi^{\pm}$ mesons, which themselves start interacting with further nuclei. Roughly 20% of the incoming energy of the hadrons is used for breaking up the nuclear binding. This is one of the reasons for the worse energy resolution of the Hadronic Calorimeter compared to the Electromagnetic Calorimeter. The decay of π^0 into photons induces also an electromagnetic shower, which accompanies the hadronic counterpart. These hadronic interactions leave highly excited nuclei behind, which undergo fission or radiate to lower their energy state. These effects lead to a hadronic shower, which is measured again by a sampling technique. Due to the larger interaction length of hadrons, more material is needed in the Hadronic Calorimeter. The ATLAS Hadronic Calorimeter is positioned around the Electromagnetic Calorimeter from the radius 2.28 m to 4.23 m. The central barrel part, also called Tile Calorimeter, covers an η-region up to 1.0. An extended barrel region is responsible for the η-coverage from 0.8 to 1.7. Iron plates are used as absorber material and are also used as return yoke for solenoid magnet field. Scintillator plastic tiles are used as an active medium. The read out of the tiles is achieved with optical fibers. Readout Cells are formed by a cluster of tiles and are projective to the interaction point. They provide a granularity of $\delta\phi \times \delta\eta = 0.1 \times 0.1$ which corresponds to roughly 10,000 individual channels. The endcap part of the Hadronic Calorimeter uses copper plates as absorber material and liquid argon as ionization material. The barrel as well as the endcap part is segmented into three independent layers. The readout cells provide a three dimensional measurement of the deposited energy, which is needed for the reconstruction and the triggering of jets. The energy resolution of the Hadronic Calorimeter in the barrel region can be parameterized as [48]

$$\frac{\Delta E}{E} = \frac{50\%}{\sqrt{E[GeV]}} \oplus 3\%$$

The Hadronic Calorimeter is a possible source of background, called cavern background, for the muon detector. This background is mainly due to thermalized neutrons and low-energy photons produced along the hadronic shower development and escaping the calorimeter. The Hadronic Calorimeter must prevent hadrons from proceeding into the muon system and provide a good containment for hadronic showers. This is achieved by a total thickness of 11 interaction lengths of the Hadronic Calorimeter.

2.3.6 Muon Spectrometer

The only particles not absorbed by the calorimeters and reaching the most external sub-detector are the muons. Hence the outermost ATLAS layer is called Muon Spectrometer (MS), dedicated to the muon identification, reconstruction and trigger (figure 2.10). It is capable to provide a measurement both in a combined mode with the other sub-detectors and in a stand-alone mode. This feature allows to have a good discovery potential even at the TeV scale and at high luminosity, when the occupancy of the Inner Detector makes precision measurement with it an issue.

Before introducing the actual layout and design of the Muon Spectrometer, the basic principle of the momentum measurement in the Muon Spectrometer will be discussed briefly. An homogeneous magnetic field is assumed for this discussion of the main principles of the momentum measurement. Obviously, this assumption does not hold for the toroidal magnetic field, since this has large inhomogeneities around the coils, but the assumption is sufficient to introduce some of the main

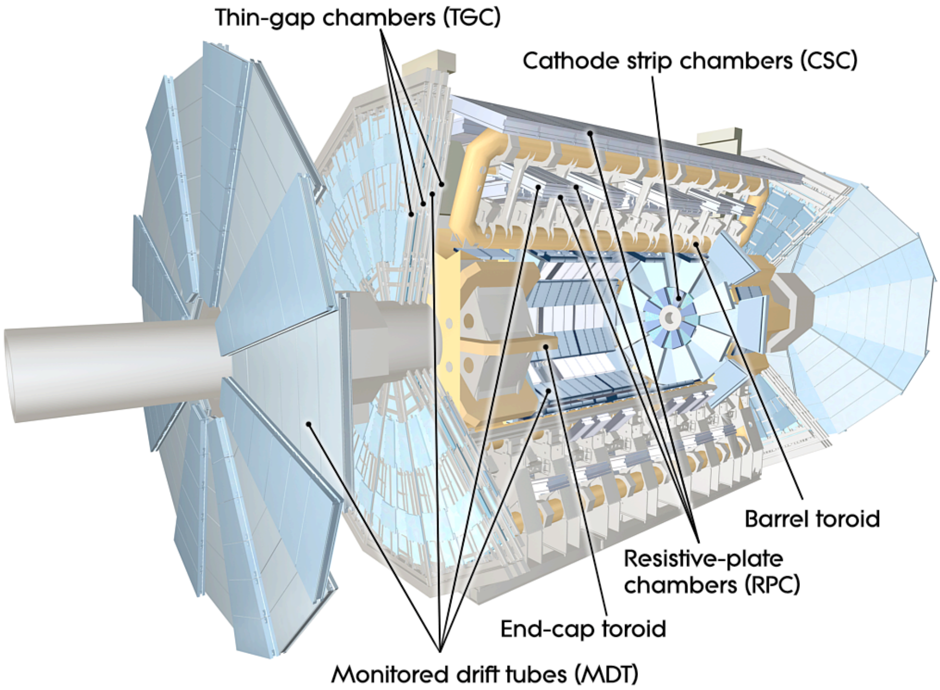

Figure 2.10. Overview of ATLAS muon system

concepts.

Since muons, which are perpendicular to the magnetic field, are bent on circles, it is sufficient to measure the radius of the circle to determine the muon's momentum. By referring to figure 2.11 where the variables are defined, we note that the radius r of a circle is correlated with its sagitta s, via

$$s = r\left(1 - \cos\frac{\alpha}{2}\right) \approx r\frac{\alpha^2}{8}$$

The dependence of the sagitta s on the transverse momentum p_T of a particle in a magnetic field is given by

$$s \approx \frac{1}{8}\frac{L^2 B}{p_T}$$

where B is the strength of the magnetic field and L the length of the muon trajectory. From this equation follows that the measurement of sagitta is equivalent to the measurement of the transverse momentum of a charged particle. The sagitta could be determined by measuring three points along the trajectory of the muon.

The ATLAS Muon Spectrometer has been designed to reach a momentum resolution of 10% for 1 TeV muons. Assuming a magnetic field strength of 0.6 T, which is roughly the average of the ATLAS torodial magnetic field, and an average trajectory length of 5 m, this leads to a required precision of 80 μm on the sagitta measurement. This required precision is achieved by four chamber technologies: *Monitored Drift Tubes* (MDT) and *Cathode Strip Chambers* (CSC) for precise muon

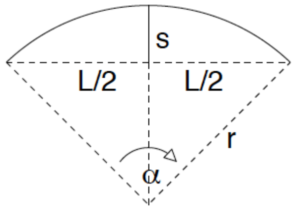

Figure 2.11. Sagitta definition

tracking in the central and in the very forward regions respectively; *Resistive Plate Chambers* (RPC) and *Thin Gap Chambers* (TGC) for muon trigger in the barrel and in the end-caps respectively (fig. 2.12).

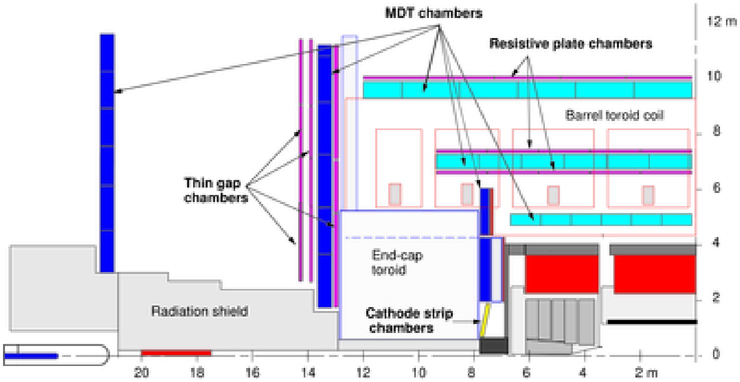

Figure 2.12. Sketch of ATLAS muon system in the longitudinal plane.

The layout of Muon Spectrometer was designed as a most hermetic system as possible and cover an η-range up to 2.7. The core elements of the Muon Spectrometer are the roughly 1.200 MDT chambers, which are responsible for a precise muon tracking and hence for a precise momentum measurement. The MDT chambers are positioned in such a way that all high energy muons coming from the interaction point of the detector should intercept at least three MDT chambers to provide a precise sagitta measurement. Such a combination of three MDT chambers, which is projective to the interaction point, is called tower in the following.

The MDT chambers are placed in three layers in the barrel region at radii of about 5 m, 7.5 m and 10 m. In the barrel, particles are measured near the inner and the outer magnetic field boundaries, and inside the field volume, in order to determine the momentum from the sagitta of the trajectory. There are also three layers of MDT chambers in the endcap region, concentric around the beam axis at 7 m, 14 m and 21 m from the interaction point. In the end-cap regions, for η >1.4, the magnet cryostats do not allow the positioning of chambers inside the field volume. Therefore the chambers in this region are arranged to determine the momentum with the best possible resolution from a point-angle measurement. A relatively large background rate is expected in the very forward region of the Muon Spectrometer. Hence, CSCs are used instead of the MDT chambers in the inner-most ring of the inner-most endcap layer, because of their finer granularity and less occupancy.

The huge size of the Muon Spectrometer and the required precision of the sagitta measurement of 80 μm, makes a precise alignment of the MDT chambers necessary. The MDT chambers are monitored by an optical alignment system, which is designed to provide a relative precision, i.e. the positioning of MDT chambers within one tower relative to each other, of 30 μm and an absolute precision, i.e. the positions of MDT chambers in the ATLAS coordinate system, of 300 μm. The label “monitored” of MDT reflects this fact. It should be noted that the relative precision has the dominant impact on the sagitta measurement. The optical alignment system will monitor the relative movement of the MDT chambers due to e.g. thermal effects, and provide the information for the muon trajectory reconstruction.

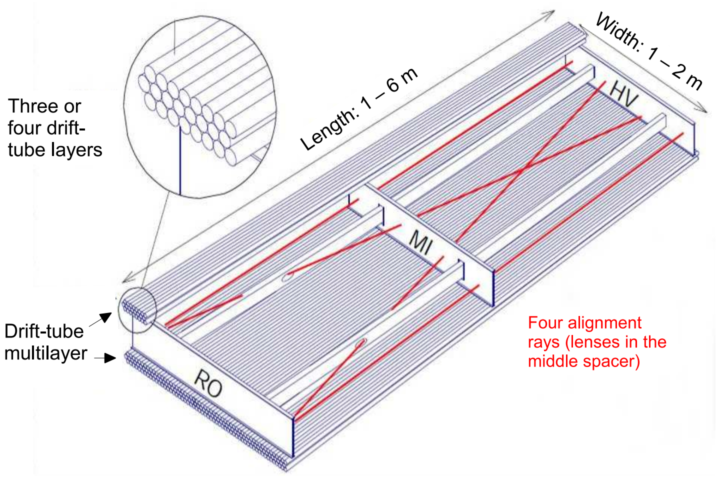

Figure 2.13. Scheme of an MDT chamber.

A schematic sketch of an MDT chamber is shown in figure 2.13. An MDT chamber consists of six to eight drift tube layers, which are arranged in two so-called multi layers with a spacing of 200 mm. The aluminum drift tubes have diameter of 30 mm and are filled with $Ar : CO_2$ gas mixture 93 : 7 at 3 bar absolute pressure. A central wire is positioned in the middle of the tube. A high energetic muon, which passes through a tube, ionizes the gas. The high voltage in the tube (3080 V) leads to an electric field, which lets the electrons drift towards the wire, while the positive ions drift towards the tube wall. When the drifting electrons reach some critical velocity, i.e. energy, they can ionize further gas molecules around them. This creates an avalanche of further electrons and leads to a so-called “Townsend avalanche”, which consists of electrons and positive charge ions. The ions drift through the whole potential difference to the tube wall and induce a measurable signal in the electrodes. By measuring the so-called drift-time, i.e. the time which is needed for the ionization cluster to reach the wire, one can determine the so-called drift-radius, i.e. the minimal distance of the muon trajectory to the central wire. A relatively bad resolution is expected for small drift-radii since the muon does not necessarily interact at the point of closest approach to the wire with the gas molecules. On average a precision of 80 μm is expected. Having measured the drift-radii for all tubes which have been hit, one can fit a tangential line to the drift-circles, which approximates the muon trajectory within one MDT chamber. These fitted straight lines are called segments in the following.

The CSC are multi-wire proportional chambers which are used in the very forward region of the Muon Spectrometer instead of the MDT chambers. They have an expected single track resolution of less than 60 μm. This good resolution is achieved by a cathode strip readout which measures the charge induced on the segmented cathode by the electron avalanche formed on the anode wires. The transverse coordinate can be calculated via the measurement of the orthogonal strips on the second cathode of the chamber. The chambers have a small sensitivity to photons ($\sim$1%) and also a small neutron sensitivity ($\leq 10^{-4}$). The small neutron sensitivity is achieved by the small gas volume used and the absence of hydrogen in the operating gas, which is a $Ar/CO_2/CF_4$ mixture.

The RPCs are the trigger elements for the barrel region, which provide a fast momentum estimation of muons for the hardware based trigger and also the necessary timing information for the drift-time measurement of the MDT chambers. They have a spatial resolution of 1 cm and timing resolution of 2 ns. The RPCs are made of two bakelite plates which form a narrow gap. The gap is filled with $C_2H_2F_4$ gas. Incident muons lead to ionization of the gas, which leads to a streaming discharge caused by the high electric field between the bakelite plates. The two bakelite plates are covered with read-out strips on their back, which are orthogonal with respect to each other. This allows an η and ϕ measurement of the muon track.

The TGCs are the trigger elements for the endcap region. They consist of two cathode plates with a distance of 1. $4mm$. The gap between the plates is filled with a gas mixture of C_5H_{10} and CO_2. Evenly spaced anode wires (1.8 mm spacing distance) are placed in between the plates and a high voltage of 3.1 kV is applied across the wires. Each wire collects a certain number of ionization electrons caused by an incident muon. The measured ionization electron distribution across all wires is used to identify the path of an incident muon. These chambers are combined to two or three layers to provide also a spatial coordinate measurement.

It should be noted that the choice of the toroidal magnetic field determines that the Muon Spectrometer measures the momentum p of the muons and not directly the transversal momentum p_T . Obviously these two quantities can be converted in each other via $p_T = p \sin\theta$. The design value of the transverse momentum resolution and its various contributions of the ATLAS Muon Spectrometer is shown in figure 2.14. The muon spectrometer is designed for a transverse momentum resolution of about 3 - 4% for muons with a $p_T = 50\ GeV$ and 10% for muons with $p_T = 1\ TeV$. The contribution of multiple scattering to the resolution is relatively small for low and high energetic muons due to the choice of air-core magnetic field configuration, which minimizes the use of material, but it's dominant in the intermediate region. Then the resolution is dominated by energy loss fluctuations on the calorimeters for low energetic muons (less than 20 GeV) and by the precision of the drift-radii measurement for high energetic muons (grater than 300 GeV).

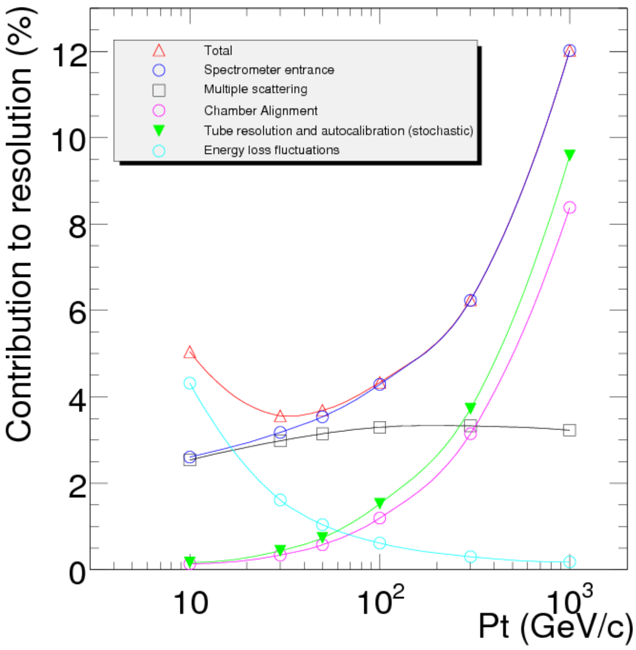

Figure 2.14. Contributions to the momentum resolution for muons reconstructed in the Muon Spectrometer as a function of transverse momentum for $|\eta| < 1.5$. The alignment curve is for an uncertainty of 30 μm in the chamber positions..

2.3.7 Trigger System and Data Acquisition

The data-size of one recorded collision is in the order of 1 MB. Since bunch crossings occur with a rate of 40 MHz, this would result in data volume which cannot be stored with today technologies. To be handled by the ATLAS computing system a reduction to 100 MB/s is needed. Thus the goal of the ATLAS trigger system is to reduce the rate of candidate collisions from 40 MHz to 100 Hz without a loss of interesting physics events. To achieve this goal the trigger system has three levels which are schematically illustrated in fig. 2.15.

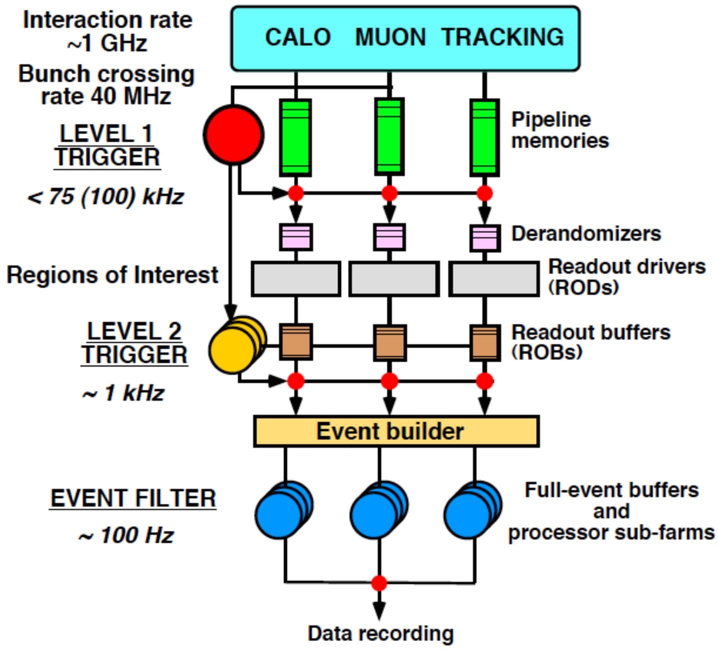

Figure 2.15. Overview of ATLAS trigger system.

The level-one trigger (L1) is hardware based. It uses information from the calorimeters with reduced granularity and from the muon trigger chambers, i.e. RPC and TGC stations, which fire for muons with sufficiently high energy. The latency of the level one trigger is 2 μs, which leads to a target rate of 75 kHz. A further important task of L1 is to define the so-called *region of interests* (RoIs) for each event. The RoIs are regions in the detector, where possibly interesting objects might be present, e.g. a high energetic muon. The L1 trigger passes the event information within the RoIs from the read-out buffers (ROBs) to the level-two trigger.

The level-two (L2) trigger is software based and uses the full granularity in the RoIs of the detector and also the Inner Detector. The target rate is 1 kHz, with a latency of 1 ms to 10 ms, depending on the complexity of the event. The full access of the L2 trigger on the event would exceed the required maximal latency and hence the concept of RoIs had to be introduced. The disadvantage of this approach is, that interesting objects, which have failed the L1 trigger, cannot be found by L2. If an event passes the L2 trigger requirements all the information of one event is collected from the ROBs by the so-called Event Builder and passed to the third trigger level, which is called Event Filter (EF). The Event Filter makes the final decision if an event is recorded for further analysis. Its target rate is 100 Hz.

The Event Filter is software based and runs on a computer farm near the ATLAS pit. This allows for a relatively long decision time of the order of one second. As a consequence, the EF has access to the full event with full granularity. More sophisticated reconstruction algorithms can be applied. Events which are accepted by the EF are written to mass-storage devices available for further offline-analysis.

The ATLAS trigger menu defines the operation of the trigger system and its conditions. A condition is a combination of an object, e.g. an electron, and a certain threshold, e.g. $p_T > 20GeV$.

Even with this output rate, the total storage space needed by the ATLAS experiment is in the order of 1 PetaByte ($10^{15} bytes$) per year. This makes a powerful computing environment necessary.

2.3.8 Muon Trigger and Reconstruction

As long as this thesis is mainly devoted to the muon performance assessment and the measurement of the Z boson cross-section into muons some more detail is given about muon trigger and reconstruction.

The muon reconstruction can use either only the MS information or the combination of the MS with the ID and the Calorimeter. Correspondingly the muon is defined as *stand-alone* or *combined*.

The **stand-alone** muon reconstruction is based entirely on muon-spectrometer information, independently of whether or not this muon spectrometer track is also reconstructed in the inner detector. The muon reconstruction is initiated locally in a muon chamber by a search for straight line track segments in the bending plane. Hits in the precision chambers are used and the segment candidates are requested to point to the centre of ATLAS. The hit coordinate ϕ in the non-bending plane measured by the trigger detectors is associated to the segment when available. A minimum of two track segments in different muon stations are combined to form a muon track candidate using three-dimensional tracking in the magnetic field. The track parameters (p_T , η, ϕ, distance of closest approach to the primary vertex along the beam axis and transverse to it) are obtained from the muon spectrometer track fit and are extrapolated to the interaction point taking into account both multiple scattering and energy loss in the calorimeters. For the latter, the reconstruction utilizes either a parametrisation or actual measurements of calorimeter energy losses, together with a parametrisation of energy loss in the inert material. The typical muon energy loss in the calorimeters is about 3 GeV. The stand-alone muon reconstruction algorithms use the least-squares formalism to fit tracks in the muon spectrometer and most material effects are directly integrated into the χ^2 function.

The **combined** muon reconstruction associates a stand-alone muon spectrometer track to an inner detector track, that measures the bending of the muon within the solenoid, using the pixel, SCT and TRT detectors. Tracks are reconstructed in the inner detector using a pattern recognition algorithm that starts with the silicon information and adds hits in the TRT. This “inside-out” tracking procedure selects track candidates with transverse momenta above 300 MeV. One further pattern recognition step is then run, which only looks at hits not previously used, starts from the TRT, and works inwards adding silicon hits as it progresses. This recovers tracks from secondaries, such as photon conversions and long-lived hadron decays. The association between the stand-alone and inner-detector tracks is performed using a χ^2-test, defined from the difference between the respective track parameters weighted by their combined covariance matrices. The parameters are evaluated at the point of closest approach to the beam axis. The combined track parameters are derived either from a statistical combination of the two tracks (*Staco* algorithm) or from a refit of the full track (*MuId* algorithm).

An alternative approach is used to recover muons whose reconstruction in the muon spectrometer failed, either because of too low muon p_T or because of the acceptance: this approach is based on the extrapolation of an inner detector track to the inner or middle stations of the muon spectrometer; the muon hypothesis is confirmed by a match to a track segment in these stations, not associated to a MS track. These muons are indicated as *tagged* muons.

Finally another type of muon identification is still possible which doesn't use the Muon Spectrometer information. This is based on Inner Detector tracks extrapolated to the calorimetric system. If the energy deposit associated to the track is compatible with the hypothesis of a minimum ionizing particle this is tagged as a muon. In the following this will be referred as *calo-muons*.

The **level-one muon barrel trigger** covers the region between $-1.05 < \eta < 1.05$. It is designed to provide three "low-p_T thresholds" between $4 \leq p_T \leq 10$ GeV , and three "high-p_T thresholds" between $10 < p_T \leq 40$ GeV . Each trigger threshold selects muons with a p_T greater that its value.
Because of the arrangement of detector services in the muon spectrometer, the feet of the detector, as well as support for the toroid coils, the barrel trigger coverage is $\sim 85\%$ of the region $-1.05 < \eta < 1.05$.

The trigger electronics uses signals coming from three layers of Resistive Plate Chambers (RPC). The RPCs are packed together with the MDT chambers. There are two layers of chambers around the MDT middle stations, of which the innermost layer is referred to as the *low-p_T plane* and the outer is known as the *pivot plane*. The third RPC layer is on the MDT outer station and is called the *high-p_T plane*.

The trigger logic is seeded by the pivot plane: if there is an hit on that plane, the trigger logic checks for hits on the low-p_T plane which are within a road defined around a track emerging from the interaction point and bending in the magnetic field and which are in the same time window of 25 ns (1 BC) ; if so, a low-p_T trigger is issued. To further reduce the fake rate, it is also required to have hits in at least 3 of the 4 layers (2 pivot and 2 low-p_T) involved in the trigger decision (called trigger majority).

When a low-p_T trigger is issued, the high-p_T trigger logic looks for hits in the high-p_T plane fulfilling the trigger logic requirement; one hit out of two gas-gaps in addition to the low-p_T trigger. This implies that an high-p_T trigger always requires a low-p_T , and in case of multiple triggers the systems forward to the subsequent trigger elements the highest p_T threshold issued.

This is relevant for the efficiency estimation: in fact, the inefficiency in the high-p_T trigger contains the inefficiency of the low-p_T ones.

The **level-one end-caps muon trigger** is based on signals provided by TGC

(Thin Gap Chamber) detectors. The TGCs provide triggers in a pseudo-rapidity range of $1.05 < |\eta| < 2.4$. The trigger logic is based on three trigger stations, located at increasing distance from the interaction point. The basic principle of the algorithm is to require a coincidence of hits in the different trigger stations within a road, which tracks the path of a muon from the interaction point through the detector. The width of the road is related to the p_T threshold to be applied. A system of programmable coincidence logic allows concurrent operation with a total of six thresholds. An inefficient region at the outer edge of the TGC is due to the presence of magnetic field, where muons bend away from TGC acceptance depending on their charges. Ineffective areas in the TGC are due to the presence of the holes for the laser optical alignment system and the physical boundary of the chambers where division in azimuth changes from 48 to 24. The geometrical acceptance of the TGC in the regions is about 98%.

The size of a L1 ROI slightly varies according to the position in the MS, the typical size being $\Delta\eta \times \Delta\phi = 0.1 \times 0.1$. The L1 muons are then confirmed by the High-Level Trigger (HLT). The first step is the Level-2 trigger (L2), where fast algorithms perform a coarse reconstruction of the muon track using also the information from the MS precision chambers (MDT and CSC), and combining them with the reconstruction performed in the Inner Detector (ID). To limit the data bandwidth, the L2 algorithms can access only the information in the RoI identified by the L1. Finally the Event Filter (EF) performs a detailed muon track reconstruction, making use of algorithms very close to those used for the offline event reconstruction.

Several configurations are available either based on the request of a single muon or of a pair of muons, corresponding to different cuts in the muon transverse momentum p_T. A conventional labeling is used which indicates the trigger level and the threshold such as *(Level)*_mu*(threshold)*. In this way for example the label EF_mu20 corresponds to the EF trigger level, with a p_T threshold of 20 GeV.

Chapter 3

Muon Efficiencies Measurement: Method and Performance

In this chapter the measurement of muon efficiencies is described. The motivation and the relevance of the measurement are illustrated. Then a method to perform the measurement on real data is shown which is based on the Z boson resonance: the *Tag&Probe* method.

3.1 Motivation

The cross-section measurement of a process in a collider experiment is essentially a counting experiment where one has to deduce how many events N_S of a certain type have been produced when n_S of them are observed. The number N_S is determined by the physics of the process, i.e. by its cross-section (σ), and the integrated luminosity of the analyzed data-sample:

$$N_S = L \cdot \sigma$$

The observed number n_S is the fraction of N_S which the detector is able to detect. Thus, this depends on the detector geometrical acceptance (A) and on the selection efficiency (ϵ).

$$n_S = N_S \cdot A \cdot \epsilon = L \cdot \sigma \cdot A \cdot \epsilon$$

So the cross-section is

$$\sigma = \frac{n_S}{L \cdot A \cdot \epsilon}$$

In practice, when the signal event selection is performed, the number of selected events N_{sel} is actually n_S plus a certain number of background events (N_b). To estimate the number of signal events, a background estimation and a subtraction procedure are required, and at the end the cross-section is given by

$$\sigma = \frac{N_{sel} - N_b}{L \cdot A \cdot \epsilon}$$

Summarizing, the components needed for a cross-section measurement are:

- Signal selection
- Background estimation and subtraction
- Luminosity measurement
- Acceptance evaluation
- Efficiency measurement

The acceptance evaluation is based on Monte Carlo predictions, assuming they correctly reproduce the generated particles distribution. This is defined as the fraction of signal events in the fiducial volume with respect to the total number of generated events. All other components can be measured from data in order to get the actual detector performance.

Muon trigger and reconstruction efficiencies, which are the focus of this thesis, are an essential part of the selection efficiency measurement for any physics analysis involving muons: this explains why their measurement from real data is so relevant.

Moreover whenever a data/MC comparison is required, the MC distributions have to be corrected to reproduce the actual performance of the detector instead of the nominal one. This is achieved using the ratio between the real selection efficiency (ϵ_{data}) and the expected one from MC (ϵ_{MC})

$$SF = \frac{\epsilon_{data}}{\epsilon_{MC}}$$

which is called *scale factor* (SF) and will be evaluated in the next chapter together with the efficiencies.

3.1.1 From Single Muon Efficiencies to Physical Process Efficiency

In the evaluation of the selection efficiency for a cross-section measurement, the efficiencies of all the analysis steps need to be taken into account. A typical analysis procedure requires, for example, an event selection, then a certain trigger to be fired, some good-quality criteria for the interesting objects, and so on and so forth. Each of these steps has its own efficiency, and all of them have to be combined together to get the final one.
In this thesis we will concentrate on the efficiency coming from muon selection, which is a combination of the reconstruction and trigger efficiencies. How these can be measured will be shown. But first of all, let's see how reconstruction and trigger efficiencies of single-muon combine to get the event efficiency.

Let's consider for example the $Z \rightarrow \mu^+ \mu^-$ process. Typically the selection for this process requires muon triggered events with two reconstructed muons according to a certain definition. Each muon is reconstructed in a given phase space bin specified by p_T, η and ϕ and at least one of them fired the trigger[1]. We use the symbol ζ to define the phase-space bin. Then $P(\text{event}, \zeta_1, \zeta_2)$ is the probability that an event with the two muons belonging to ζ_1 and ζ_2 is triggered and reconstructed.

With these definitions, the total number of selected events is connected to the Z production differential cross section by the:

$$\begin{aligned} N_{sel} &= L \cdot A \cdot \int d\zeta_1 d\zeta_2 \frac{d\sigma}{d\zeta_1 d\zeta_2} P(\text{event}, \zeta_1, \zeta_2) + N_{bkg} \\ &= L \cdot A \cdot \sigma \cdot \int d\zeta_1 d\zeta_2 \frac{df}{d\zeta_1 d\zeta_2} P(\text{event}, \zeta_1, \zeta_2) + N_{bkg} \end{aligned} \tag{3.1}$$

where the integral is extended to the entire fiducial volume

In the second line we have factorized the total cross-section and introduced the normalized distribution $f(\zeta_1, \zeta_2)$ of the signal events in the phase-space. The integral shown above is exactly the total efficiency of the process under study:

$$\epsilon = \int d\zeta_1 d\zeta_2 \frac{df}{d\zeta_1 d\zeta_2} P(\text{event}, \zeta_1, \zeta_2) \tag{3.2}$$

In fact, given the total efficiency of the process and the expected number of background events, the cross-section turns out to be:

$$\sigma = \frac{N_{sel} - N_b}{L \cdot A \cdot \epsilon} \tag{3.3}$$

Thus eq. 3.2 suggests that ϵ depends on two ingredients: the distribution $\frac{df}{d\zeta_1 d\zeta_2}$ of the muons according to the physical process under study, and the detection efficiency $P(\text{event}, \zeta_1, \zeta_2)$. If they are both well described by the Monte Carlo simulation, ϵ turns out to be simply the ratio between the numbers of the selected and of the generated events in the fiducial volume. If the description of the detector efficiencies is not fully under control (as it is expected to be at least during the first years of data taking), one can use the Monte Carlo simulation to describe the kinematic distribution of the signal events $\frac{df}{d\zeta_1 d\zeta_2}$, and data control samples to get the detector efficiencies $P(\text{event}, \zeta_1, \zeta_2)$. The simulation naturally provides the integration in ζ_1 and ζ_2 of the single event probabilities according to equation 3.2.

The probability $P(\text{event}, \zeta_1, \zeta_2)$ can be expressed as a combination of single muon efficiencies. Defining $P(R, \zeta)$ the probability that a muon in the bin ζ is reconstructed, and $P(T|R, \zeta)$ the probability that the reconstructed muon satisfies a given trigger condition, the probability that the whole event is selected:

$$\begin{aligned} P(\text{event}, \zeta_1, \zeta_2) &= P(R, \zeta_1) \cdot P(R, \zeta_2) \cdot \\ &\quad [P(T|R, \zeta_1) + P(T|R, \zeta_2) - P(T|R, \zeta_1) \cdot P(T|R, \zeta_2)] \end{aligned} \tag{3.4}$$

where ζ_1 and ζ_2 are the bins of the two reconstructed muons in the event. In the general case of n muons in the event, the formula is:

$$P(\text{event}, \vec{\zeta}) = \left[\prod_{i=1,n} P(R, \zeta_i) \right] \cdot \left[1 - \left(\prod_{i=1,n} (1 - P(T|R, \zeta_i)) \right) \right]$$

[1]For simplicity we neglect here the case of the trigger being due to an extra muon either fake or not coming from the Z decay. The amount of these events is negligible according to the Monte Carlo.

where naturally both $P(R,\zeta)$ and $P(T|R,\zeta)$ depend on the way a reconstructed muon is defined.

To conclude, in order to get the total event efficiency we need the reconstruction efficiency for each selected muon and its trigger efficiency. The Tag&Probe method, illustrated in the following section, has been developed to measure these two quantities from data. It also gives the possibility to measure the absolute trigger efficiency, i.e. not dependent on the muon reconstruction, which is not needed for cross-section measurements but it's quite interesting for the detector performance assessment.

3.2 Tag&Probe Method

3.2.1 The Method

The Tag&Probe method (TP) described here is based on the kinematic and dynamic correlation between the muons coming from the Z boson decay. The idea is to tag one of the two muons with tight criteria, then take advantage of the correlation to select the second muon (to be used as probe to test the efficiencies) with high purity, despite never using the system it's meant to test. In particular, the Z mass constrain is fundamental in order to guarantee a pure selection and suppress the background.

The signature of $Z \to \mu^+\mu^-$ events is two isolated muons in the final state, coming from the primary vertex of the event. The idea of the method is to tag one of the two muons, i.e. the *tag*, using the information from the Inner detector, the calorimeters and all the muon sub-detectors, in order to have an high purity selection. The tag muon is also required to have fired one of the trigger signatures responsible for the event acquisition: this ensures an unbiased measurement of the trigger efficiency using any other object in the event. Then the aim is to select the second muon, i.e. the *probe*, without using the information from the sub-system of which one intends to measure the efficiency (in this case the muon trigger and the reconstruction sub-detectors), taking advantage of the kinematical correlation of the two muons.

For muon **reconstruction efficiency** measurement in particular one needs to select the probe never using the Muon Spectrometer information. These probes are then selected from the tracks reconstructed in the Inner Detector and so in the following they will be called *Indet probes*. These probes can be also used to measure the muon trigger efficiency with respect to the inner tracker reconstruction, because no trigger information is used to select them too. This will be referred in the following as **absolute trigger efficiency**.

To measure the muon trigger efficiency with respect to the offline reconstruction, is possible to use tracks reconstructed in the Muon Spectrometer as long as no trigger requirements are applied. Therefore these probes are selected starting from reconstructed muon tracks and so in the following they will be called *Muon probes*. In this case the efficiency will depend on the reconstructed muon definition and thus on the physics process it is meant to be applied to. This means that the method has to be flexible enough to allow the efficiencies to be measured for any kind of muon definition. This efficiency will be referred in the following as **relative trigger efficiency**.

Finally the efficiencies are stored in a format which is easily accessible to the physics analyses. This format is chosen to be an n-dimensional matrix where the dimensions are the variables with respect to which the efficiencies are expected to have some dependence. The standard ones are p_T , η and ϕ of the probe. This allows the efficiency corrections in a phase space bins as required by the specific analysis. In the following the dependence of the efficiencies on the jets variables in the event will be also studied, which is relevant for example in the case they have to be applied to the W/Z+Jets cross-section measurement (see section 2.1.1).

In the following section the details of this analysis will be shown including selection cut flow, Monte Carlo studies, comparison with Monte Carlo truth and background contribution. The results on the 7 TeV data and the comparison with the MC expectations will be shown in the next chapter.

To implement this method the *InsituMuonPerformance* package has been developed within the official ATLAS software and all the results shown in the following sections are obtained with it.

3.2.2 Monte Carlo Samples

In order to perform these studies a number of signal and background Monte Carlo samples have been used. They have been generated at $\sqrt{s} = 7\,TeV$ with PYTHIA [16] using MRSTLO* [17] parton distribution functions (PDF), then simulated with GEANT4 [18] and fully reconstructed.

The main backgrounds to the analysis are expected to come from all processes which generate di-muon final states, such as the leptonic $Z \rightarrow \tau^+\tau^-$, $b\bar{b}$ and $t\bar{t}$ or processes with an high p_T muon in the final state plus one fake muon from the underlying event, such as the $W \rightarrow \mu\nu$. To simulate them the corresponding MC samples have been used. For the $t\bar{t}$ sample POWHEG [19] is used.

To simulate the Z/γ^* process, for convenience two samples are used. The first one covers an invariant mass range below 60 GeV and the cross-section is only available at the LO and it will be referred as Drell-Yan$\rightarrow \mu^+\mu^-$ (DY) in the following. The second one covers an invariant mass range above 60 GeV and its cross-section at NNLO is $\sigma(Z/\gamma \rightarrow l^+l^-) = 0.99$ nb. This will be referred as $Z \rightarrow \mu^+ \mu^-$ and it essentially represent our signal. In the following the term “Z cross-section” will generically refer to the $Z/\gamma \rightarrow l^+l^-$ cross section. The second one covers an invariant mass range below 60 GeV and the cross-section is only available at the LO.

To each sample a filter is applied at the generation level, in order to select only the events with at least one lepton in the fiducial volume ($|\eta| < 2.8$) and eventually with at least a minimum transverse momentum. This is done because the simulation of the particles interaction with the detector is a time-demanding process, and pre-selecting the interesting events (with minimal cuts similar to that one that will be applied at the analysis level afterwords), optimizes time and disk-space needed, because the final samples are smaller too, as well as processing time.

The relevant samples used in the analysis are summarized in table 3.1 with their cross-sections, the used generator, the filter applied and the integrated luminosity available.

Monte Carlo Samples				
Sample	Int. Lumi [pb^{-1}]	XSec*ϵ_{filter} [pb]	Filter	Generator
$Z \rightarrow \mu^+ \mu^-$	310	964	$M_{ll} > 60$ GeV & 1 μ in $\|\eta\| < 2.8$, $\epsilon_{filter} = 0.975$	Phytia
Drell-Yan$\rightarrow \mu^+\mu^-$	798	1253	$M_{ll} < 60$ GeV	Phytia
W$\rightarrow \mu\nu$	109	9161	1 μ in $\|\eta\| < 2.8$, $\epsilon_{filter} = 0.876$	Phytia
Z $\rightarrow \tau\tau$	40	989	–	Phytia
$b\bar{b}$	60	73900	1 μ with $p_T >$ 15 GeV in $\|\eta\| < 2.8$	Phytia
$t\bar{t}$	2297	87.	1 lepton with $p_T > 1$ GeV , $\epsilon_{filter} = 0.538$	PowHeg

Table 3.1. Monte Carlo samples used for the Tag&Probe analysis. For each sample the generator used, the cross-section, the filter and the integrated luminosity available are reported.

3.2.3 Selection Scheme

In this section a brief scheme of the Tag&Probe analysis is given. Let's suppose we are interested in measuring the efficiencies for a certain definition of muons to be used in a physics analysis:

1. The tags collection is built
2. The Indet probes collection is built starting from Inner Detector tracks
3. From the reconstructed muon collection the muons are pre-selected following the requirements of the physics measurement (e.g. isolated, combined muons, coming from the primary vertex)
4. The Muon probes collection is built starting from the pre-selected muons
5. The reconstruction and trigger efficiencies are calculated and stored in a standard format

The efficiencies are calculated with the following definitions:

Reconstruction Efficiency is the number of Indet probes matching one of the pre-selected muons over the total number of Indet probes

- the matching cone is determined by the reconstruction resolution and is chosen to be $\Delta R < 0.005$

Absolute Trigger Efficiency is the number of Indet probes matching a certain trigger object (this is done for each trigger item and level one wants to test, e.g. L1_MU10 RoIs) over the total number of Indet probes

- the matching cones are determined by the trigger angular resolution at the HLT, which is different for the L2 and EF, and by the ROI size for the L1. So they are chosen to be
$\Delta R < 0.3$ for L1 trigger objects
$\Delta R < 0.05$ for L2 trigger objects
$\Delta R < 0.02$ for EF trigger objects

Relative Trigger Efficiency (with respect to the offline reconstruction) is the number of Muon probes matching a certain trigger object (as for absolute trigger efficiency) over the total number of Muon probes

- the matching cones are chosen as for the absolute trigger efficiency case:
$\Delta R < 0.3$ for L1 trigger objects
$\Delta R < 0.05$ for L2 trigger objects
$\Delta R < 0.02$ for EF trigger objects

3.2.4 Selection Cut Flow

Let's go trough the details of the Tag&Probe selection.

1. Tag Selection

The first step of the analysis is the selection of the **tag muons**. The tag muon is a combined muon coming from the primary vertex, within a geometrical acceptance of $|\eta| < 2.5$. Moreover the tag muon must have passed the muon trigger selection: this allows an unbiased study of the trigger properties of the other objects in the event. The p_T cut on the tag is thus determined by the trigger threshold. The tag is also required to come from the primary interaction vertex, so a cut on the transverse distance of closest approach of the track to the vertex, defined as d_0, is applied. Finally it has to be isolated in the inner tracker. The track isolation is defined as the sum of the transverse momenta of the ID tracks in a cone of given radius ΔR around the muon minus the sum of the transverse momenta in an inner cone of a radius 0.1 to exclude the momentum of the track itself. This energy is then normalized to the muon track p_T . The size of the cone used in this analysis is $\Delta R = 0.3$.

2. Indet probes selection

Then for each tag the **Indet probe** selection starts from an inner detector track with opposite charge sign to the tag, required to have a transverse momentum larger than 5 GeV to reduce the combinatorial background (the biggest part of the tracks in the ID has a very low momentum coming from the underlying event) and to be in a fiducial volume ($|\eta| < 2.5$).

In order to select only tracks coming from the primary vertex, the $|d_0|$ of the track is required to be smaller than 0.1 mm. This meant to reject muons from long lived particles, such as B mesons, as can be seen from figure 3.1 which shows the d_0 distribution for signal and background samples before the corresponding cut.

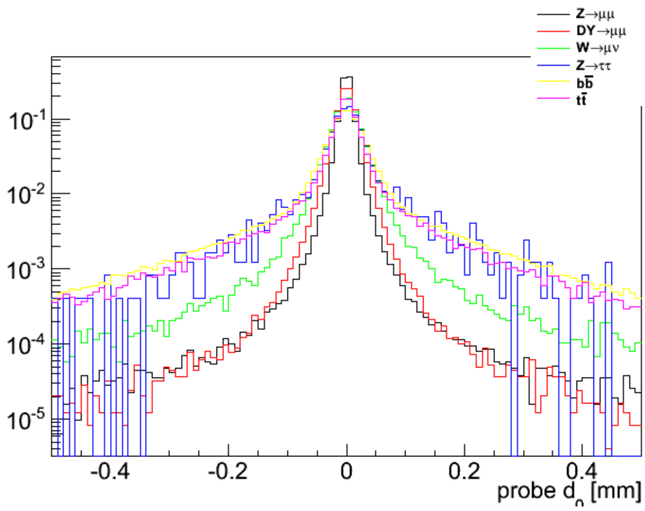

Figure 3.1. Impact parameter distribution for Indet probes at the selection step before the corresponding cut. Signal and backgrounds are all normalized to unit. The cut is chosen to be $|d_0| < 0.1mm$

Then the track has to come to the same vertex of the tag, so a cut on the difference between the longitudinal impact parameter of the tag and the probe $|\Delta z_0| < 0.5\, mm$ is applied (being the resolution on the z_0 parameter $\sim 90\mu m$).

A track isolation cut is applied, mainly to reject muons within jets. Looking at this variable distribution for the tracks selected just before this cut, figure 3.2, the isolation energy over p_T is chosen to be smaller than 0.1.

Further cuts are needed to reject other background processes that produce two muons uniformly distributed in the space, e.g. the $t\bar{t} \to \mu^+\mu^- + X$, or the events with an ID track faking a muon, e.g. $W \to \mu\, \nu$. The tag and the probe are required to be back-to-back in the transverse plane ($\Delta\Phi > 2.14\, rad$), as can be seen from figure 3.3.

Then, to further reduce the background due to a fake muon coming from the $W \to \mu\, \nu$ events, the probe is required to match a CaloMuon. Finally the tag and probe invariant mass has to lie in a range of $\pm$ 20 GeV around the Z mass (figure 3.4)

3. Muon Pre-Selection

In the following analysis the **muon definition**, which it's meant the efficiencies to be calculated for, is chosen to be that one used for the $Z \to \mu^+\, \mu^-$ cross-section measurements (see chapter 5), illustrated in table 3.2. So the next step of the analysis is the muon pre-selection following these criteria.

These cuts have been studied on real data to improve the quality of the muons used in the analysis. In particular, the requirement on the muon transverse momentum measured in the MS, the p_T resolution and the requirements on the hits associated to the track, are not meant to reject the background and have no big effect on MC, but they remove a number of bad reconstructed muons in data.This is because in data Staco combined muons have been found with a big mis-match between the p_T reconstructed in the Inner Detector and that one reconstructed in the Muon

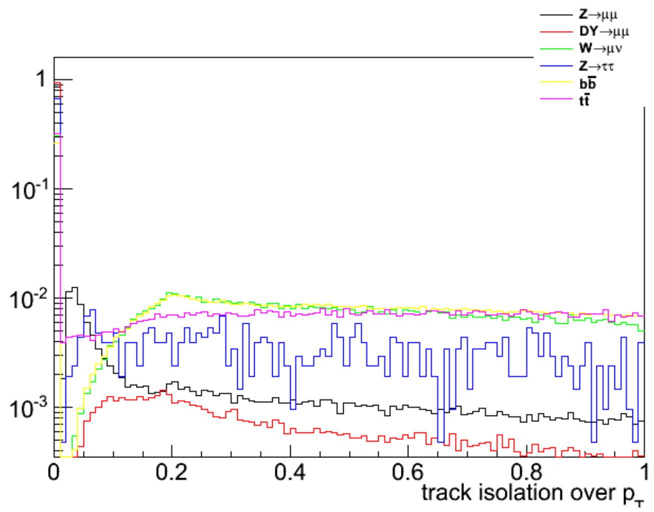

Figure 3.2. Isolation over p_T distribution for Indet probes at the selection step before the corresponding cut. Signal (mainly concentrated in the first bin, black line just below the red line) and backgrounds are all normalized to unit. The cut is chosen to be isolation/$p_T < 0.1$

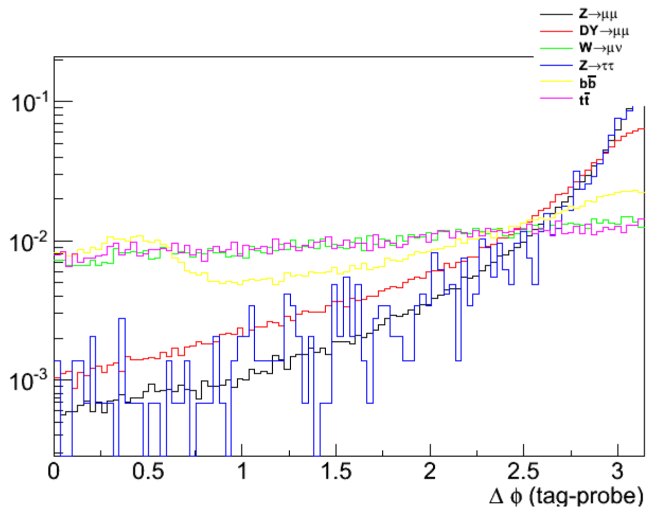

Figure 3.3. Tag-probe $\Delta\phi$ distribution for Indet probes at the selection step before the corresponding cut. Signal and backgrounds are all normalized to unit. The cut is chosen to be $\Delta\phi > 2.14$

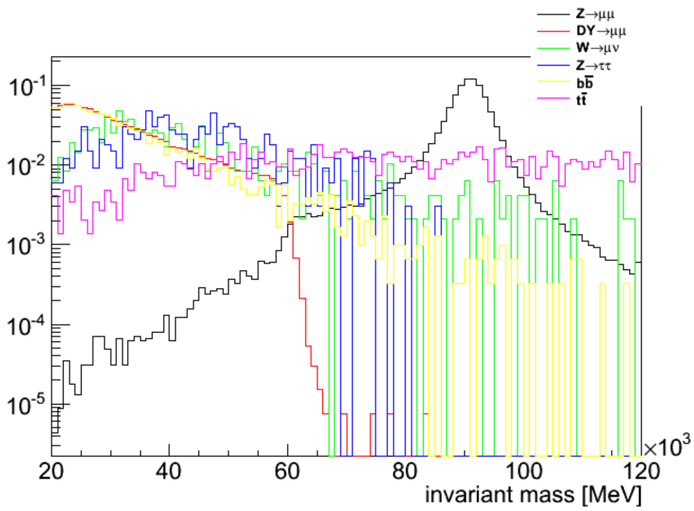

Figure 3.4. Tag-probe invariant mass distribution for Indet probes at the selection step before the corresponding cut. Signal and backgrounds are all normalized to unit. The tag-probe mass is required to lie in a range between 71 and 111 GeV. Notice that the DY samples drops around 60 GeV because it is produced with an invariant mass < 60 GeV. Above the signal sample $Z \rightarrow \mu^+ \mu^-$ starts.

Spectrometer, which we want to remove. In section 4.2 distributions of these variables from data will be shown and discussed to clarify the choice.

The pre-selected muon are then matched with the Indet probes to measure the reconstruction efficiency and are used to build the Muon probes collection to measure the trigger efficiency with respect to the muon reconstruction.

4. Muon probes selection

The **Muon probes** are selected starting from the pre-selected muon collection. After the pre-selection a set of cuts are applied to the muons to fullfill the requirement of coming from the Z-boson decay. They are essentially the same already discussed in the Indet probes selection: the muon has to be opposite charge sign to the tag, tag and the probe have to come from the same vertex ($\Delta z_0 < 0.5\, mm$), they have to be back-to-back in the transverse plane ($\Delta\Phi > 2.14\, rad$) and their invariant mass has to lie in a range of $\pm$ 20 GeV around the Z mass.

The summary of the Tag&Probe selection cuts is shown in table 3.3. In the next section the study of the method performance using this selection is presented. The expected results is described and the possible sources of systematic errors will be discussed.

3.3 Study of the Method Performance

Table 3.4 and 3.5 show the cut-flow of the muon pre-selection and the Indet and Muon probe selection for signal and background samples. All numbers are normalized to an integrated luminosity of 1 pb^{-1} to allow an easy comparison and interpretation of the results.

Muon Pre-Selection Cuts	
Type	Combined Muon
p_T	> 15.0 GeV
$\|\eta\|$	< 2.5
Track Isolation (0.2)	< 1.8 GeV
# PIX hits	> 1
# SCT hits	> 5
# TRT hits	> 0 (only for $\|\eta\| < 2.0$)
$\|p_T^{ID} - p_T^{MS}\|/p_T^{ID}$	< 0.5
p_T^{MS}	> 10 GeV
d_0	$< 0.1\ mm$
z_0	$< 10\ mm$

Table 3.2. Muon pre-selection cuts. This is chosen to be the same used for the inclusive Z and Z+jets 7 TeV analysis. The variables used in the selection are defined in the text.

	Tag&Probe Selection @ 7 TeV		
Cut	Tag	Indet Probes	Muon Probes
Type	Combined Muon	InDet Track	Pre-selected Muon
Charge	-	OS	OS
Trigger	L1_MU10	-	-
p_T	> 10.0 GeV	> 5.0 GeV	-
$\|\eta\|$	< 2.5	< 2.5	-
d_0	< 0.1 mm	< 0.1 mm	-
Δz_0	-	< 0.5 mm	< 0.5 mm
Track Isolation	< 0.2	< 0.1	-
$\Delta\Phi$	-	> 2.14 rad	> 2.14 rad
CaloMuon matching	-	True	False
ΔM	-	$M_Z \pm 20$ GeV	$M_Z \pm 20$ GeV

Table 3.3. Tag&Probe selection for 7 TeV analysis. Jet selection: $p_T > 20$ GeV in $|y| < 2.8$

The effect of the background component will be discussed in more detail in section 3.3.2.

Muon Pre-Selection Summary						
Cut	$Z \to \mu\mu$	$DY \to \mu\mu$	$W \to \mu\nu$	$Z \to \tau\tau$	$t\bar{t}$	$b\bar{b}$
Initial Muons	1608.1	898.5	8719.1	296.8	85.3	49624.3
After pre-selection	1275.8	113.2	6566.0	83.9	28.6	7243.9

Table 3.4. Muon pre-selection cut-flow. Numbers are normalized to an integrated luminosity of 1 pb^{-1}

Indet Probes Selection						
Cut	$Z \to \mu\mu$	$DY \to \mu\mu$	$W \to \mu\nu$	$Z \to \tau\tau$	$t\bar{t}$	$b\bar{b}$
Type	1182.05	337.47	1427.85	77.39	54.98	10168.07
p_T	1182.05	337.47	1427.85	77.39	54.98	10168.07
$\|\eta\|$	1154.90	330.06	1400.14	76.2	54.34	9968.75
Charge	1011.70	307.63	807.35	60.71	32.67	5469.39
d_0	1001.99	304.91	769.08	52.54	28.35	4547.18
Δz_0	1001.99	304.91	769.08	52.54	28.35	4547.18
TrackIsol	889.47	285.18	217.61	36.17	8.45	995.06
$\Delta\Phi$	795.33	230.78	87.11	31.64	3.24	503.68
CaloMuon	744.35	191.74	4.53	8.39	1.13	56.57
ΔM	704.3 $\pm$ 1.3	–	0.52 $\pm$ 0.09	0.45 $\pm$ 0.4	0.29 $\pm$ 0.01	1.30 $\pm$ 0.01
Muon Probes Selection						
Cut	$Z \to \mu\mu$	$DY \to \mu\mu$	$W \to \mu\nu$	$Z \to \tau\tau$	$t\bar{t}$	$b\bar{b}$
Type	800.11	82.2	0.62	5.6	2.72	75.32
Charge	799.99	82.19	0.46	5.55	2.57	72.69
Δz_0	790.86	81.1	0.43	5.32	2.53	66.63
$\Delta\Phi$	728.42	64.63	0.15	4.78	1.0	13.32
ΔM	689.2 $\pm$ 0.6	–	0.02 $\pm$ 0.08	0.32 $\pm$ 0.01	0.26 $\pm$ 0.01	0.65 $\pm$ 0.01

Table 3.5. Tag&Probe cut-flow. Numbers are normalized to an integrated luminosity of 1 pb^{-1}

At the end of the selection we are left with 706.9 $\pm$ 1.3 Indet probes and 690.5 $\pm$ 0.6 Muon probes per pb^{-1} of integrated luminosity. Figures 3.5, 3.6 and 3.7 show how they are distributed in p_T , η and ϕ. Essentially the whole Muon Spectrometer can be exploited with the method and efficiencies for muons with a p_T in a range between $\sim$ 10 and $\sim$ 100 GeV can be measured.

In the η distribution of the Muon probes is clearly visible the geometrical acceptance of the Muon Spectrometer. In fact less probes are selected around $\eta = 0$ and $|\eta| \sim 1.2$ where the Muon Spectrometer has a poor coverage.

This holes are not present in the Indet probes distribution due to the fact that the ID has a full coverage in η.

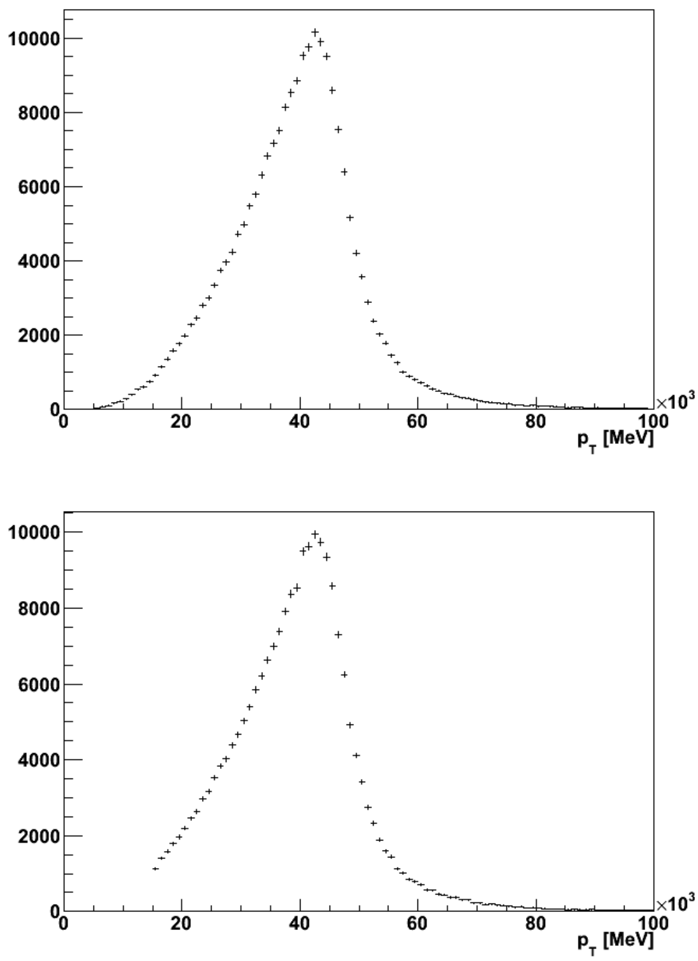

Figure 3.5. Transverse momentum distribution of the Indet (upper plot) and Muon (lower plot) probes. This shows the range exploitable with the method.

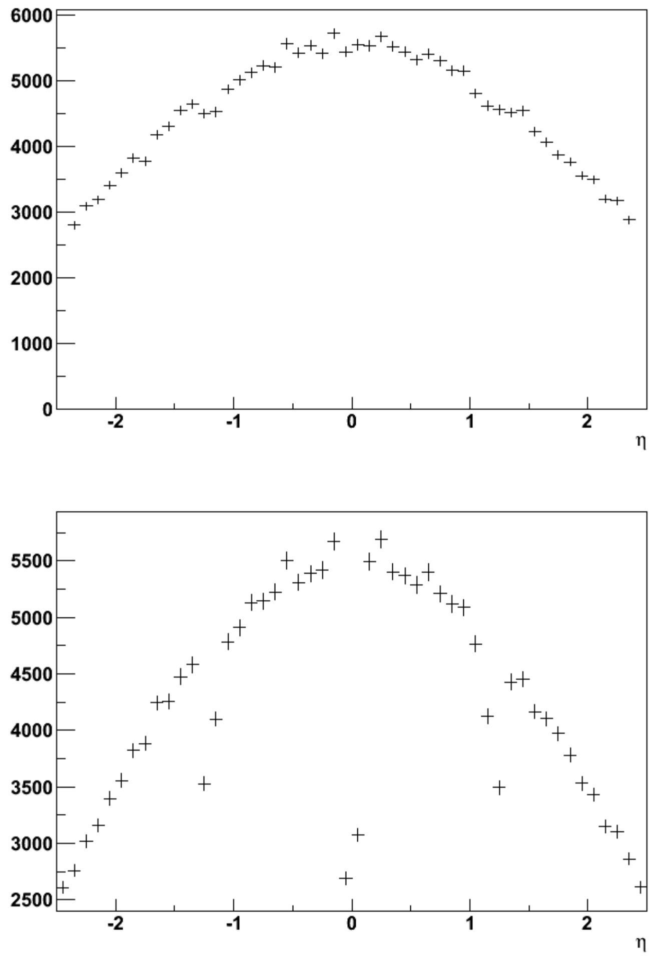

Figure 3.6. Pseudorapidity distribution of the Indet (upper plot) and Muon (lower plot) probes.

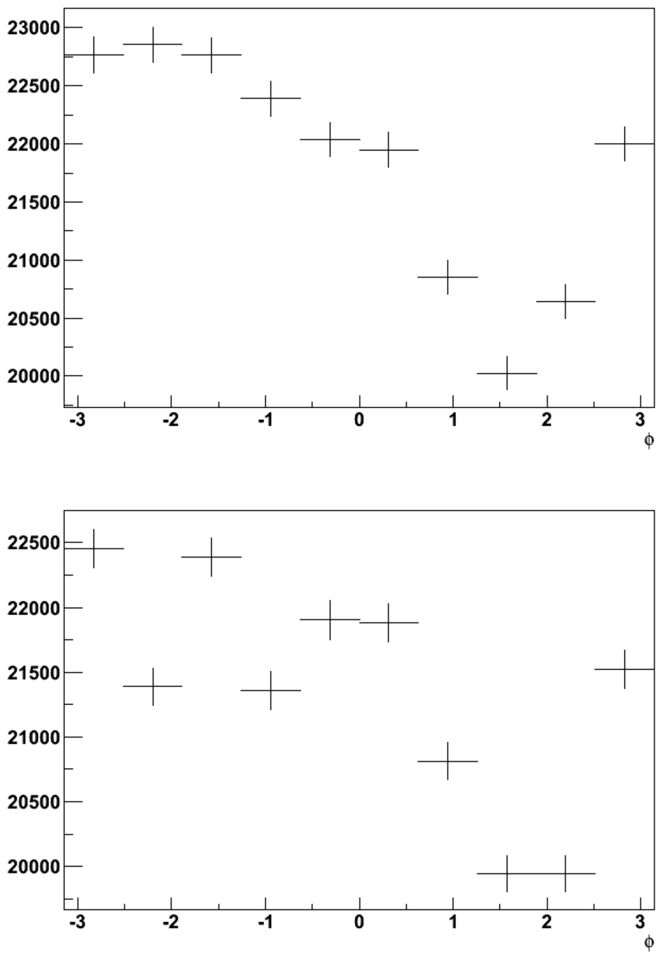

Figure 3.7. Azimuthal angle distribution of the Indet (upper plot) and Muon (lower plot) probes. Notice that the scale is expanded and there is only a 7% difference between the upper and the lower bins.

The small deeps in the ϕ distributions of both kind of probes are instead due to the tag selection. In fact when the tag muon comes in a region around the feet of the experiment it has less probability to be reconstructed. As a consequence a smallest number of probes are selected in these cases which means a deep in the distribution in a region opposite to the feet one in ϕ (around $\phi \sim 1.2$ and $\phi \sim 2.0$). Nevertheless this is not a bias for the differential efficiency measurement, but only a reduction of the statistics in the interested regions.

3.3.1 Reconstruction and Trigger Efficiencies

In this section the results of the efficiencies measurement using the Tag&Probe method on MC signal samples are illustrated. The effect of the background on the efficiencies will be discussed later on.

Reconstruction Efficiency

The reconstruction efficiency, for muons defined as in table 3.2, is shown in figures 3.8 as a function of the probe p_T. It is essentially flat with an average value of 92.02 ± 0.06 % in the full range.

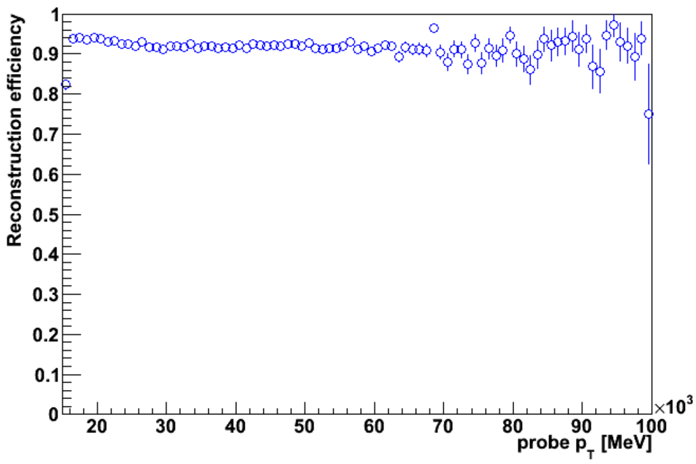

Figure 3.8. Muon combined reconstruction efficiency vs p_T.

The efficiency behavior versus η, figure 3.9, as expected shows the structure of the muon spectrometer: it drops in the crack region around $\eta = 0$ and around $|\eta| \sim 1.2$ as expected. In the same way the efficiency is flat in ϕ, figure 3.10, with two small drops around the feet regions as expected as well.

Trigger Efficiencies

The absolute trigger efficiency also shows a peculiar behavior. First of all it should be noticed that the average efficiency of each trigger level is always below $\sim 85\%$: this is mainly due to the L1 trigger acceptance (see section 2.3.8), which is not factorized, and only $\sim 1\%$ is actually due to the intrinsic trigger detector efficiencies.

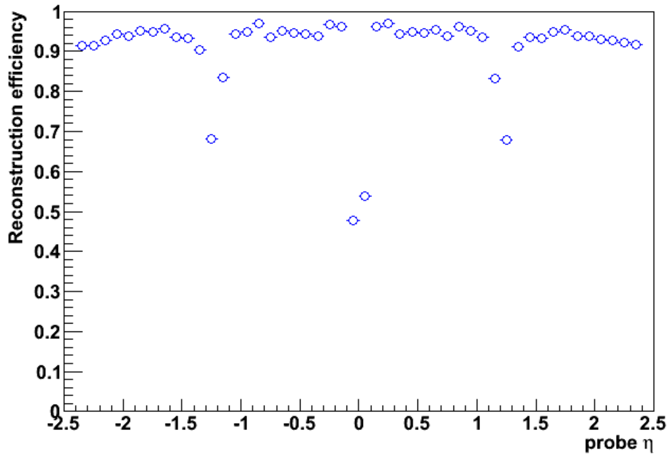

Figure 3.9. Muon combined reconstruction efficiency vs η.

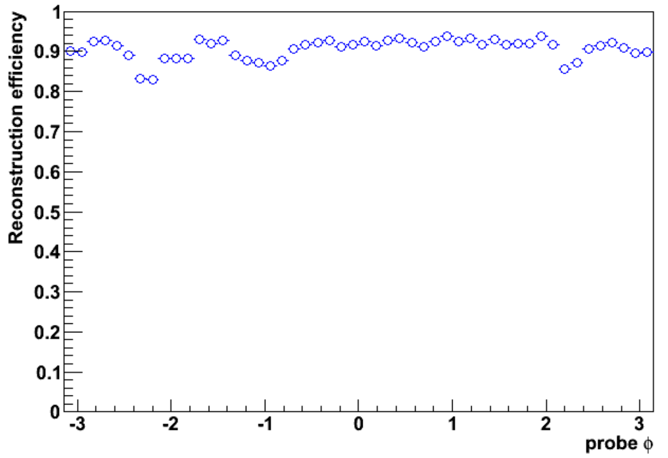

Figure 3.10. Muon combined reconstruction efficiency vs ϕ.

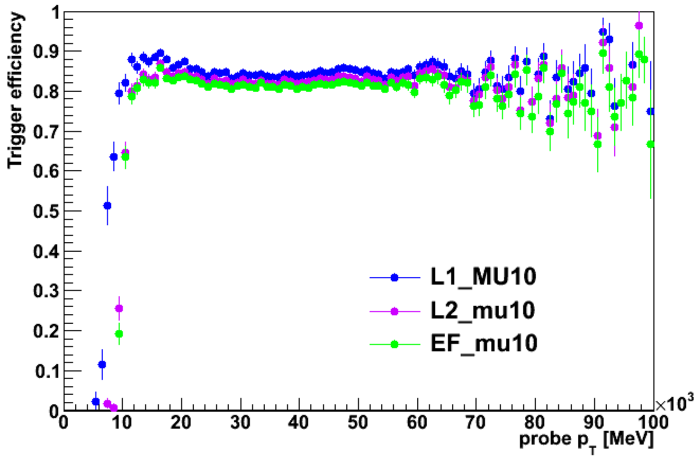

Figure 3.11. Absolute trigger efficiency for 10 GeV threshold vs p_T . The three trigger levels are shown: L1 (blue), L2 (magenta) and EF (green).

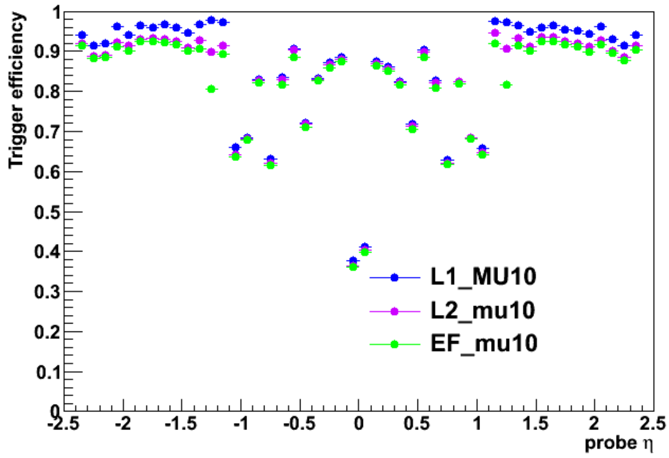

Figure 3.12. Absolute trigger efficiency for 10 GeV threshold vs η. The three trigger levels are shown: L1 (blue), L2 (magenta) and EF (green).

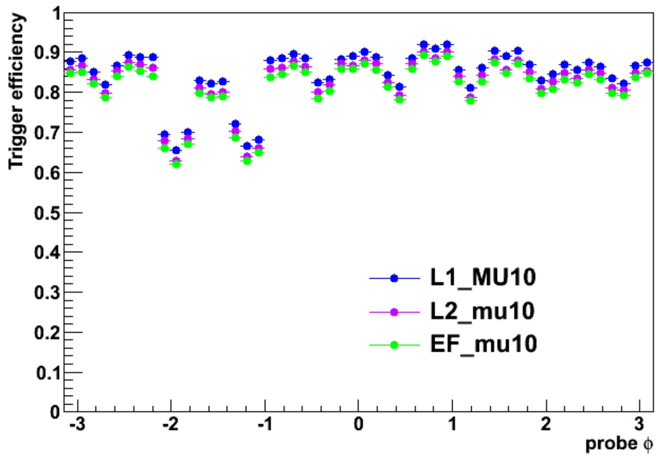

Figure 3.13. Absolute trigger efficiency for 10 GeV threshold vs ϕ. The three trigger levels are shown: L1 (blue), L2 (magenta) and EF (green).

From the η distribution (fig. 3.12) is also possible to distinguish how the acceptance regions are distributed. Looking in more detail:

- in p_T (fig. 3.11) three regions can be distinguished
  - below the nominal trigger threshold (10 GeV for the EF_mu10 trigger item) the efficiency is zero because the trigger is not supposed to select muons with less than 10 GeV of momentum
  - around the nominal threshold a turn-on is visible which rises the efficiency from zero to the expected value (plateau). The sharp rise is smoothed by the resolution effect on the L1 p_T measurement, which is worse for higher thresholds (with higher p_T the sagitta is smaller and smaller so the resolution on is worse). The threshold is defined as the value of p_T where the efficiency is the 80% of the plateau value
  - above the threshold the trigger has its best efficiency ($\sim$ 83% in this example)
- in η (fig. 3.12) the different acceptance regions are visible: the end-caps regions are almost 98% efficient while the barrel is around 80% with an hole around $\eta = 0$ as expected
- the ϕ (fig. 3.13) distribution also shows the acceptance regions being flat in all the range but the feet regions. It also shows the sectors structure of the muon spectrometer: the efficiency oscillates regularly where the lower efficiency regions are in correspondence of the small sectors, and the higher efficiency regions in correspondence of the large sectors.

Going from the L1 to the EF the efficiency drops only by few percents: this means that the trigger algorithms are almost 100% efficient and that actually the main contribution to the average trigger efficiency is the acceptance of the L1 trigger detectors (mainly in the barrel region, see figure 3.12).

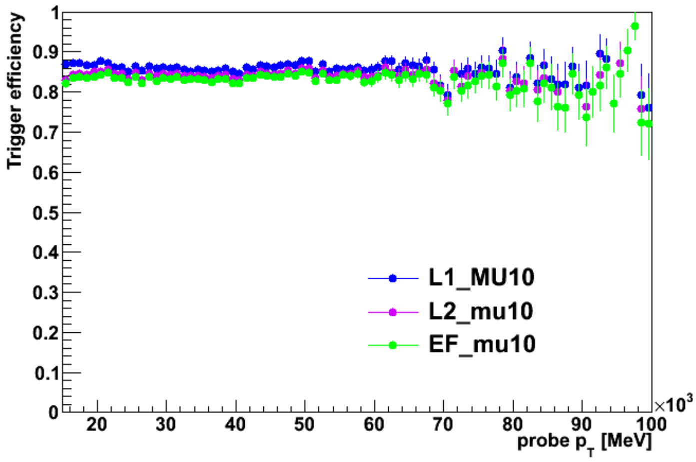

Figure 3.14. Trigger efficiency with respect to muon reconstruction for 10 GeV threshold vs p_T . The scale starts from 15 GeV due to the cut done in muon preselection. The three trigger levels are shown: L1 (blue), L2 (magenta) and EF (green).

The trigger efficiencies with respect to the muon reconstruction show the same structure of the absolute ones (figures 3.14, 3.15 and 3.16). The only difference is that the p_T distribution doesn't show the turn-on only because the muons taken into account have more than 15 GeV of p_T (so are already in the plateaux region) and the average efficiency is some percent higher. This is due to the fact that the probability of triggering a muon is higher when it has been already reconstructed and of course it depends on the definition of the reconstructed muon (the tighter is the muon definition, the higher the probability of having fired the trigger).

As in the case of the item EF_mu10 taken as example, it is possible to measure trigger efficiency for any trigger item and level, in accordance with what is needed for the analysis. In table 3.6 are reported the values of the trigger and reconstruction efficiencies at the plateau. Both the statistical errors using the full MC statistics and the expected ones with 1 pb^{-1} of integrated luminosity are reported.

Average Efficiencies and Uncertainties for 1 pb^{-1}		
Efficiency	Plateau Value (full sample)	Error with 1 pb^{-1}
Reconstruction	92.02 ± 0.06 %	1.0 %
Relative EF_mu10	83.45 ± 0.08 %	1.5 %
Absolute EF_mu10	81.42 ± 0.08 %	1.5 %

Table 3.6. Trigger and reconstruction efficiencies at the plateau. Both the statistical errors using the full MC statistics (first column) and the expected ones with 1 pb^{-1} of integrated luminosity (second column) are reported.

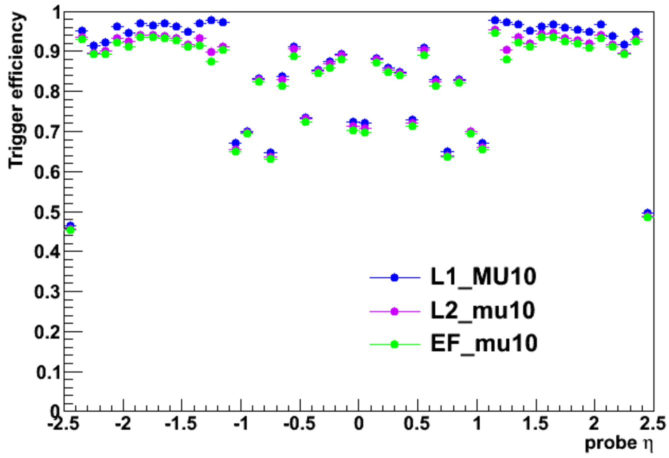

Figure 3.15. Trigger efficiency with respect to muon reconstruction for 10 GeV threshold vs η. The three trigger levels are shown: L1 (blue), L2 (magenta) and EF (green).

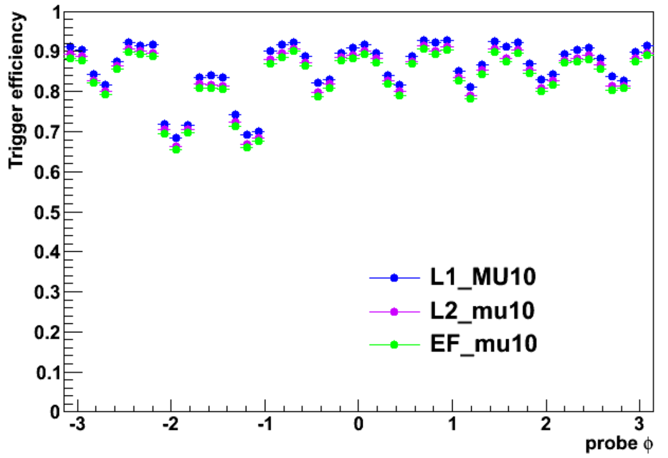

Figure 3.16. Trigger efficiency with respect to muon reconstruction for 10 GeV threshold vs ϕ. The three trigger levels are shown: L1 (blue), L2 (magenta) and EF (green).

3.3.2 Systematics Studies

In this section the assessment of the systematic errors to the efficiency measurement will be described. First of all the bias due to the method used will be estimated comparing the efficiency with the T&P method on the MC signal sample and the one measured from the MC truth. Then the background contribution and the dependence of the efficiency from the selection cuts and the jets in the event will be considered.

Comparison with the MC Truth

The bias on the efficiency measurement with the T&P method can be estimated comparing it with the expected efficiencies from the MC truth. For this comparison the MC signal sample is used.

The MC truth efficiencies are estimated as in the following:

- all generated muons are taken as probes within $|\eta| < 2.4$ and $p_T > 5$ GeV. They are matched with the pre-selected reconstructed muons (as in table 3.2) to calculate the reconstruction efficiency and with the trigger objects to calculate the absolute trigger efficiency

$$\text{Reconstruction Efficiency} = \frac{\#\text{ probes matching a reconstructed muon}}{\#\text{ selected probes}}$$

$$\text{Abs Trigger Efficiency} = \frac{\#\text{ probes which fire the trigger}}{\#\text{ selected probes}}$$

- all generated muons which match a pre-selected reconstructed muon are taken as probes and matched with the trigger objects to calculate the relative trigger efficiency

$$\text{Rel Trigger Efficiency} = \frac{\#\text{ probes matching a reco muon and firing the trigger}}{\#\text{ probes matching a reco muon}}$$

Figures 3.17, 3.18 and 3.19 show the comparison between the p_T, η and ϕ distributions with the T&P method and the MC truth for the two kind of probes. The main discrepancy is in the muon p_T shape especially in the low-p_T region, biased by the T&P selection.

The MC truth selection has more probes with respect to the Tag&Probe selection in the low-p_T region, where the trigger is less efficient (turn-on region) and the reconstruction shows a turn-on due to resolution effect. This results in a little bias

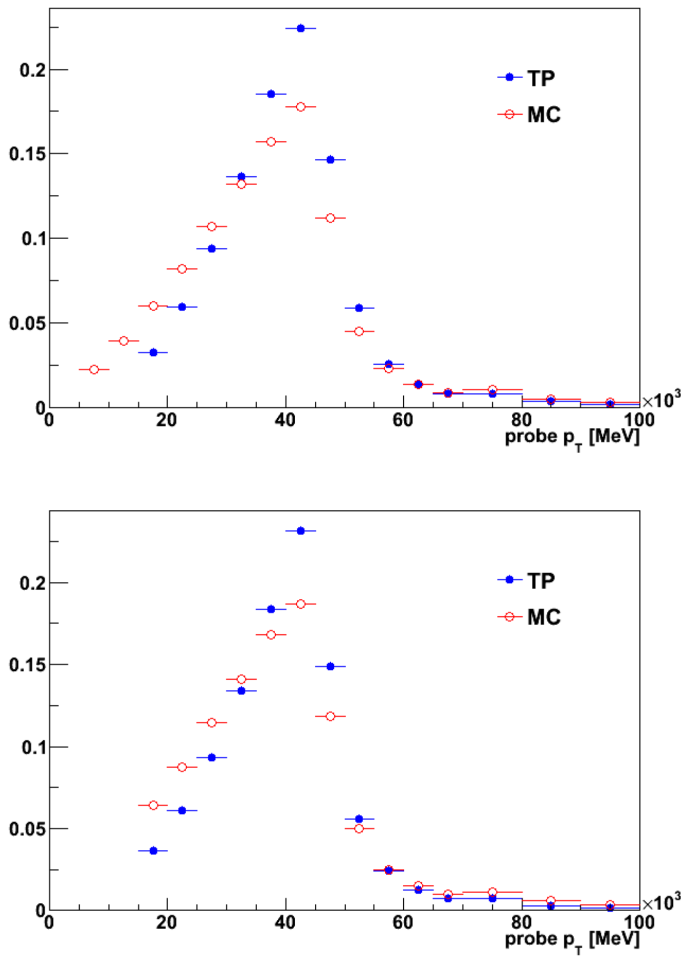

Figure 3.17. Comparison between Indet (upper plot) and Muon (lower plot) probes p_T distributions from T&P (blue) and MC truth (red). Distributions are normalized to the unit.

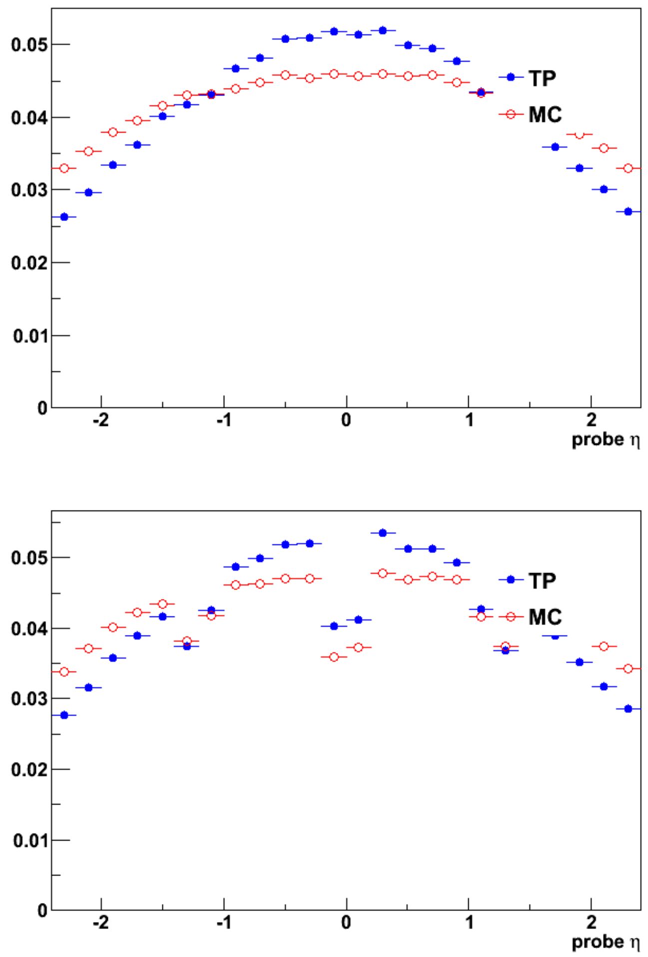

Figure 3.18. Comparison between Indet (upper plot) and Muon (lower plot) probes η distributions from T&P (blue) and MC truth (red). Distributions are normalized to the unit.

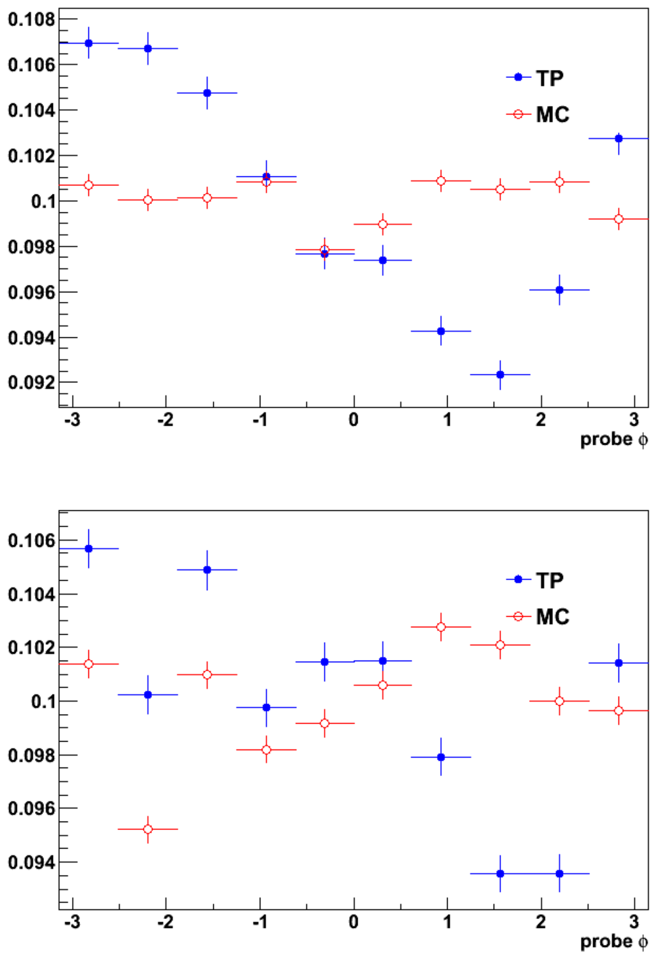

Figure 3.19. Comparison between Indet (upper plot) and Muon (lower plot) probes ϕ distributions from T&P (blue) and MC truth (red). Distributions are normalized to the unit.

in this region both in reconstruction efficiency (figure 3.20) and in absolute trigger efficiency (figure 3.21). The relative trigger efficiency is not affected (figure 3.22) because in this case only the trigger plateau region is involved, where the efficiency is constant, so a different probe p_T shape doesn't make any difference.

In order to not to bias the measurement it's sufficient to take into account the efficiencies in a proper phase-space binning. In this way one disentangles the effect of the muon distribution from the efficiency contribution.

Background Contribution

As already discussed the main background to the T&P selection comes from processes which can generate di-muon final states, such as the leptonic $Z \rightarrow \tau^+\tau^-$, $b\bar{b}$ and $t\bar{t}$ or those with an high p_T muon in the final state plus a fake probe (Indet or Muon) from the underlying event, such as the $W \rightarrow \mu\nu$. Table 3.5 shows that after the probe selection the main background comes from the $b\bar{b}$ process, and that the overall contribution is 0.36 $\pm$ 0.14 % for Indet probes and 0.18 $\pm$ 0.12 % for Muon probes.

Figures 3.23 and 3.24 show the background distributions in p_T and invariant mass both for Indet and Muon probes at the end of the selection. The background is mainly concentrated in the lower p_T region: this causes an efficiency drop in the region between 10 and 20 GeV in both reconstruction (figures 3.25) and trigger (figures 3.26 and 3.27) efficiencies, but it's better visible in the absolute trigger efficiency just because it covers a p_T range down to 5 GeV .

Till now the background effect on the efficiencies has been neglected because it's contribution is less than 1% effect. Anyhow in order not to rely on the MC predictions the background should be estimated from data, especially because in the first data the effect on the efficiencies around 20 GeV is visible, as will be shown in the next chapter. This effect and a method for a first background data-driven estimation will be discussed in more detail in section 4.8.

Jet Variables

As long as one of the first applications of the muon efficiencies is the measurement of the correction factors for the the W and Z differential cross-section measurements as a function of the number of the jets in the event, it's also important to understand the dependence of the efficiencies on the jets variables.
The jets have been chosen to be reconstructed using an "anti-kt" algorithm [15], which guarantees for being infrared and collinear safe.

In principle one expects that the higher is the jet multiplicity in the events, the higher the probability to have a jet close to the muon we want to measure the efficiency for. When the jet and the muon are close, can happen that the high track multiplicity in the Inner Detector can affect the reconstruction efficiency.
So what we expect is a reduction of the reconstruction efficiency in the events with high jet multiplicity and in general in the events with a jet close to the muon.
On the other hand, the L1 trigger efficiency in principle should not be affected in the same way, because the L1 trigger doesn't use any Inner Detector information so is less sensitive to the muon isolation.

In order to reduce this efficiencies dependence, one can use an appropriate jet definition. For example one can consider to add to the usual jet selection, i.e. $p_T >$

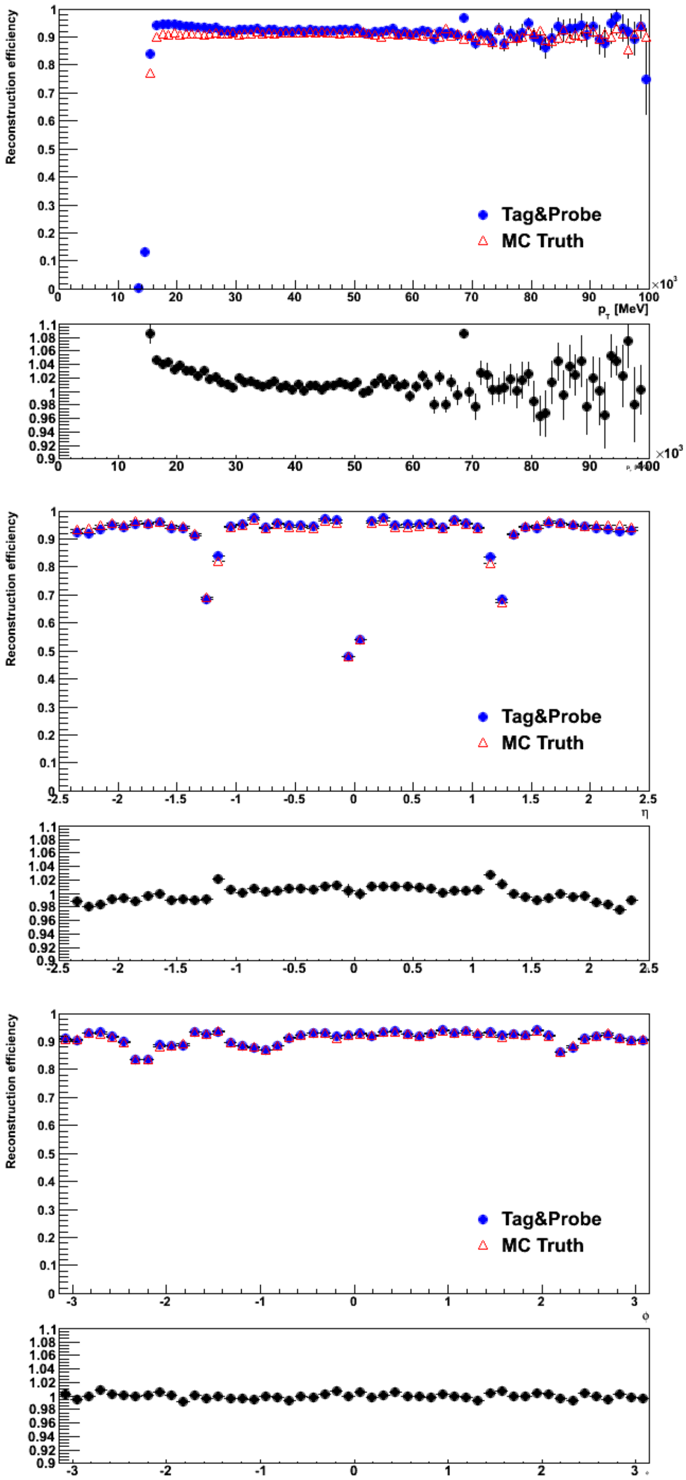

Figure 3.20. Reconstruction efficiencies for T&P (blue) and MC truth (red) vs p_T , η and ϕ.

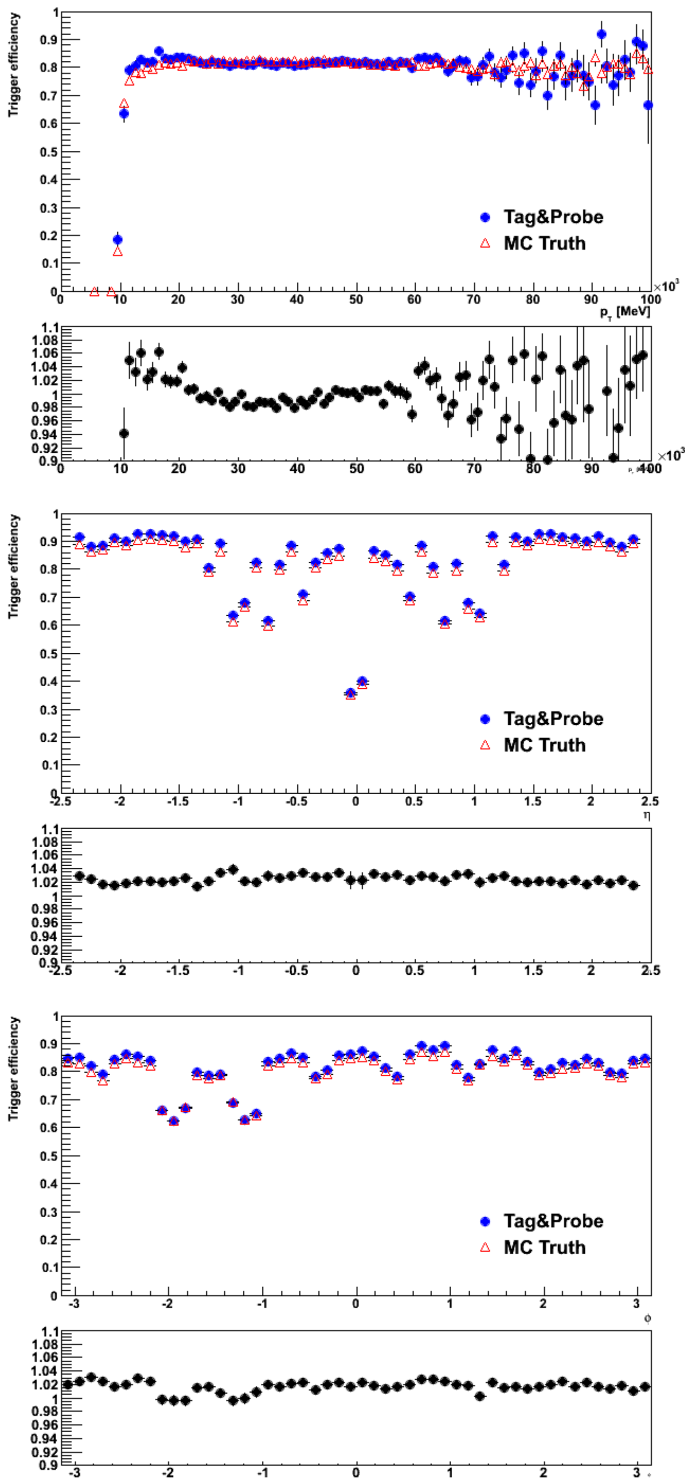

Figure 3.21. Absolute EF_mu10 trigger efficiencies for T&P (blue) and MC truth (red) vs p_T , η and ϕ .

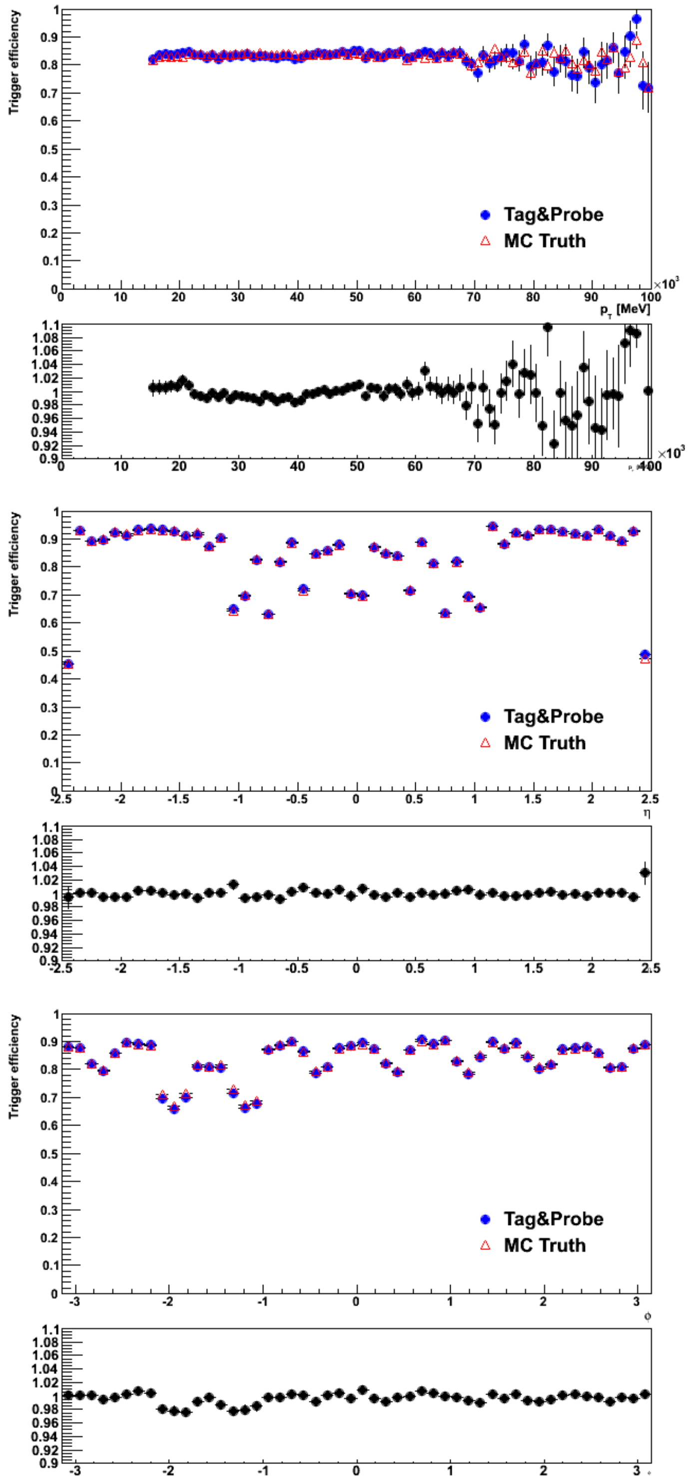

Figure 3.22. Relative EF_mu10 trigger efficiencies for T&P (blue) and MC truth (red) vs p_T , η and ϕ.

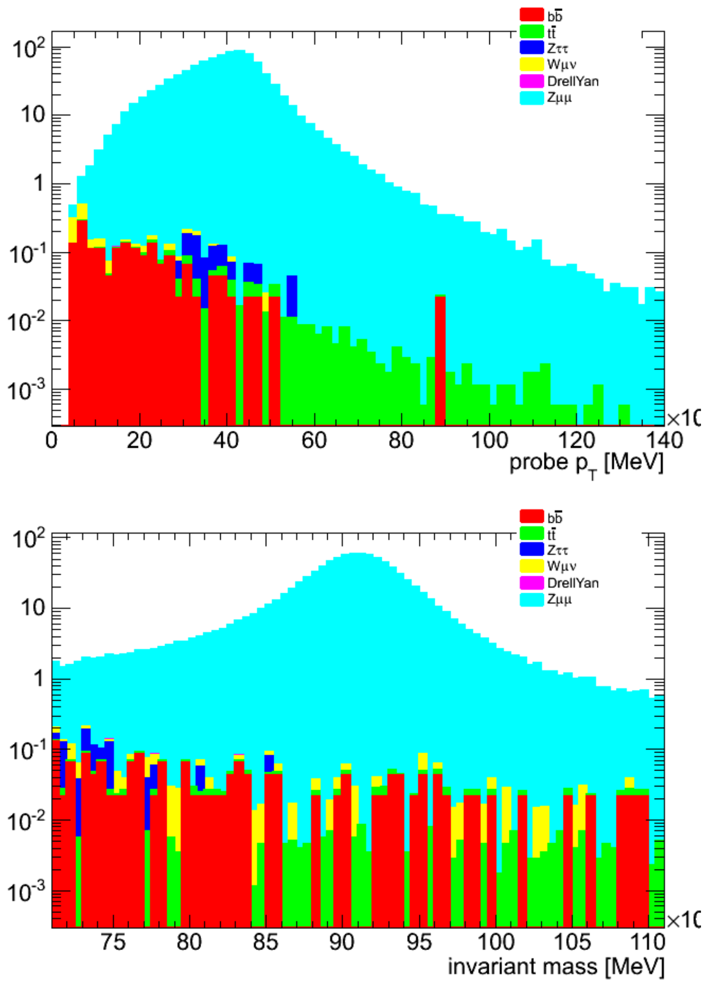

Figure 3.23. Indet probes p_T and invariant mass distribution after the selection. Signal and background contributions are shown.

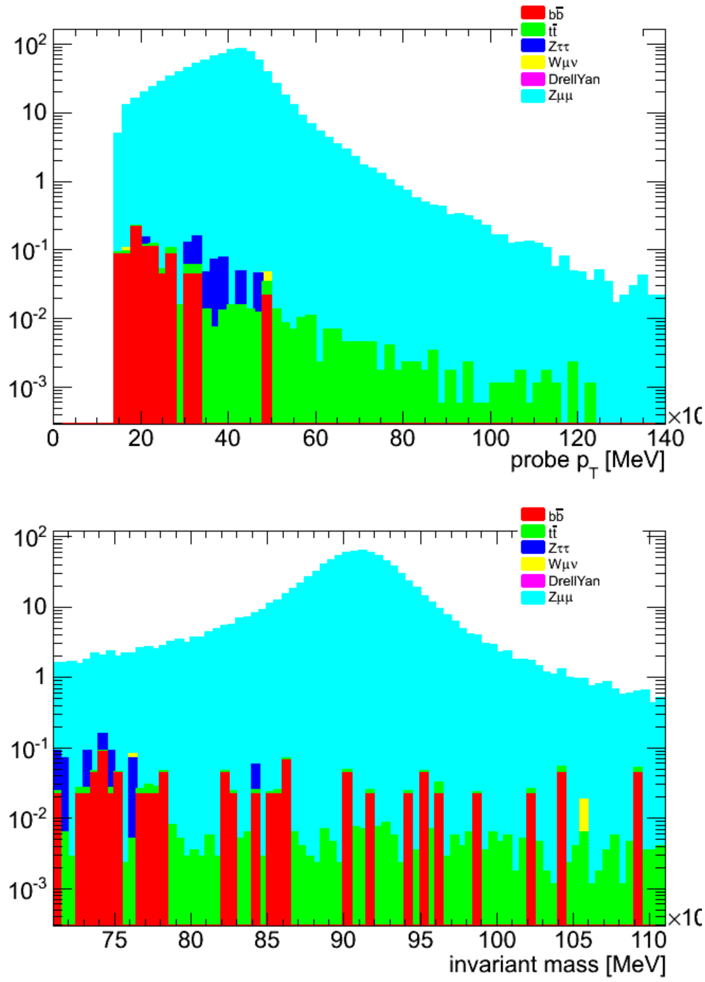

Figure 3.24. Muon probes p_T and invariant mass distribution after the selection. Signal and background contributions are shown.

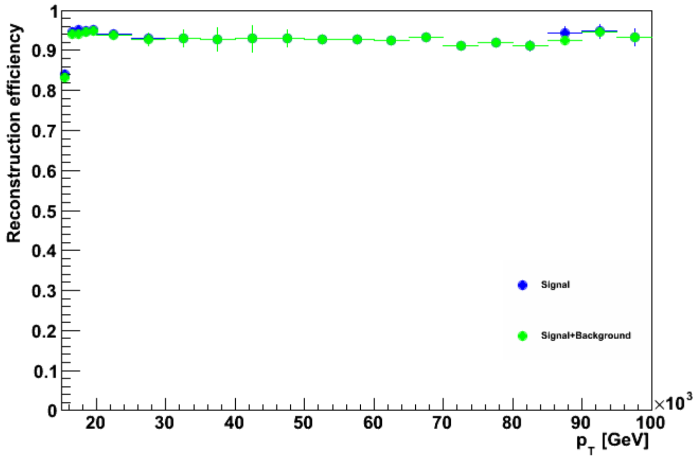

Figure 3.25. T&P reconstruction efficiencies for signal (blue) and signal plus background (green) vs p_T .

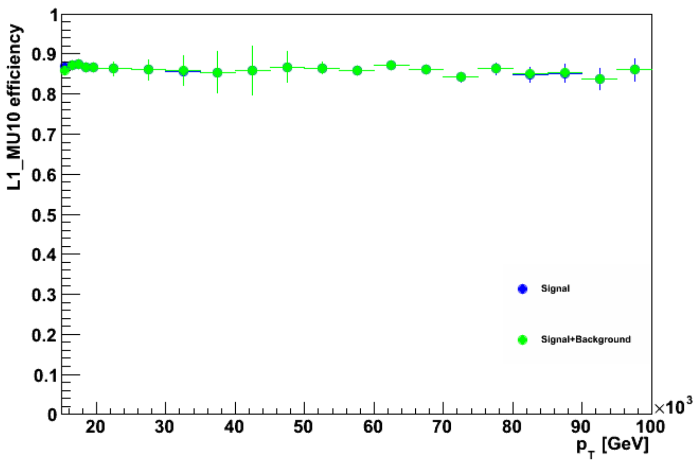

Figure 3.26. T&P relative EF_mu10 trigger efficiencies for signal (blue) and signal plus background (green) vs p_T .

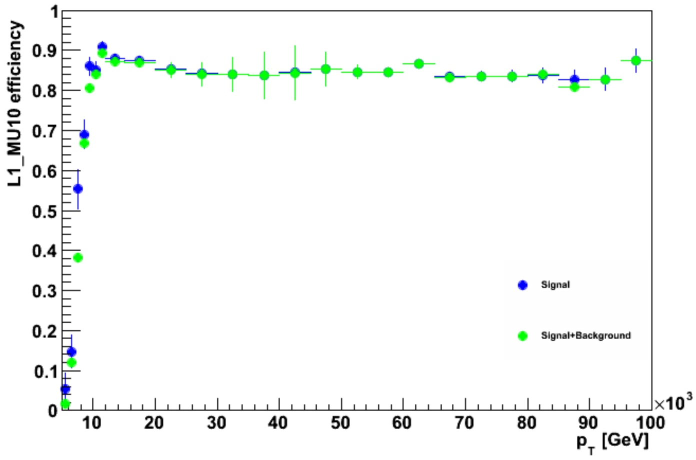

Figure 3.27. T&P absolute EF_mu10 trigger efficiencies for signal (blue) and signal plus background (green) vs p_T .

20 GeV in $|y| < 2.8$, a requirement on the minimal distance between the jet and the closest pre-selected muon (notice that only the pre-selected muons are considered for the analysis).
An isolation requirement is applied which removes all the jets in a cone $\Delta R < 0.5$ around a good muon. This is to reject the events where the same cluster in the calorimeter is identified both as a muon and as a jet, faking the jets counting in the event.

Using this definition both reconstruction and trigger efficiencies have a residual dependence on the jets variables, as one can see from figures 3.28, 3.29 and 3.30, which is however not negligible. This dependence can be due, for example, to some fake combination of the ID and MS tracks when reconstructing the combined muon, due to the high track multiplicity in the ID.
In the next chapter, this dependence will be tested on the data sample and the systematics uncertainty on the efficiencies when neglecting this dependence will be discussed.

3.4 Summary

The Tag&Probe method allows to measure muon trigger and reconstruction efficiencies from data using the $Z \rightarrow \mu^+ \mu^-$ process. After the selection we are left with 706.9 $\pm$ 1.3 per pb^{-1} of Indet probes and 690.5 $\pm$ 0.6 per pb^{-1} of Muon probes, with a background contamination of 0.36 $\pm$ 0.14 % for Indet probes and 0.18 $\pm$ 0.12 % for Muon probes (table 3.7).

This means that with 1 pb^{-1} of integrated luminosity is possible to measure the average efficiencies with a statistical error of 1.0-1.5%. Whenever it would be necessary is possible to bin the efficiencies to avoid to introduce a systematic error in the cross-section measurements or because it is required by some detector effect. In this case the statistical error will scale with the square root of the number of

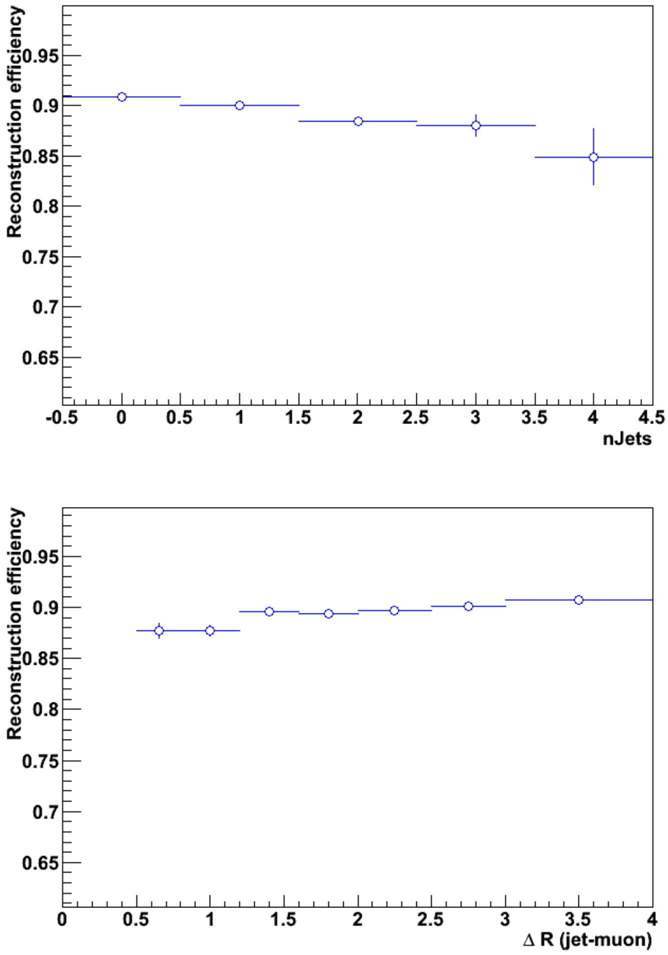

Figure 3.28. Muon reconstruction efficiency vs number of jets in the event and distance between the muon and the closest jet (ΔR).

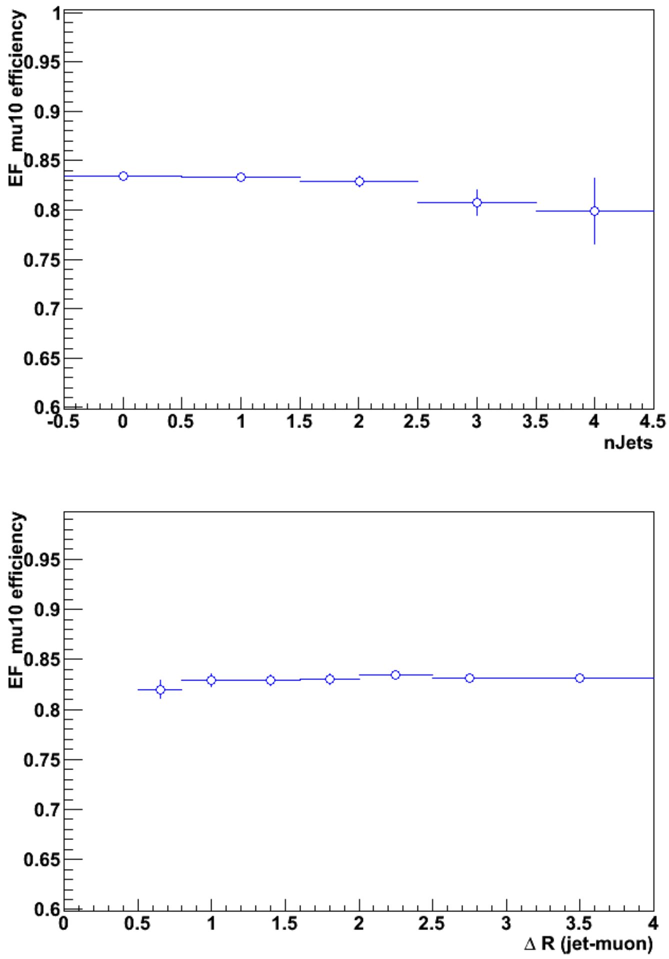

Figure 3.29. Trigger efficiency with respect to offline reconstruction for 10 GeV threshold vs number of jets in the event and distance between the muon and the closest jet (ΔR).

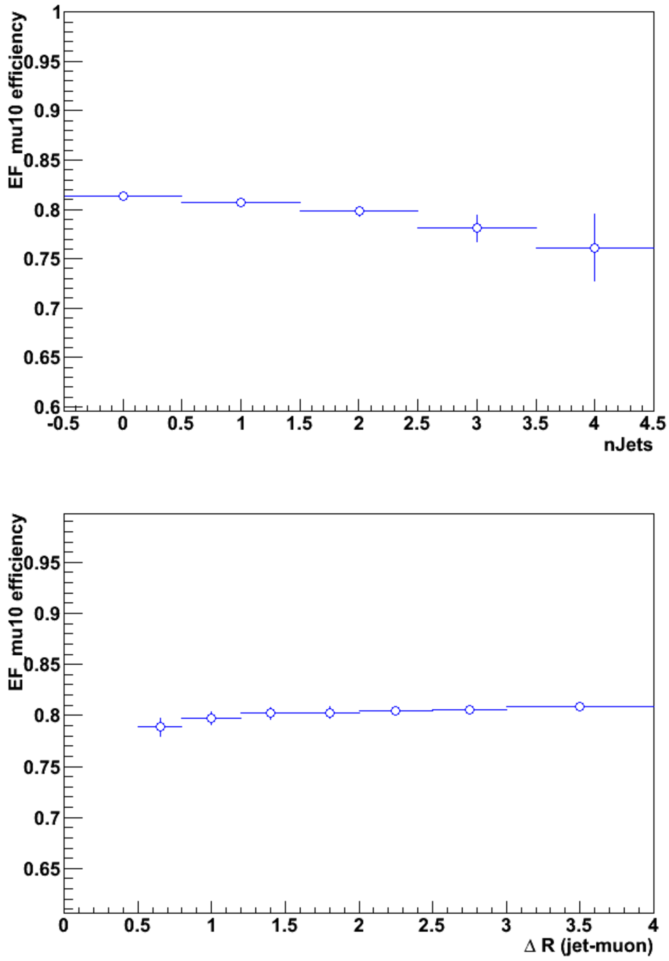

Figure 3.30. Absolute trigger efficiency for 10 GeV threshold vs number of jets in the event, distance between the muon and the closest jet (ΔR).

bins. So the choice of the binning should be a compromise between the detector and physics requirements and the statistical precision is willing to achieve. This item will be discussed in more detail in the next chapter once a binning will be chosen to perform the first measurement with data.

A further systematic uncertainty can come from averaging over the jet multiplicity: this effect will be evaluated and discussed in the next chapter. The actual background contribution have to be estimated from data and so will be discussed in the next chapter as well.

Summary of Selected Probes per pb^{-1}		
Probe Type	Selected	Background
Indet	706.9 ± 1.3	0.36 ± 0.14 %
Muon	690.5 ± 0.6	0.18 ± 0.12 %

Table 3.7. Summary of Indet and Muon probes expected per pb^{-1} of integrated luminosity from MC studies. The numbers include the background contamination, whose estimation is reported too.

Chapter 4

Measurement of Muon Efficiencies with the First pb^{-1}

With the first 0.32 pb^{-1} of data, the first $Z \rightarrow \mu^+ \mu^-$ cross-section measurement at 7 TeV has been performed by the ATLAS collaboration [25]. After the selection 179 candidates have been found and the cross-section in a mass range between 66 and 116 GeV has been estimated to be

$$\sigma(pp \rightarrow Z \rightarrow \mu\mu) \; = \; 0.87 \; \pm 0.08(stat) \; \pm 0.06(syst) \; \pm 0.10(lumi) \; nb$$

in agreement with the theoretical predictions.

At the end of August 2010, the integrated luminosity recorded by the detector reached 1.3 pb^{-1} . On the first 1 pb^{-1} of collected data we performed the first muon efficiencies measurement with the Tag&Probe method. In this chapter the results of such a measurement at 7 TeV are shown and compared to the MC expectations illustrated in the previous chapter.

4.1 Data Sample and Event Selection

This analysis is based on an integrated luminosity data sample of 1.02 pb^{-1} collected between April and August 2010. It is performed running on the so-called "Muon Stream", which contains all the events which have passes one on-line muon trigger. This anyhow does not cause any bias in the measurement because the Tag&Probe method requires one muon have fired the trigger, as it will be explained in the next section.

From each run only a sub-set of luminosity blocks (LBs) is selected using the Good Run List (GRL) mechanism: events are extracted from each run according to some user-defined criteria (which is in general dependent on the specific analysis). In our case the requirements are essentially stable LHC beams and good quality data. In particular the magnets have to be at the nominal voltage, all the sub-detectors have to be in good shape (from data quality tests) and the muon reconstruction algorithms have to be checked working properly. Table 4.1 summarizes the data samples with the respective integrated luminosity after the GRL selection. The error on the absolute value of the luminosity measurement is estimated to be $\sim$ 11%.

Data Samples		
Run Period	Run Number Range	Int. Lumi [nb^{-1}]
A	152166-153200	0.1
B	153565-155160	8.1
C	155228-156682	8.5
D	158045-159224	294.5
E	160387-161948	1003.6

Table 4.1. Summary of the data samples used. Data are collected between April and August 2010. The total integrated luminosity after the GRL selection is 1.32 pb^{-1} , mostly concentrated in the periods D and E. Anyhow, due to some crash running the jobs the effective integrated luminosity used is 1.02 pb^{-1} .

Collision events are then selected by requiring the event to be in time coincidence with a paired LHC proton bunch, i.e. the bunches which are supposed to collide, and to have at least three Inner Detector good quality tracks associated with a reconstructed primary vertex. The good quality criteria require the tracks to have at least one hit in the pixel detector and at least six hits in the semi-conductor tracker.

4.2 Tag&Probe Performance

Event Selection and Muon Pre-Selection

With the described data sample it is possible to measure the muon efficiencies applying the T&P method described in the previous chapter.
After the GRL selection we are left with about 22 million events and about 17 million of them passing the event selection. In this sample we can find 41377 tags and 6104 muons passing the pre-selection. Table 4.2 shows the cut-flow of the muon pre-selection in data, compared to the MC expectations, signal plus backgrounds (table 3.1), normalized to the data luminosity.

Indet and Muon probes selection

Table 4.3 summarizes the cut-flow of the probes selection (Indet and Muon) for data, compared to the MC expectations, signal plus background, normalized to the data integrated luminosity.

At the end of the selection we are left with 744 Indet probes to measure the absolute trigger and reconstruction efficiency and with 677 Muon probes to measure the relative trigger efficiency.

The number of selected probes has to be compared with the MC expectation. Both Indet probes, which were expected to be 721.0 $\pm$ 1.1, and the Muon probes, which were expected to be 704.19 $\pm$ 0.47, are in a good agreement within one sigma. Anyhow we need to take in mind that no correction is applied to the MC expectations to correct for the actual detector performance yet, both in the cut-flows and in the following plots.

Muon Pre-Selection Summary		
Cut	Data	MC
Initial Muons	8331142	8536.35
Type	5301581	7456.18
p_T cut	25248	5889.76
η	25221	5807.32
Track Isolation	10119	5709.01
Track Quality	8397	5645.76
p_T resolution	7460	5608.11
Standalone p_T	7376	5607.54
d_0	6105	5599.09
z_0	6104 ± 78	5597.2 ± 3.1

Table 4.2. Muon pre-selection cut-flow, data and MC expectations, signal plus background. MC is normalized to the data integrated luminosity (1.02 pb^{-1}). Reminder: here the muon type is *combined*.

Figures figure 4.1 and 4.2, show the tag-probe invariant mass distribution before the mass cut, for Indet and Muon probes respectively. In both of them it's clearly visible the Z boson peak around 91 GeV , which in data is a little bit larger than the MC one and it is shifted at lower mass. The first effect can be due to the muon momentum resolution, which in data seems to be worse than in the MC simulation. This is a temporary effect due to the fact that the calibration constants of the muon reconstruction chambers are not the final ones and also the work to provide a correct alignment of the muon spectrometer from data, absolute and with respect to the inner tracker, is on-going. Both these effects will be corrected with the 2010 full data sample and this is expected to improve the muon momentum resolution.
The shift of the Z peak on the left is mainly due to the calibration of the momentum scale of the muon which again is currently in progress, because till now not enough data have been available to perform this task.

In the Indet p_T distribution before the mass cut (figures 4.3, upper plot) can be found a discrepancy, which also reflects in an excess in the low Z mass range. This indicates the presence of some other background contribution in addition to those simulated by MC. Probably this is a QCD effect which can be studied using the appropriate MC samples. This also causes the disagreement in the data/MC cut-flow. After the mass cut the most of this background is anyhow removed, being in the low-p_T region, and data agree with the MC expectations (figures 4.3, lower plot). With the available statistics is not yet possible to perform an accurate evaluation and subtraction of this background, but an effort is on-going to study a data-driven method to do it with more luminosity, as will be explained in section 4.8.
The background contamination is less relevant in the Muon probes p_T distribution (figures 4.4), due to the tighter selection cuts, as expected.
Moreover a strange bump in the Indet invariant mass distribution has been found, maybe due to some event double-counting, which is under investigation.

Figures 4.5 and 4.6 show how both Indet and Muon probes distribute in η and ϕ after the mass cut, in agreement with the MC expectations again.

Event Selection		
Cut	Data	MC
Initial Events	24105444	–
GRL	21793697	–
Event Selection	17247073	–
Tags	41377	14186.47
Indet Probes Selection		
Cut	Data	MC
Type	4796385	1039601.08
Tag removal	4755008	1025414.62
p_T	176497	41544.52
$\|\eta\|$	176201	41407.68
Charge	34278	7843.24
d_0	30276	6838.13
Δz_0	30276	6838.13
Track Isolation	10082	2480.58
$\Delta\Phi$	5610	1684.80
CaloMuon	1373	1026.87
ΔM	744 ± 27	721.0 ± 1.1
Muon Probes Selection		
Cut	Data	MC
Type	5883	5538.81
Charge	1027	982.71
Δz_0	969	965.81
$\Delta\Phi$	833	828.55
ΔM	677 ± 26	704.19 ± 0.47

Table 4.3. Probes selection cut-flow, data and MC expectations. MC is normalized to the data integrated luminosity (1.02 pb^{-1}). The di-jet QCD background is missing in the MC simulation, which causes a disagreement between data and MC cut-flow. Nevertheless this background is concentrated in the low-p_T region (see text) and then is removed by the mass cut, which restore the data/MC agreement.

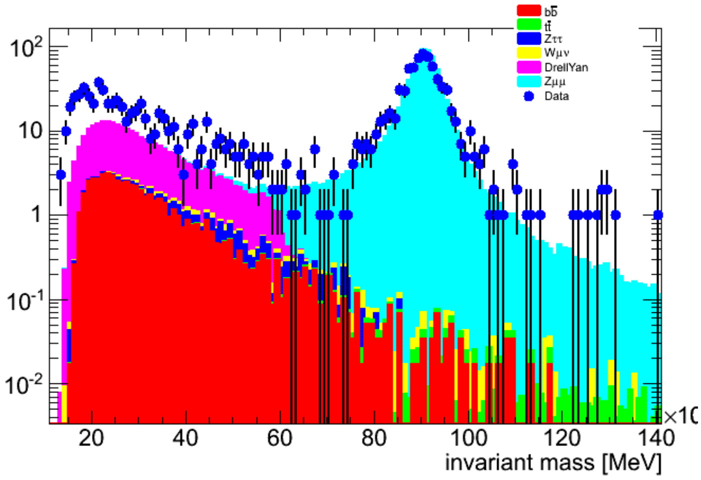

Figure 4.1. Invariant mass distribution of the tag and probe pair for Indet probes, before the cut on the invariant mass. The plot clearly shows the Z boson peak. The MC expectations (filled histograms) are normalized to the data luminosity.

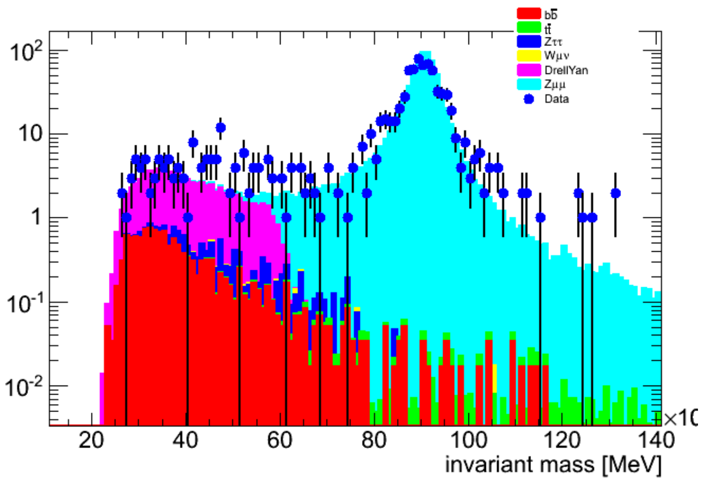

Figure 4.2. Invariant mass distribution of the tag and probe pair for Muon probes,before the cut on the invariant mass. The plot clearly shows the Z boson peak. The MC expectations (filled histograms) are normalized to the data luminosity.

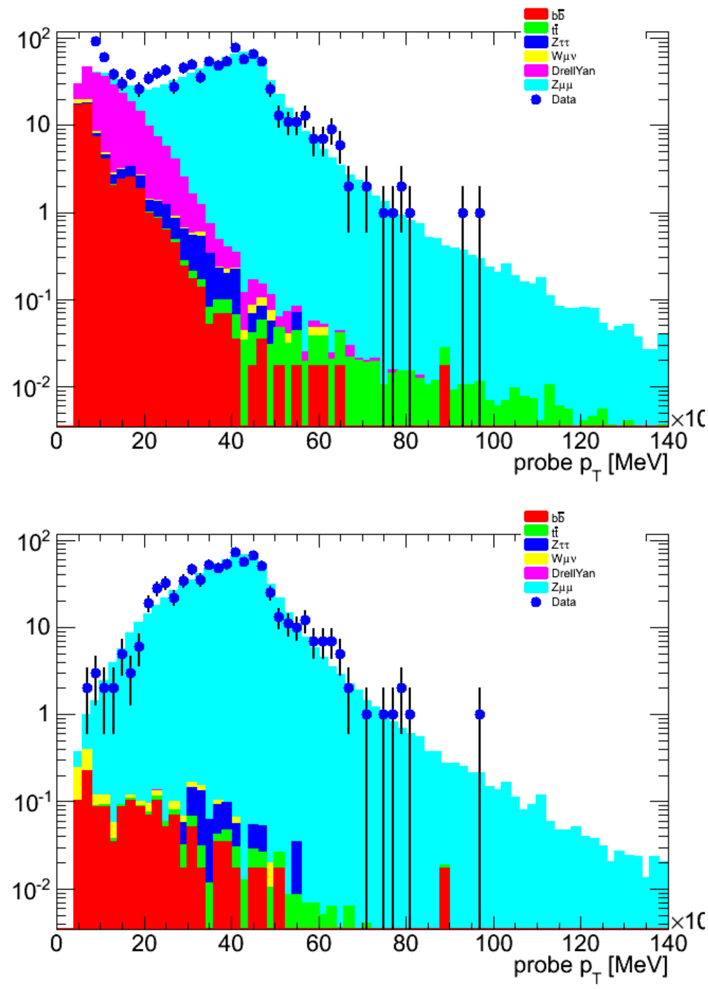

Figure 4.3. Transverse momentum distribution of the Indet probes, before (upper plot) and after (lower plot) the cut on the invariant mass. The MC expectations (filled histograms) are normalized to the data luminosity.

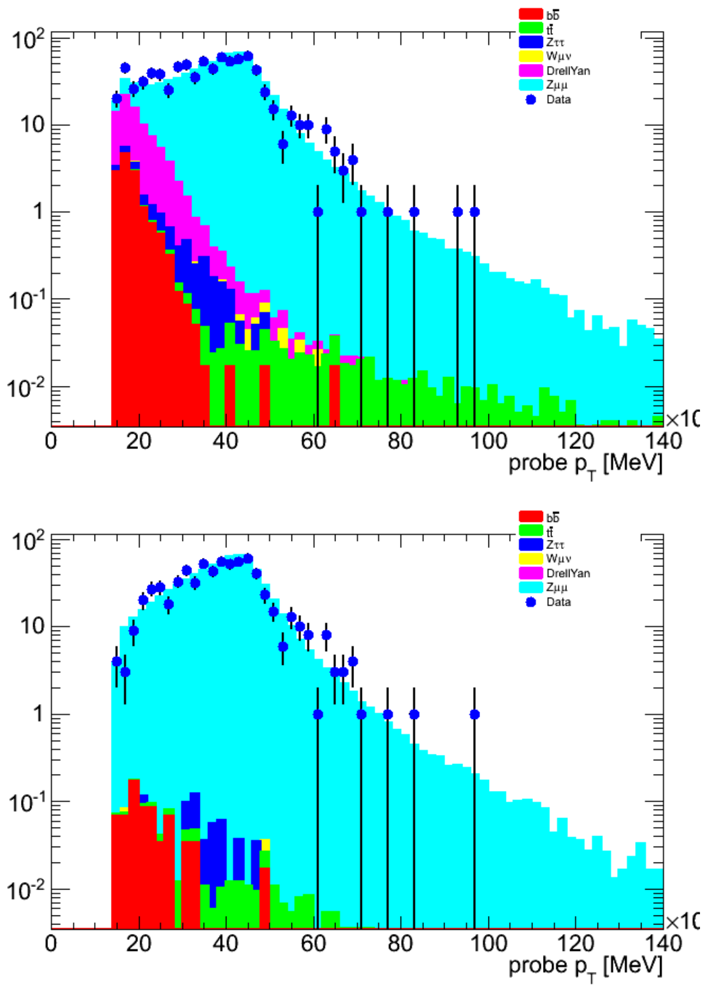

Figure 4.4. Transverse momentum distribution of the Muon probes, before (upper plot) and after (lower plot) the cut on the invariant mass. The MC expectations (filled histograms) are normalized to the data luminosity.

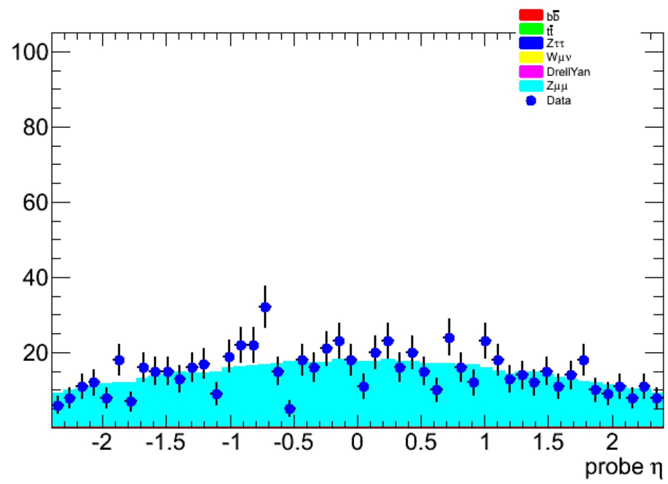

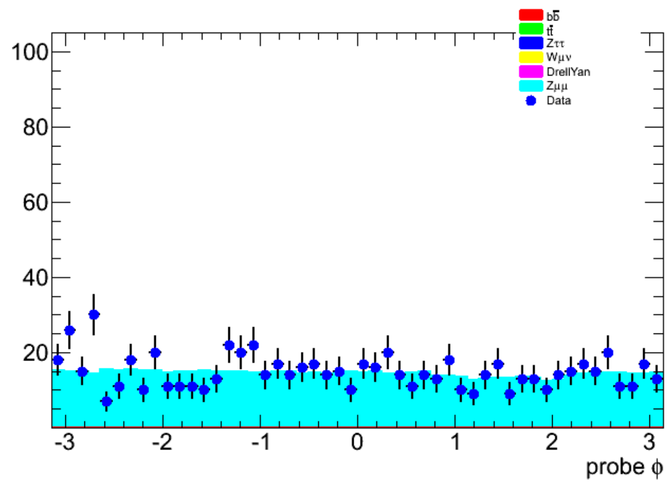

Figure 4.5. Distribution of the Indet probes' η (upper plot) and ϕ (lower plot). The MC expectations (filled histograms) are normalized to the data luminosity.

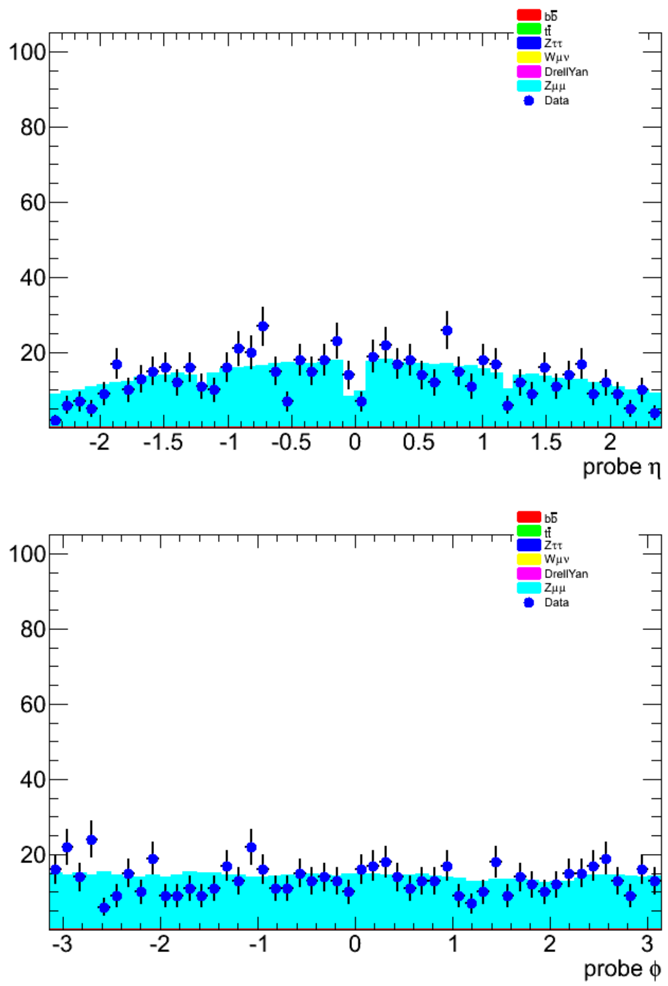

Figure 4.6. Distribution of the Muon probes' η(upper plot) and ϕ (lower plot). The MC expectations (filled histograms) are normalized to the data luminosity.

4.2.1 Reconstruction and Trigger Efficiencies

Once the probe collections are built, we can measure the muon efficiencies. The choice of the phase-space binning is quite important: it has to be a compromise to reach a reasonable statistical error without introducing a bias in the measurement, taking into account the fact that the detector is not homogeneous. Anyhow the choice can be different if one is interested in using the data efficiency itself or the scale factor (SF), defined as the ratio between data and MC efficiencies:

$$SF = \frac{\epsilon_{data}}{\epsilon_{MC}}$$

In the following data efficiencies and scale factors for reconstruction and trigger will be presented. The trigger item discussed in the following will be the L1_MU10 because this is the one used for the first W/Z cross-secion measurement.

Due to the fact that the trigger timing alignment was not yet completed in the analyzed data-sample, data have been acquired with the L1 trigger ROIs spread over three bunch-crossings (3 BC) instead of the nominal one (1 BC). In order to properly take into account this issue, the ROIs for the trigger matching are directly taken from the *Muon Central Trigger Processor* (MuCTPI), which collects all the ROIs from the muon system, instead of the usual *Central Trigger Processor*, which only collects the in-time ROIs from all the ATLAS sub-detectors: this allows to consider also the out-of-time ROIs. Then the matching is done in the usual way with the ΔR cone as for MC.

From MC studies, the **reconstruction efficiency** is expected to be flat in p_T (figure 3.8). This behavior is confirmed by data, as shown in figure 4.7, where all bins are compatible within the statistical error. Only the first bin has a slightly lower efficiency, feeling the effect of both the background contamination (see next section) and the resolution: the selected Indet probes are required to match a combined muon with a p_T greater than 15 GeV , but a track with slightly more than 15 GeV can be reconstructed as a combined muon with slightly less than 15 GeV and then not selected and this causes an inefficiency. This effect is different in data and MC because the resolution in data is worse than the MC expectations, as already discussed. Nevertheless, due to the statistics available we will integrate over p_T and use the average value.

The same is true for the ϕ dependence which can be considered flat (figure 4.8). So it's possible to take also in ϕ the average value both for data efficiency and for scale factors.

Conversely the same is not true for the η distribution already from the MC studies (figure 3.9). Looking at the regions where the spectrometer is less efficient (around $|\eta| \sim 0$ and $|\eta| \sim 1.2$), figure 4.9, we find that with the available statistics the efficiencies in the transition regions around $|\eta| \sim 1.2$ are compatible with the plateau value and can be annexed to the end-caps regions. On the other hand the crack region around $|\eta| \sim 0$, despite the poor statistics, shows a genuine efficiency drop effect so can be treated separately. Re-binning in such a way (figure 4.10) one gets the efficiencies and scale factors summarized in table 4.4. It has to be noticed that the SF in the crack region is greater than 1, i.e. the data η efficiency is better

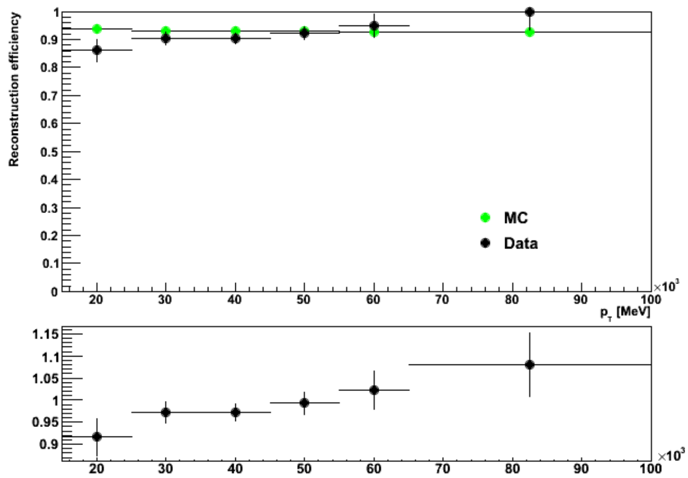

Figure 4.7. Reconstruction efficiencies for data (black) and MC (green) vs p_T . In the bottom figure there is the data/MC ratio (SF).

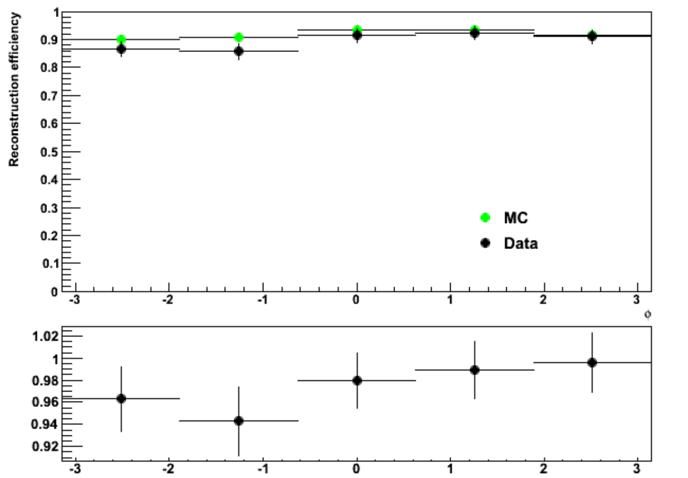

Figure 4.8. Reconstruction efficiencies for data (black) and MC (green) vs ϕ. In the bottom figure there is the data/MC ratio (SF).

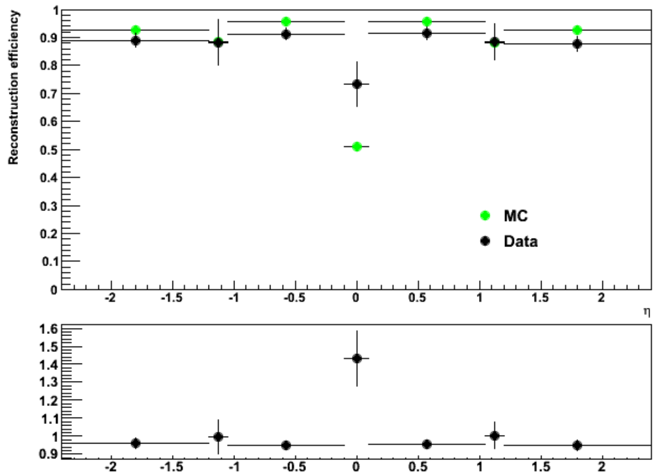

Figure 4.9. Reconstruction efficiencies for data (black) and MC (green) vs η. In the bottom figure there is the data/MC ratio (SF).

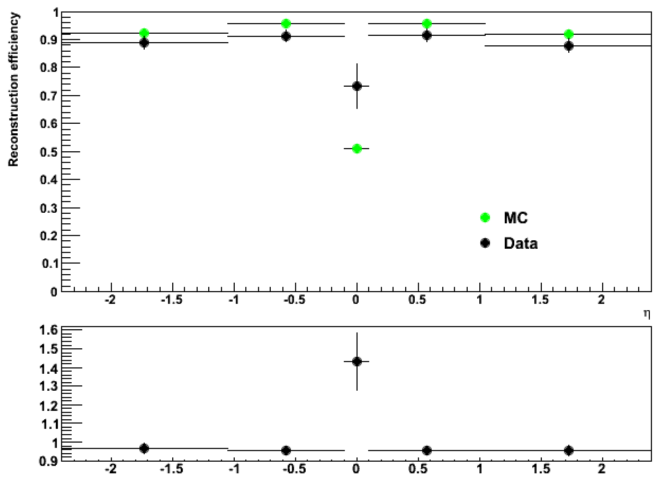

Figure 4.10. Reconstruction efficiencies for data (black) and MC (green) vs η. In the bottom figure there is the data/MC ratio (SF).

than the MC expected one. This is due to a resolution effect: when a muon is close to the crack region, it can be reconstructed as inside the crack region. This happen more often in data with respect to the MC because the resolution in data is worse. This explains why the crack region seems to be more efficient and the resulting SF is greater than 1.

Reconstruction Efficiencies				
Region	η value	Data	MC	Scale Factor
Barrel	$0.1 < \lvert\eta\rvert < 1.05$	0.92 ± 0.02	0.9636 ± 0.0008	0.95 ± 0.02
End-Caps	$1.05 < \lvert\eta\rvert < 2.4$	0.91 ± 0.03	0.942 ± 0.001	0.96 ± 0.01
Crack	$\lvert\eta\rvert < 0.1$	0.73 ± 0.08	0.514 ± 0.005	1.43 ± 0.15
Average	$\lvert\eta\rvert < 2.4$	0.91 ± 0.01	0.9511 ± 0.0005	0.96 ± 0.01

Table 4.4. Summary of data and MC reconstruction efficiencies and scale factors. The binning in η is chosen to follow the detector geometry compatibly with the available statistics. The values are integrated over p_T and ϕ following the considerations made in the text.

The **relative trigger efficiency** can also be considered flat in p_T and ϕ (figures 4.11 and 4.12), So as in the reconstruction case, we can integrate over these two variables.

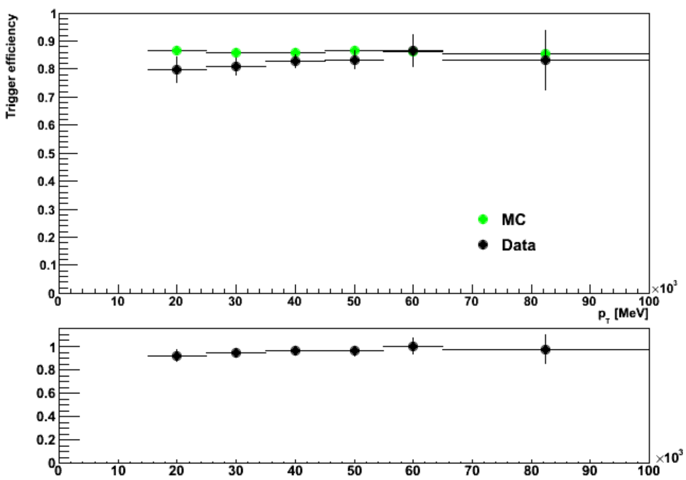

Figure 4.11. Relative L1_MU10 trigger efficiencies for data (black) and MC (green) vs p_T . In the bottom figure there is the data/MC ratio (SF).

Conversely the η distribution, figure 4.13, shows a clear discrepancy between the barrel and the end-caps regions, both in the data efficiencies and in the scale factors. In fact, while in the barrel the actual performance match quite well the MC expectations, in the end-caps regions there is an $\sim$ 10 % difference and the data efficiency is significantly lower than expected.

Due to this fact at least a distinction between the two regions is required and

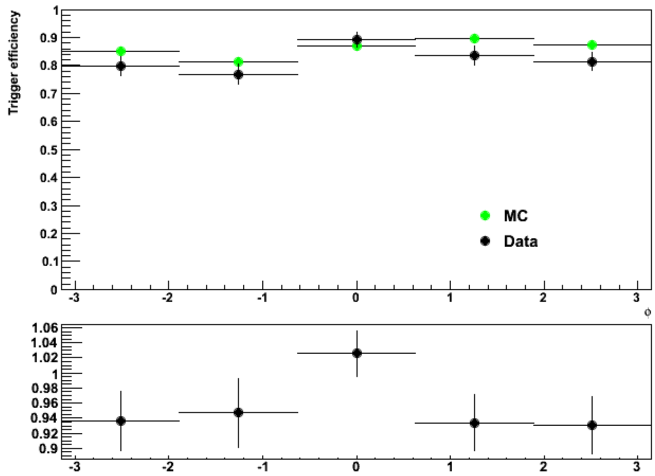

Figure 4.12. Relative L1_MU10 trigger efficiencies for data (black) and MC (green) vs ϕ. In the bottom figure there is the data/MC ratio (SF).

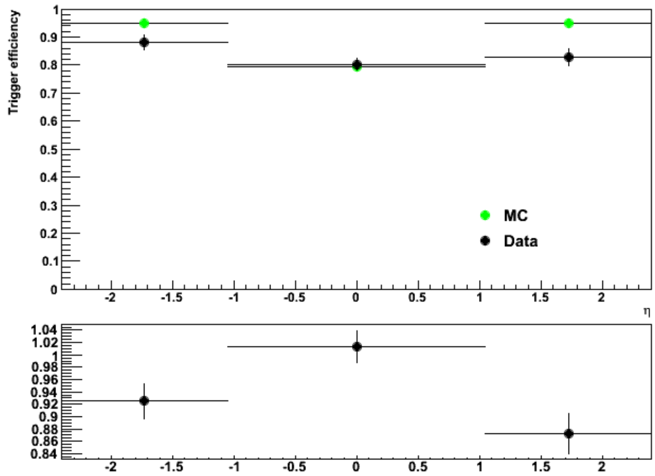

Figure 4.13. Relative L1_MU10 trigger efficiencies for data (black) and MC (green) vs η. In the bottom figure there is the data/MC ratio (SF).

the efficiencies that one gets are summarized in table 4.5.

Relative Trigger Efficiencies L1_MU10				
Region	η value	Data	MC	Scale Factor
Barrel	$\|\eta\| < 1.05$	0.80 ± 0.02	0.793 ± 0.001	1.01 ± 0.03
End-Caps	$1.05 < \|\eta\| < 2.4$	0.85 ± 0.03	0.950 ± 0.009	0.90 ± 0.03
Average	$\|\eta\| < 2.4$	0.83 ± 0.01	0.9142 ± 0.0006	0.95 ± 0.02

Table 4.5. Summary of L1_MU10 relative trigger efficiencies and scale factors. The binning in η is chosen to follow the detector geometry compatibly with the available statistics. The values are integrated over p_T and ϕ following the considerations made in the text.

Finally the **absolute trigger efficiency** shows a more complex behaviour. As in the previous cases there is no clear dependence on the ϕ variable within the statistical errors, figure 4.14.

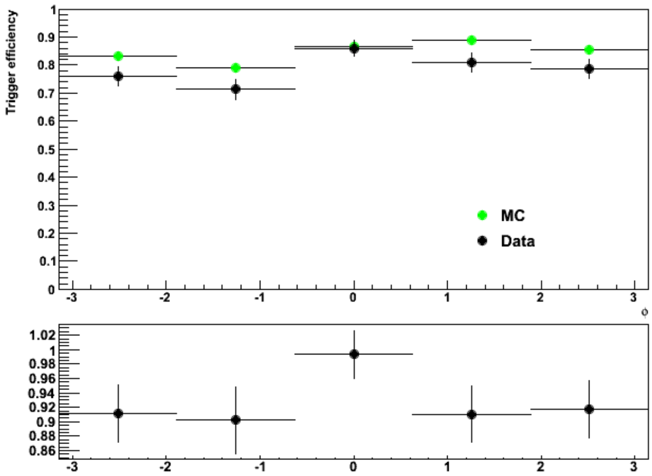

Figure 4.14. Absolute L1_MU10 trigger efficiencies data (black) and MC (green) vs ϕ. In the bottom figure there is the data/MC ratio (SF).

The p_T shape, figure 4.15, feels the effect of the characteristic turn-on near the trigger threshold (10 GeV in this case), as expected from MC studies (figure 3.11), but the effect is not pronunced due to the small statistics available.

The η distribution shows the same behaviour as in the relative trigger case, figure 4.16: also in this the agreement between data and MC is quite good in the barrel and is worse in the end-caps regions.

The study of the absolute trigger efficiency is interesting from the detector performance point of view, also to unfold the reconstruction from the trigger performance. Nevertheless these efficiencies are not used to correct the distributions for cross-section measurement, where only the relative trigger ones are needed. For this reason the binning is needed only to compare data and MC expectations in

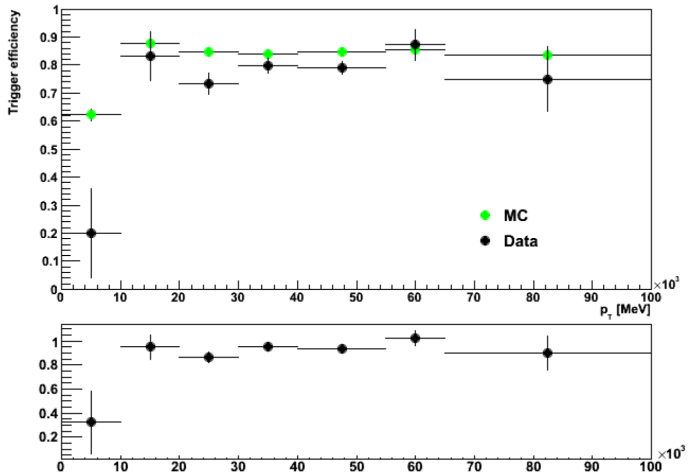

Figure 4.15. Absolute L1_MU10 trigger efficiencies data (black) and MC (green) vs p_T . In the bottom figure there is the data/MC ratio (SF).

phase-space regions. In table 4.6 are given the average values of efficiencies and scale factors in barrel and end-caps regions.

Absolute Trigger Efficiencies L1_MU10				
Region	η value	Data	MC	Scale Factor
Barrel	$\lvert\eta\rvert < 1.05$	0.74 ± 0.02	0.750 ± 0.001	0.99 ± 0.03
End-Caps	$1.05 < \lvert\eta\rvert < 2.4$	0.85 ± 0.03	0.9505 ± 0.009	0.89 ± 0.03
Average	$\lvert\eta\rvert < 2.4$	0.80 ± 0.02	0.9072 ± 0.0006	0.93 ± 0.02

Table 4.6. Summary of absolute L1_MU10 trigger efficiencies and scale factors. The values are integrated over p_T and ϕ following the considerations made in the text.

The $\sim 10\%$ discrepancy in the end-caps region between data and MC expectations has been found to be partially due to trigger roads configuration, which have been reduced in data to avoid a too high trigger rate. This has been already fixed and a 4% gain in TGC efficiency has already been seen in the new runs, which are not included in this thesis.

4.3 Systematics Studies

Possible sources of systematic errors, which affect the efficiency measurement, can be due to both the probe selection and the background contamination. Moreover the integration over the other event variables, e.g. jet multiplicity and distance between jets and muons, can lead to an efficiency bias depending on the topology of the events. In order to study these effects,the dependence of the efficiencies on jets variables is also discussed in the following.

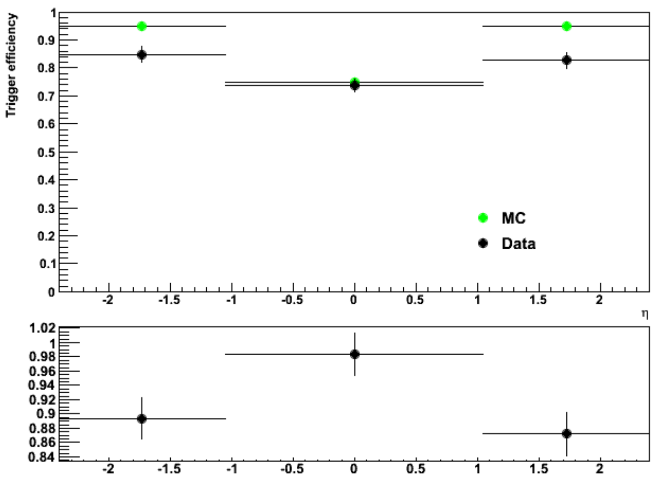

Figure 4.16. Absolute L1_MU10 trigger efficiencies data (black) and MC (green) vs η. In the bottom figure there is the data/MC ratio (SF).

4.3.1 Background Estimation from Data

From Monte Carlo studies the background contamination is 0.36 ± 0.14 % for Indet probes and 0.18 ± 0.12 % for Muon probes. It is mainly dominated by the QCD precesses ($b\bar{b}$) in both Indet and Muon selection and concentrated in the low-p_T region. Nevertheless its effect is already visible in the efficiencies in the region around 20 GeV (figure 4.7). So in this section we will present a first data-driven method to estimate the background, especially due to the theoretical uncertainties on the QCD cross-sections.

In some of the background processes taken into account for this study, the two tracks passing the selection (tag and probe) are not correlated in charge sign. This means that in principle there is the same probability to have the two tracks with the *same-sign* (SS) or with the *opposite-sign* (OS). This is for example true for the most of the QCD background where the tag and the probe can came from two uncorrelated different processes. But the same is also true for the $W \rightarrow \mu\, \nu$ process where one of the two muons comes from the W decay while the other one is a fake muon selected from the underlying event.
Thise means that the number of background events passing the signal selection with the OS requirement, is the same that would passes the same selection but with the SS requirement. So this type of background can be evaluated from data just reverting the OS requirement in the selection with the SS one and counting how many of them are selected.

This method can be already exploited with the available data to determine a first background estimation despite the big statistical errors. Applying it we select only 5 events from the Indet sample, which means a background contamination in the standard selection of 0.7 ± 0.3 % for Indet probes, table 4.7. No events are selected in the Muon probes sample at all.

Figure 4.17 shows how this background is distributed in p_T and invariant mass,

Same-Sign Probes with $1.02\ \mathrm{pb}^{-1}$		
	Indet probes	Muon probes
# selected SS probes	5	0
Background estimation	0.7 ± 0.5 %	–

Table 4.7. Background estimation with SS/OS method from data ($1.02\ \mathrm{pb}^{-1}$). Number of selected same-sign probes from Indet and Muon sample and corresponding expected background in the signal region.

which is what we expected from MC (figures 3.23 and 3.24).

This method doesn't provide an estimation of the background which generate charge-sign correlated muons, such as the $t\bar{t}$ or the $Z \to \tau^+\tau^-$. With more integrated luminosity available, more sophisticated methods to estimate such backgrounds from data can be exploited. At this stage, for this processes we decided to rely on the MC expectations and we get (see table 3.5) 3.3 ± 1.3 events in the Indet selection and 1.6 ± 1.0 events in the Muon selection in $1.02\ \mathrm{pb}^{-1}$ of data.

4.3.2 Selection Cuts

The background contamination and the possible presence of some detector dead-regions, can introduce a systematic error in the efficiency measurement. In order to estimate this uncertainty the selection cuts are varied in a range around the nominal value, and the maximum variation of the average efficiency is observed and used used as an estimation of these uncertainties. This procedure has been applied to the data sample of $1.02\ \mathrm{pb}^{-1}$ and the systematics obtained are summarized in table 4.8. For both type of probes, the cuts based on the kinematical correlation between the tag and the probe, i.e. Δz_0, $\Delta\Phi$ and ΔM, are considered to check whether the kinematic of the Z biases the measurement. No further contributions are considered for the Muon probes because all the other cuts applied in the selection are part of the muon definition the efficiencies have to be measured for. On the other hand additional sources of systematic uncertainty are considered for the Indet probes, varying also the d_0 and the track isolation cut.

The d_0 cut applied to the Indet probes has been changed tightening and loosening it within a range of the same order of magnitude of the detector resolution, which means 50 μm. This leads to a 0.1% variation of the reconstruction efficiency and to a 0.1% variation of the absolute trigger efficiency. The relative trigger efficiency is unchanged because the cut hasn't been change in the Muon probes definition.

The isolation cut is expected to have a big influence on the efficiency determination, especially for the reconstruction efficiency because we are testing isolated muons (so it's easier to find a matching if we require also the probe to be isolated). So in a conservative way we can change it of a factor 2 in both directions and the observed effect is 1.5% variation of the reconstruction efficiency and 0.6% of the absolute trigger efficiency. Again it has no influence on the relative trigger efficiency because the Muon probes are untouched.

The detector resolution on the Δz_0 variable is around 200 μm: changing the cut

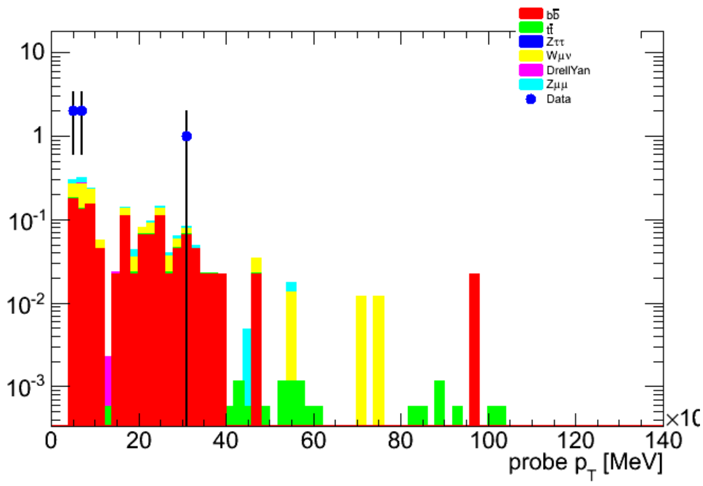

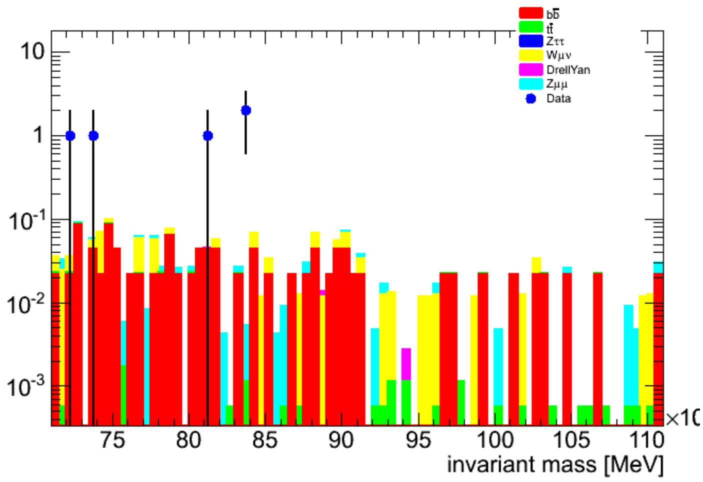

Figure 4.17. Distribution of same-sign Indet probes vs. p_T (upper plot) and invariant mass (lower plot) probes, for data and MC.

value in this range we observe a 0.1% variation of the reconstruction efficiency, 0.5% of the absolute trigger efficiency and 0.3% of the relative trigger efficiency.

Concerning the $\Delta\Phi$, the nominal value of 2.14 it has already been chosen to be quite loose (figure 3.3). So the larger effect of the efficiencies should appear tightening it. A meaningful choice could be 2.6 because this is the point where the signal becomes dominant with respect to the background. Doing this we observe a 0.5% variation of the reconstruction efficiency, 0.7% of the absolute trigger efficiency and 0.4% of the relative trigger efficiency.

Finally tightening the mass cut from 20 GeV to 12 GeV and 8 GeV to further reduce the background contamination we get a 0.6% variation of the reconstruction efficiency, 0.8% of the absolute trigger efficiency and 0.7% of the relative trigger efficiency, so no big effect.

Systematic Uncertainties			
Cut	Reconstruction Efficiency	Absolute Trigger Efficiency	Relative Trigger Efficiency
d_0	0.1%	0.1%	–
Isolation	1.5%	0.6%	–
Δz_0	0.1%	0.5%	0.3%
$\Delta\Phi$	0.5%	0.7%	0.4%
ΔM	0.3%	0.8%	0.7%
	1.6%	1.3%	0.9%

Table 4.8. Systematics uncertainties on efficiencies measurement. The uncertainties are evaluated varying the selection cuts in the range explained in the text and estimating the corresponding maximal average efficiency variation.

Thus the squared sum of all systematic uncertainties to the efficiencies measurement gives a 1.6% variation of the reconstruction efficiency, 1.1% of the absolute trigger efficiency and 0.9% of the relative trigger efficiency.

4.3.3 Jet Variables

When the inclusive cross-section is measured, the efficiencies dependence on the additional variables in the event can be neglected. On the other hand if the differential cross-section of a process is considered with respect to some variable, the dependence of the efficiencies on such a variable has to be checked, because otherwise it can introduce a bias in the measurement.

Let's consider the case of the differential Z cross-section with respect to the number of jets in the event, which will be discussed in more detail in the next chapter. For this analysis we need to check the dependence of the muon efficiencies on the number of jets in the event, in order to understand if a different efficiency for each jet multiplicity is needed or the average value is enough.

Figures 4.18, 4.19 and 4.20 show such a muon efficiencies dependence from the number of jets in the event for data and MC and the respective scale factors. While is visible a discrepancy between data and MC expectations, as already observed and discussed in the previous section, a dependence of the data efficiencies on the number of jets is not clearly visible with the statistics available for this analysis.

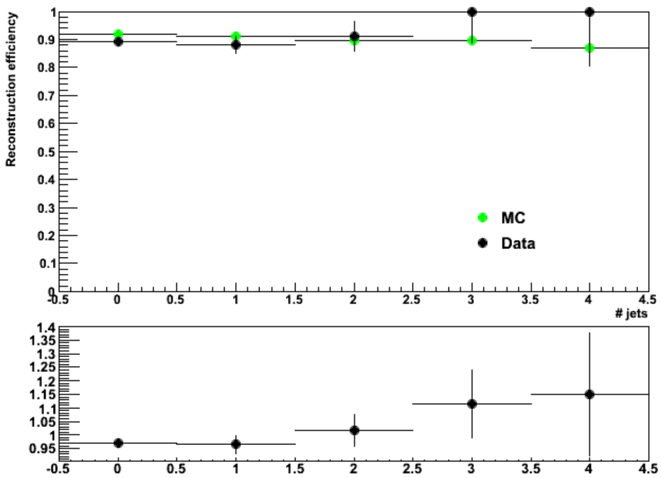

Figure 4.18. Muon reconstruction efficiency vs number of jets in the event for data (black) and MC (green) and the data/MC scale factor.

In table 4.9 the reconstruction and trigger efficiencies, data and MC, for the events with at least 0, 1, 2, 3 or 4 jets are reported. As expected all the values are compatible within the statistical errors, so we can integrate over the number of jets in the event and use the average value (first row) for the cross-section measurements.

This procedure causes no bias to the cross-section measurement of the inclusive processes by definition, but can lead to a systematic uncertainty when the average value is applied to the measurement of the differential cross-sections where events with different number of jets are considered. For example, in principle for the measurement of the $Z \rightarrow \mu^+ \mu^-$ production in association with one or more jets one should use the efficiency calculated with one or more jets in the events (second row). A possible systematic uncertainty can be introduced using the average efficiency value. This can be estimated from MC considering the difference between the average value and the binned one (bottom part of table 4.9). Then, once enough statistics will be available, one should consider to calculate the appropriate efficiency or to estimate the same systematics directly from data. Anyhow for the moment the measurement of this process is dominated to the statistic uncertainty, as it will be shown in the next chapter.

4.3.4 Summary

Muon trigger and reconstruction efficiencies have been measured from data with the Tag&Probe method. Using the data sample of an integrated luminosity of 1.02 pb^{-1} , collected between April and August 2010, we get the average efficiencies summarized in table 4.10.

The systematic uncertainties reported in the table have been estimated looking at the efficiencies dependence on the selection cuts. These efficiencies are also

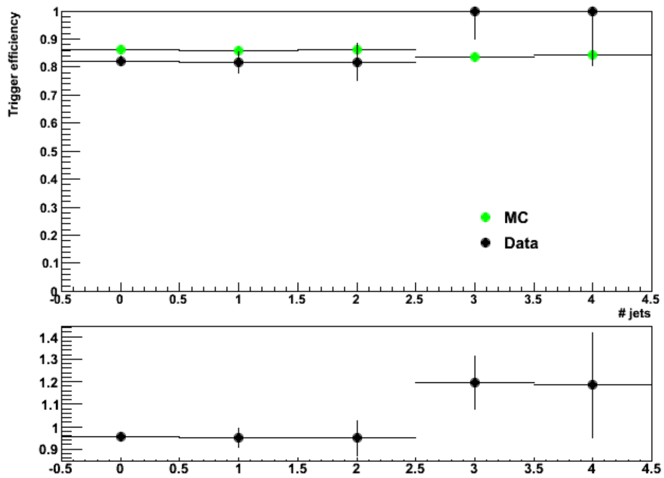

Figure 4.19. Trigger efficiency with respect to offline reconstruction for 10 GeV threshold vs number of jets in the event for data (black) and MC (green) and the data/MC scale factor.

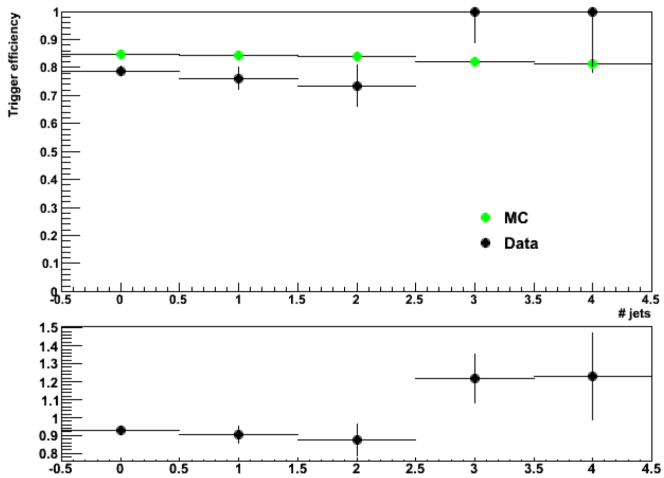

Figure 4.20. Absolute trigger efficiency for 10 GeV threshold vs number of jets in the event for data (black) and MC (green) and the data/MC scale factor.

Efficiencies vs Number of Jets			
Cut	Reconstruction Efficiency	Absolute Trigger Efficiency	Relative Trigger Efficiency
Data			
≥ 0	0.91 ± 0.01	0.79 ± 0.01	0.82 ± 0.01
≥ 1	0.92 ± 0.02	0.78 ± 0.03	0.83 ± 0.03
≥ 2	0.95 ± 0.04	0.82 ± 0.05	0.86 ± 0.05
≥ 3	1.00 ± 0.09	1.00 ± 0.10	1.00 ± 0.08
≥ 4	1.00 ± 0.19	1.00 ± 0.19	1.00 ± 0.19
Monte Carlo			
≥ 0	0.9304 ± 0.0005	0.9047 ± 0.0006	0.8606 ± 0.0007
≥ 1	0.928 ± 0.001	0.901 ± 0.001	0.859 ± 0.002
≥ 2	0.922 ± 0.003	0.892 ± 0.004	0.858 ± 0.004
≥ 3	0.919 ± 0.009	0.862 ± 0.010	0.841 ± 0.011
≥ 4	0.905 ± 0.024	0.892 ± 0.023	0.878 ± 0.026
Systematic Uncertainty			
≥ 1 / ≥ 0	- 0.21%	- 0.35%	- 0.13%
≥ 2 / ≥ 0	- 0.86%	- 1.03%	- 0.22%
≥ 3 / ≥ 0	- 0.12%	- 0.43%	- 0.20%
≥ 4 / ≥ 0	- 0.25%	- 0.13%	+ 0.17%

Table 4.9. Dependence on the muon efficiencies from the number of jets in the event from data and Monte Carlo. Data do not show a statistical significant dependence from the jet multiplicity, so the average value can be considered instead of the binned one. The systematic error introduced integrating over this variable is estimated from the Monte Carlo samples. In the bottom part of the table is reported the difference of the average efficiency for each jet multiplicity with respect to the value with ≥ 0 jets.

Summary of Reconstruction and Trigger Efficiencies		
Type	Data Efficiency	MC Efficiency
Reconstruction	0.91 ± 0.01 (stat) ± 0.016 (syst)	0.9511 ± 0.0005 (stat) ± 0.016 (syst)
Trigger	0.83 ± 0.01 (stat) ± 0.009 (syst)	0.9142 ± 0.0006 (stat) ± 0.016 (syst)

Table 4.10. Summary of L1_MU10 relative trigger efficiency and reconstruction efficiencies from data and MC. The values are integrated over a range $|\eta| < 2.4$.

averaged over the jet multiplicity in the events. Despite the data do not show a clear dependence on such variable, essentially due to the big statistic errors, the use of the average efficiency value is expected to introduce a systematic uncertainty. This uncertainty is evaluated from the MC and reported in table 4.11.

Additional Systematic Uncertainties					
Affected Component	$Z+\geq 0$ jet	$Z+\geq 1$ jet	$Z+\geq 2$ jet	$Z+\geq 3$ jet	$Z+\geq 4$ jet
Reconstruction [%]	-	0.2	0.9	0.1	0.3
Trigger [%]	-	0.1	0.2	0.2	0.2

Table 4.11. Additional systematic uncertainties to be added when neglecting the efficiencies dependence on the jet multiplicity.

A first background estimation has been performed from data using the SS/OS method, which is in agreement with the MC predictions. Anyhow further detailed studies are needed and currently on-going, to estimate not only the sign-uncorrelated backgrounds and to better understand the efficiency behavior in the low-p_T region (under 20 GeV).

Chapter 5

Cross-Section Measurement of $Z \rightarrow \mu^+ \mu^-$ Production with 1.3 pb^{-1}

One of the first measurements where the muon efficiencies measured with the Tag&Probe method have been applied, is the determination of the cross-section of the $Z \rightarrow \mu^+ \mu^-$ process, both inclusive and differential versus the number of jets in the event. This measurement has been performed on a data sample of 1.3 pb^{-1} of integrated luminosity (see [26]). This comparison has been performed both at the particle-level, i.e. accounting for the differences in the real detector performance and the expected ones and at the parton-level, i.e. correcting back the reconstructed distributions to the generation-level distributions. In this chapter the analysis and the particle-level comparison are summarized, stressing how the correction factors measured with the Tag&Probe method are used. Any further detail on the analysis can be found in the cited note.

5.1 Data Sample

The data sample used for the analysis corresponds to an integrated luminosity of 1.3 pb^{-1} collected between April and August 2010 (data periods A to E), the same already described in section 4.1 and summarized in table 5.1. The integrated luminosity corresponding to each period has been evaluated after applying the same Good Run List Selection described in section 4.1.

Events are required to have fired the L1_MU10 trigger and to have at least three Inner Detector good quality tracks, associated with a reconstructed primary vertex, with $|z_0| < 150\ mm$. Good quality tracks meens having at least one hit in the pixel detector and at least six hits in the semi-conductor tracker.

5.2 Monte Carlo Samples

Data results are compared with the MC expectations. The MC signal and background samples used to do this, are generated at $\sqrt{s} = 7$ TeV with PYTHIA [16], Alpgen [22] and MC@NLO [23] using MRSTLO [17] parton distribution functions (PDF). The

Data Samples		
Run Period	Run Number Range	Int. Lumi [nb^{-1}]
A	152166-153200	0.1
B	153565-155160	8.1
C	155228-156682	8.5
D	158045-159224	294.5
E	160387-161948	1003.6

Table 5.1. Summary of the data samples used. Data are collected between April and August 2010 and their integrated luminosity after the GRL selection is 1.32 pb^{-1}.

Process	Generator	Cross-section [nb]	Filter
$Z \rightarrow \mu^+ \mu^-$	Alpgen(+Herwig+Jimmy)	1.07	$M_{ll} > 40$ GeV
$W \rightarrow \mu \nu$	Alpgen(+Herwig+Jimmy)	10.46	lepton filter
$Z \rightarrow \tau^+ \tau^-$	Alpgen(+Herwig+Jimmy)	1.07	$M_{ll} > 40$ GeV
$t\bar{t}$	MC@NLO	0.16	1 lepton with $p_T > 1$ GeV
WZ	Alpgen(+Herwig+Jimmy)	0.00167	lepton filter
ZZ	Alpgen(+Herwig+Jimmy)	0.00103	lepton filter
WW	Alpgen(+Herwig+Jimmy)	0.00445	lepton filter
QCD	Pythia	97.7	1 jet $\|\eta\| < 2.7$, $p_T > 17$ GeV
$b\bar{b}$	Pythia	73.9	1μ, $p_T > 15$ GeV
$c\bar{c}$	Pythia	28.4	1μ, $p_T > 15$ GeV

Table 5.2. Monte Carlo samples used in this note. The cross-sections quoted are the ones used to normalize estimates of expected number of events. Lepton filter means only the leptonic decays are selected at the generation-level.

events are then simulated with GEANT4 [18] and fully reconstructed. Details of these samples are summarized in Table 5.2 with the respective cross-sections and the filter applied at the generation level. The cross-sections for the QCD sample, the $b\bar{b}$ and the $c\bar{c}$ sample are directly from Pythia. The cross-sections for the di-boson samples are taken from Alpgen at LO and scaled with a global k-factor of 1.21 to take into account the possible NLO corrections, and the lepton filter is applied to select only the leptonic decays.

5.3 $Z \rightarrow \mu^+ \mu^-$ Selection

A dedicated selection has been optimized for the analysis of the $Z \rightarrow \mu^+ \mu^-$ events, which is summarized in table 5.3. It essentially requires to have exactly two oppositely charged high-p_T muons ($p_T >$ 15 GeV), reconstructed with the Staco algorithm, isolated in the Inner Detector and with an invariant mass in the range (91 ± 20) GeV. They also have to fulfill some good-quality requirements, stricter than those used in the event selection to get a pure sample. In the following the good quality requirements are described and then the motivations are given:

Collision event selection	
Primary vertex	$N_{vtx} \geq 1$ with $N_{tracks} \geq 3$,, $\lvert z_{vtx} \rvert < 150$mm
Trigger	L1_MU10
Good-muon selection	
Phase space	$p_T > 20$ GeV , $\lvert\eta\rvert < 2.4$
Muon ID	Staco Combined
Muon cleaning	p_T MS > 10 GeV ,
	$\lvert p_T$ (MS) - p_T (ID)$\rvert / p_T$ (ID) < 0.5
	$\lvert z_{muon} - z_{vtx} \rvert < 10\ mm$
	$d_0 < 0.1\ mm$ (wrt. the primary vertex)
	$N_{PIXhits} > 1$, $N_{SCThits} > 5$, $N_{TRThits} > 0$, if $\lvert\eta\rvert < 2$
Track isolation	$\Sigma p_T < 1.8$ in $\Delta R < 2.0$ around the muon track
$Z \rightarrow \mu^+ \mu^-$ event selection	
	Exactly 2 good muons
Charge	Opposite sign
Invariant Mass	$71 < M_{ee} < 111$ GeV

Table 5.3. Event selections for the $Z \rightarrow \mu^+ \mu^-$ analysis.

- **Combined tracks** - A muon candidate has to be reconstructed as a combined track in the Inner Detector and the Muon Spectrometer.
- **Quality requirements** - To ensure the good quality of the muon track, the following criteria are applied
  - The muon track in the Inner Detector is required to have at least two hits in the pixel detector, at least six hits in the SCT detector and for ID tracks with $\lvert\eta\rvert < 2.0$ at least one hit in the TRT detector.
  - The absolute difference between the z-coordinate of the primary vertex, z_{pv}, and the z-position of the muon track extrapolated to the beam line, z_μ, is less than 10 mm ($\lvert z_{\mathrm{pv}} - z_\mu \rvert < 10\ mm$) and the impact parameter, d_0, of the muon track (relative to the primary vertex) is less than 0.1 mm ($\lvert d_0 \rvert <0.1\ mm$).
  - The transverse momentum measured using only the muon spectrometer track, $p_T{}^{\mathrm{MS}}$, is greater than 10 GeV and the absolute difference between the muon spectrometer p_T and the p_T measured using the inner detector, $p_T{}^{\mathrm{ID}}$, is less than $0.5 * p_T^{\mathrm{ID}}$ ($\lvert p_T^{\mathrm{ID}} - p_T^{\mathrm{MS}} \rvert / p_T^{\mathrm{ID}} < 0.5$).
- **Muon isolation** - To reduce backgrounds from multi-jet events, a track-based isolation is required. The sum p_T of inner detector tracks in a cone of $\Delta R < 0.2$ around the muon track must be less than 1.8 GeV . The isolation is calculated using tracks with $p_T > 1$ GeV , within 10 mm from the primary vertex, and with a the total number of Pixel and SCT greater than 3.

The requirement on the number of hits of the inner detector track is applied to remove badly reconstructed tracks (mainly those reconstructed starting from the

TRT detector and back-extrapolated to the interaction vertex), as well as muons coming from decay-in-flight of long-lived particles. This cut is very efficient for the signal, where both muons are actually coming from the primary vertex and crossing all the inner detector layers have a big number of associated hits.

The cut on the longitudinal impact parameter z_0 is effective in rejecting cosmics events in-time with the bunch crossing, while the transverse impact parameter cut d_0 is a powerful cut against muons from heavy-flavor quark decays.

The isolation cut is mainly intended to reject the events with a muons within jets. The cut of 1.8 GeV in a 0.2 cone is chosen to have more than 99% efficiency on the selection of real prompt muons and reject $\sim 80\%$ of the jet background.

Finally in the first data a number of muon tracks with a big discrepancy between the transverse momentum value measured by the ID and the MS have been found. Figure 5.1 shows the transverse momentum measured by the MS as a function of that measured by the ID, for muons with a combined p_T greater than 5 GeV . As can be noticed the number of tracks have a few tens of ID p_T and less than about 5 GeV of MS p_T . To remove these fake tracks, the MS p_T is required to be greater than 10 GeV , and the resolution cut $|p_T^{\rm ID} - p_T^{\rm MS}|/p_T^{\rm ID} < 0.5$ has been added too.

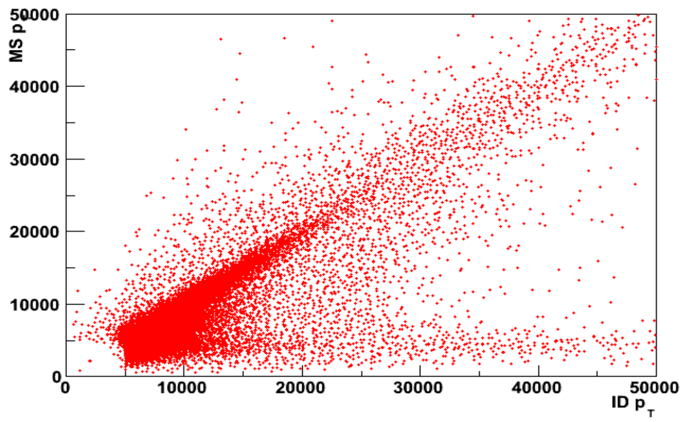

Figure 5.1. Distribution of the muon transverse momentum measured by the the MS and extrapolated to the primary vertex vs the same measured by the ID, for combined muons of a $p_T > 5$ GeV .

Jet Selection

Jets are reconstructed using the Anti-kt algorithm, with calorimeter clusters as input with a distance parameter of $R = 0.4$. They are required to have a transverse momentum greater than 20 GeV in a pseudo-rapidity range of $|\eta| < 2.8$. Jets not associated to in-time energy distributions or related to known calorimeter noise effects, are removed.

An isolation requirement is applied which removes all the jets whose axis is closer than 0.5 ΔR to a good muon. This is to reject the events where the same cluster in the calorimeter is identified both as a muon and as a jet, faking the jets counting in the event.

In order to reject jets stemming from the secondary vertexes in the event (from pile-up), a cut is applied on the jet vertex fraction (JVF). This is defined as the fraction of the sum of the transverse momenta of the tracks associated with a jet, which are coming from the primary interaction vertex, and it is required to be greater than the 75%.

5.4 Detector-Level Results

After the selection described in the previous section, we are left with 430 $Z \rightarrow \mu^+ \mu^-$ candidate events. This number has to be compared to 451.1 ± 1.3, which is the expected number of events, signal plus background, from the MC samples, without any correction. Data and MC expectations for the various inclusive jet multiplicities are summarized in table 5.4. It can be noticed that the MC prediction and the number of data events agree within one standard deviation.

	$Z+\geq 0$ jet	$Z+\geq 1$ jet	$Z+\geq 2$ jet	$Z+\geq 3$ jet	$Z+\geq 4$ jet
$Z \rightarrow \mu^+ \mu^-$	449.6 ± 1.3	101.6 ± 0.6	26.6 ± 0.3	6.8 ± 0.1	1.7 ± 0.1
$W \rightarrow \mu\, \nu$	0.03 ± 0.01	0.01 ± 0.01	< 0.01	< 0.01	< 0.01
$Z \rightarrow \tau^+ \tau^-$	0.11 ± 0.02	0.02 ± 0.01	0.01 ± 0.01	0.01 ± 0.01	0.01 ± 0.01
WW, WZ, ZZ	0.61 ± 0.01	0.48 ± 0.01	0.32 ± 0.04	0.140 ± 0.003	0.048 ± 0.001
$t\bar{t}$	0.72 ± 0.01	0.71 ± 0.01	0.63 ± 0.01	0.34 ± 0.01	0.13 ± 0.01
$b\bar{b}$	0.07 ± 0.04	0.02 ± 0.02	< 0.02	< 0.02	< 0.02
$c\bar{c}$	< 0.02	< 0.02	< 0.02	< 0.02	< 0.02
Total predicted	451.1 ± 1.3	102.8 ± 0.6	27.6 ± 0.3	7.3 ± 0.1	1.9 ± 0.1
Data observed	430 ± 20.7	110 ± 10.6	31 ± 5.6	8 ± 2.8	2 ± 1.4

Table 5.4. Number of events expected from MonteCarlo and observed in data for several inclusive jet multiplicities for the $Z \rightarrow \mu^+ \mu^-$ selection. The MC samples are normalized to the (N)NLO cross section,s with the exception of QCD which is normalized to the cross-section provided by PYTHIA. The number of predicted events is then normalized to the integrated luminosity of the data sample. Only statistical errors are considered.

Figure 5.2 shows the distribution of the invariant mass of the two selected muons for events with at least one selected jet. The Z boson peak is clearly visible in the data, and the total number of selected events is in good agreement with the MC expectations. Nevertheless the peak is visibly larger in data than in MC, which reflects the effect of the worse muon resolution in data, as already discussed in section 4.2. On the other hand the MC predicts with a good accuracy the shape of the Z boson p_T distribution, as shown in figure 5.3. In figure 5.4 the number of selected events as a function of the number of jets in the event, data and MC, is also reported. The agreement between data and MC is good.

5.5 Efficiency Corrections

As explained in section 3.1.1, to measure the cross-section it is necessary to correct the di-muon distributions for the selection efficiency.

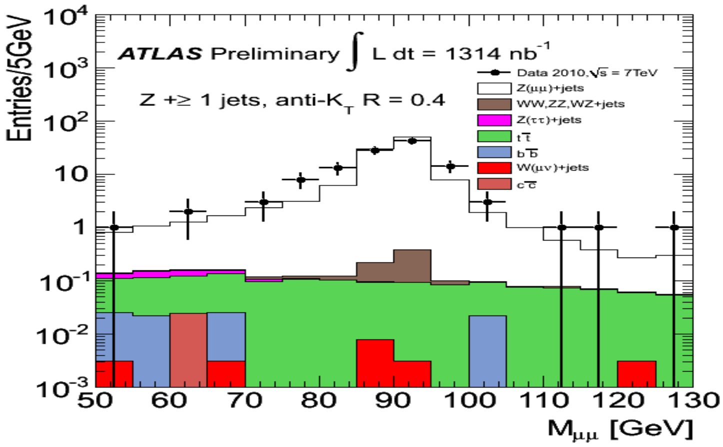

Figure 5.2. Distribution of the di-muon mass from data (dots) and MC simulation (filled histograms) for $Z \rightarrow \mu^+ \mu^-$ events with at least one jet in the event.

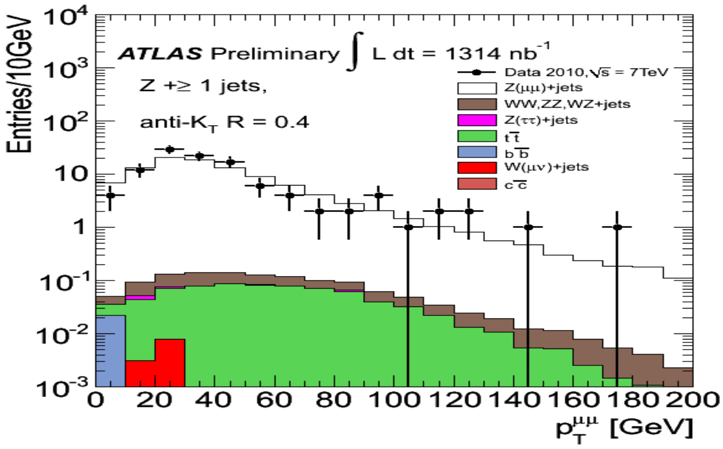

Figure 5.3. Distribution of the p_T of the Z boson, from data (dots) and MC simulation (filled histograms), for $Z \rightarrow \mu^+ \mu^-$ events with at least one jet in the event.

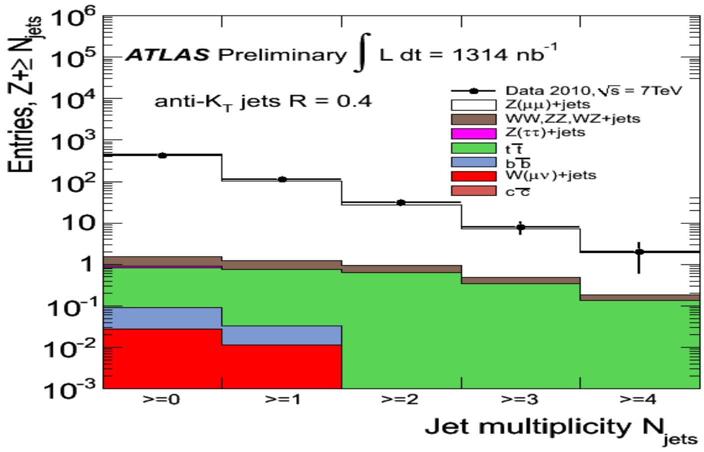

Figure 5.4. Distribution of selected $Z \rightarrow \mu^+ \mu^-$ events vs the inclusive jet multiplicity in the event.

The selection efficiency (ϵ_{sel}) is calculated from PYTHIA and using the generated events as reconstructed after full detector simulation. The denominator is the number of events passing the generator-level requirements, and the numerator is the number of events passing the full analysis selection. The uncorrected value of ϵ_{sel} is estimated to be

$$\epsilon_{sel} = 0.78 \pm 0.02$$

The systematic error of 2.5% derived by the difference found in the ϵ_{sel} using two different generators Alpgen e Sherpa. This factor is then corrected to take into account the difference between the real detector performance and the MC expected ones, via the scale factor (SF). In the evaluation of this SF, corrections for each selection step would need to be taken into accounted (event selection, trigger...). In this thesis we will only focus on the corrections coming from the muon identification and trigger.

In order to calculate the muon SF we need to combine the reconstruction (ϵ^R) and trigger (ϵ^T) efficiencies estimated in the previous chapter and summarized in table 5.5.

Summary of Reconstruction and Trigger Efficiencies

Type	Data Efficiency	MC Efficiency
Reconstruction	0.91 ± 0.01 (stat) ± 0.02 (syst)	0.9511 ± 0.0005 (stat) ± 0.016 (syst)
Trigger	0.83 ± 0.01 (stat) ± 0.01 (syst)	0.9142 ± 0.0006 (stat) ± 0.016 (syst)

Table 5.5. Summary of L1_MU10 relative trigger efficiency and reconstruction efficiencies from data and MC. The values are integrated over a range $|\eta| < 2.4$.

As a first correction and due to the limited statistics available we use an average value for both scale factors, integrated over a range $|\eta| < 2.4$. Combining the reconstruction and trigger efficiencies of both selected muons, we obtain a scale factor (SF) of:

$$\mathrm{SF} = \frac{\epsilon_1^R \cdot \epsilon_2^R \cdot (1-(1-\epsilon_1^T)(1-\epsilon_2^T))|_{data}}{\epsilon_1^R \cdot \epsilon_2^R \cdot (1-(1-\epsilon_1^T)(1-\epsilon_2^T))|_{MC}} = 0.90 \pm 0.03$$

Using this SF to correct the selection efficiency obtained from the MC studies, we get the final correction factor ϵ_{tot}:

$$\epsilon_{tot} = \epsilon_{sel} \cdot \mathrm{SF} = 0.70 \pm 0.02$$

The uncertainty on the SF is derived from the uncertainties on the trigger and reconstruction efficiencies, taking into account both the statistic and systematic uncertainties summarized in table 5.5. This uncertainty is then linearly combined with the uncertainty on ϵ_{sel} to get the final uncertainty on the efficiency correction factor. An additional systematic uncertainty is added, which is different for each jet multiplicity, due to the fact that we are neglecting the jet dependence in the SF computation. These systematics have been derived in section 4.3.3 and reported in table 5.6.

Additional Systematic Uncertainties on SF					
Affected Component	$Z+\geq 0$ jet	$Z+\geq 1$ jet	$Z+\geq 2$ jet	$Z+\geq 3$ jet	$Z+\geq 4$ jet
ϵ^R [%]	-	0.2	0.9	0.1	0.3
ϵ^T [%]	-	0.1	0.2	0.2	0.2
$\delta SF/SF$	0.016	0.027	0.072	0.027	0.038

Table 5.6. Additional systematic uncertainties on the SF to be added when neglecting the efficiencies dependence on the jet multiplicity.

5.6 Background Estimation

The QCD background estimation from data is done via a template method. The idea is to calculate from MC the ratio between the number of QCD events passing the standard di-muon selection explained in section 5.3, and those events passing the same selection but with reverted isolation cut, i. e. with the two muons having a tracker isolation greater than 1.8 GeV in a cone 0.2 (*anti-isolation*). Then the number of events passing the anti-isolation selection is measured from data and corrected by the ratio estimated from MC to get the number of QCD events passing the standard selection.

The $b\bar{b}$ MC sample is used to approximate the shape distribution of the QCD background for this study, because it dominates the anti-isolated distribution, as can be seen in figure 5.5. The ratio between the number of events passing the isolated selection over the anti-isolated selection is found to be $\mathrm{N}_{iso}/\mathrm{N}_{anti-iso} = 0.023 \pm 0.013$. The number of selected events with the anti-isolation in data is 4, which translates into a QCD estimate of $\mathrm{N}_{QCD} = 0.09 \pm 0.07$. This result is comparable to the expected number of QCD events from MC, which is $\mathrm{N}_{QCD} = 0.07 \pm 0.04$ (table 5.4).

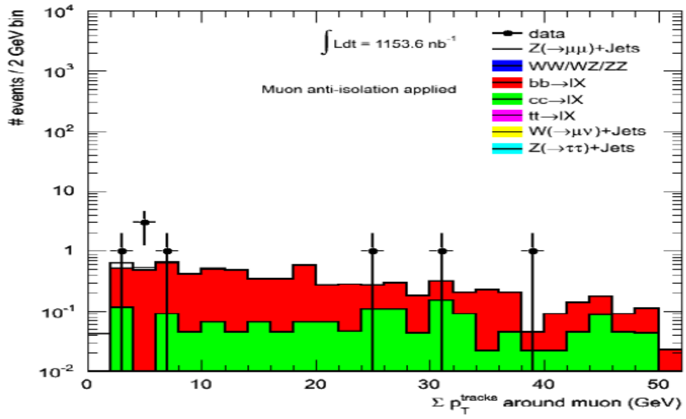

Figure 5.5. Distribution of the muon isolation variable in a cone 0.2 in data and MC, for muons with the anti-isolation requirements. The distribution is dominated by the $b\bar{b}$ background, which is then chosen to approximate the shape of the QDC background.

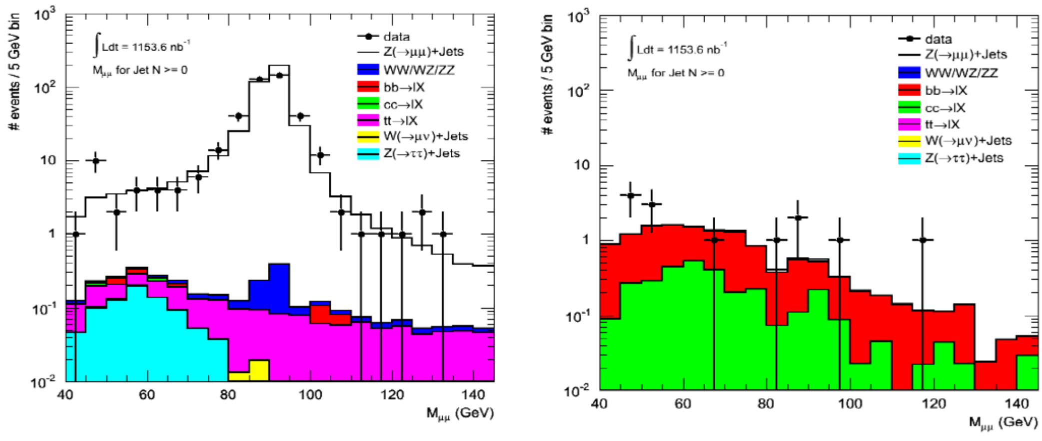

Figure 5.6. Distribution of the di-muon mass from data (dots) and MC simulation (filled histograms) for the $Z \rightarrow \mu^+ \mu^- +$ jets selection with the usual isolation requirement (left) and with the anti-isolation requirement (right).

However the non-QCD backgrounds are not estimated with this method, so in the end, considering this and the limited statistic available, the total background estimate for this cross-section measurement is taken from the MC, as reported in table 5.4.

5.7 Cross-Section

Putting together all the evaluated components of the analysis, summarized in table 5.7, we can finally calculate the cross-section for the process in the fiducial region σ^{fid}, as:

$$\sigma^{fid} = \frac{N_{sel} - N_b}{L \cdot \epsilon_{tot}}$$

Here the fiducial region is defined as that containing two muons with p_T greater than 15 GeV in $|\eta| < 2.4$ and at least one jet of 20 GeV in a pseudo-rapidity range of $|\eta| < 2.8$.

Inclusive $Z \rightarrow \mu^+ \mu^-$ Cross-sections Components					
	$Z+ \geq 0$ jet	$Z+ \geq 1$ jet	$Z+ \geq 2$ jet	$Z+ \geq 3$ jet	$Z+ \geq 4$ jet
Selected events	430 ± 21	110 ± 11	31 ± 6	8 ± 3	2 ± 1
Background	1.56 ± 0.05	1.26 ± 0.03	1.01 ± 0.05	0.54 ± 0.05	1.41 ± 0.03
Total Efficiency	0.70 ± 0.02	0.70 ± 0.03	0.70 ± 0.07	0.70 ± 0.03	0.70 ± 0.04
Luminosity [pb^{-1}]	1.32 ± 0.15	1.32 ± 0.15	1.32 ± 0.15	1.32 ± 0.15	1.32 ± 0.15

Table 5.7. Summary of $Z \rightarrow \mu^+ \mu^-$ cross-section components, evaluated with 1.3 pb^{-1}. The background contribution is estimated from MC, while the efficiency correction is estimated from MC but corrected for the SF between data and MC trigger and reconstruction efficiency as explained in the text. The estimated uncertainty on the luminosity is 11%.

The resulting differential $Z \rightarrow \mu^+ \mu^-$ cross-section values, as a function of the inclusive jet multiplicity in the event, in the fiducial region, are reported in table 5.8. For comparison the MC expectations are also reported. In this case only the systematic uncertainties due to the efficiency factor ϵ_{sel} are included. From the table results an excess in the data cross-sections, which is more evident in the events with at least 1 or 2 jets, as can be noticed from figure 5.7. This discrepancy has to be further investigated in more detail. Anyhow we want to remark that this is a detector-level comparison, where no un-folding correction to the parton-level are applied, which could modify the agreement. Moreover no systematic errors due to theoretical uncertainties on the MC cross-sections have been evaluated yet, which can again modify the agreement with the data and no NNLO corrections have been taken into account, which can shift the central values of the cross-section.

These studies are actually on-going and a more detailed comparison is expected to be performed with the full 2010 data sample, with an integrated luminosity of 42 pb^{-1}, in the next few weeks.

$Z \rightarrow \mu^+ \mu^-$ **Cross-sections**
DATA 1.3 pb^{-1}
$\sigma^{fid}(Z \rightarrow \mu^+\mu^- + \geq 0jets) = 464 \pm 21(\text{stat}) \pm 14(\text{syst}) \pm 51(\text{lumi})$ pb
$\sigma^{fid}(Z \rightarrow \mu^+\mu^- + \geq 1jets) = 118 \pm 11(\text{stat}) \pm 4.4(\text{syst}) \pm 13(\text{lumi})$ pb
$\sigma^{fid}(Z \rightarrow \mu^+\mu^- + \geq 2jets) = 32 \pm 6(\text{stat}) \pm 2.5(\text{syst}) \pm 4(\text{lumi})$ pb
$\sigma^{fid}(Z \rightarrow \mu^+\mu^- + \geq 3jets) = 8.1 \pm 2.8(\text{stat}) \pm 0.3(\text{syst}) \pm 0.9(\text{lumi})$ pb
$\sigma^{fid}(Z \rightarrow \mu^+\mu^- + \geq 4jets) = 0.6 \pm 1.4(\text{stat}) \pm 0.03(\text{syst}) \pm 0.07(\text{lumi})$ pb
MC Expectations
$\sigma^{fid}(Z \rightarrow \mu^+\mu^- + \geq 0jets) = 436 \pm 11(\text{syst})$ pb
$\sigma^{fid}(Z \rightarrow \mu^+\mu^- + \geq 1jets) = 98.5 \pm 2.6(\text{syst})$ pb
$\sigma^{fid}(Z \rightarrow \mu^+\mu^- + \geq 2jets) = 25.78 \pm 0.69(\text{syst})$ pb
$\sigma^{fid}(Z \rightarrow \mu^+\mu^- + \geq 3jets) = 6.56 \pm 0.18(\text{syst})$ pb
$\sigma^{fid}(Z \rightarrow \mu^+\mu^- + \geq 4jets) = 0.48 \pm 0.05(\text{syst})$ pb

Table 5.8. Summary of $Z \rightarrow \mu^+ \mu^-$ cross-sections vs the inclusive jet multiplicity in the event, in the fiducial region $|\eta| < 2.4$.

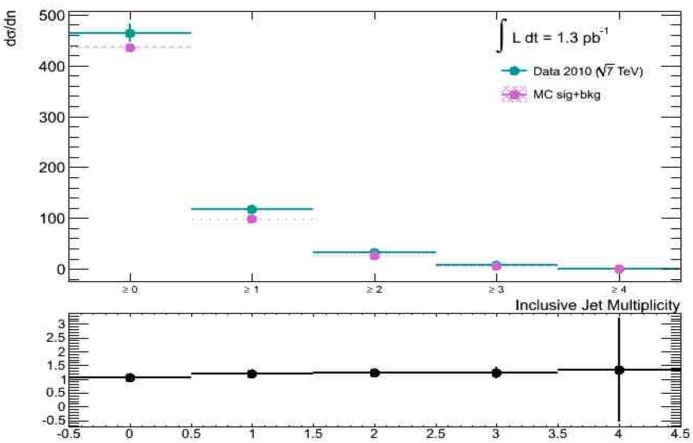

Figure 5.7. $Z \rightarrow \mu^+ \mu^-$ differential cross-section vs jet multiplicity in the event at the detector-level, data and MC (signal plus background). Statistic and systematic uncertainties are reported for data. Only systematic error due to reconstruction efficiency is reported for MC.

Chapter 6

Conclusions

The observation of the $pp \rightarrow Z \rightarrow \mu^+\mu^-$ process is a fundamental step towards all the precision and new physics measurement at LHC, because this is used as a standard candle both for detector performance assessment and tuning of theoretical predictions of processes at 7 TeV center of mass energy.

In this thesis it has been shown how this process can be used to measure muon reconstruction and trigger efficiencies from data. To this aim, a Tag&Probe method has been developed and optimized in the past years using the MC simulations, showing that $\sim 2\%$ of statistical precision can be reached on the measurement with a data integrated luminosity of 1 pb^{-1}, with less than 1% of background contamination.

In the first five months of data-taking, the ATLAS detector collected about 1.3 pb^{-1} of integrated luminosity. Using this data sample a the first muon efficiencies have been measured with the Tag&Probe method and have been compared with the MC expectations. The reconstruction efficiencies show a discrepancy of $\sim 4\%$ from the expectations, while the trigger efficiencies show a discrepancy of $\sim 9\%$ overall, being this discrepancy mainly concentrated in the End-Cap regions.

Preliminary studies on the background contamination to this measurement show that a data-driven method has to be developed to estimate the background from data. In fact a contamination larger than the MC expected one has been found in the low-p_T region (below 20 GeV).

The efficiencies have been then used to derive the data/MC scale factor needed for the $Z \rightarrow \mu^+ \mu^-$ cross-section measurement. A first estimation of both inclusive and differential cross-sections with respect to the jet multiplicity in the event, has been shown with the same 1.3 pb^{-1} data sample, in a fiducial region defined by two muons with p_T greater than 15 GeV in $|\eta| < 2.4$ and at least one jet of 20 GeV in a pseudo-rapidity range of $|\eta| < 2.8$. The particle-level comparison with the MC expectations has been presented, but before concluding anything, all the theoretical uncertainties on the MC predictions have to be studied in detail. This work is on-going and will profit of the whole 42 pb^{-1} data sample recorded in the 2010.

In conclusion this is the performance assessment of the ATLAS detector has started and the re-discovery of the Standard Model physics have already produced interesting results, which will help to tune the MC predictions at a new unexplored energy. The first step towards the new physics to be discovered.

Bibliography

[1] M.E. Peskin, D.V. Schroeder, *"An introduction to quantum field theory"*, Addison-Wesley (1995) 842 p.

[2] ALEPH Collaboration, CDF Collaboration, D0 Collaboration, DELPHI Collaboration, L3 Collaboration, OPAL Collaboration, SLD Collaboration, LEP Electroweak Working Group, Tevatron Electroweak Working Group, SLD electroweak heavy flavour groups, *"Precision Electroweak Measurements and Constraints on the Standard Model"*, arXiv:0911.2604v2 [hep-ex]

[3] K. Nakamura et al. (Particle Data Group), J. Phys. G **37**, 075021 (2010)

[4] S.D. Drell, T.M. Yan, *"Massive Lepton-Pair Production in Hadron-Hadron Collisions at High Energies"*, PRL **25**, 316-320 (1970).

[5] J. D. Bjorken and E. A. Paschos, *"Inelastic Electron-Proton and γ-Proton Scattering and the Structure of the Nucleon"*, Phys. Rev. **185**, 1975-1982 (1969).

[6] W. L. van Neerven and E. B. Zijlstra, Nucl. Phys. B **382** (1992) 11 [Erratum-ibid. B **680** (2004) 513].

[7] C. Anastasiou, L. Dixon, K. Melnikov, and F. Petriello, *"High-precision QCD at hadron colliders: electroweak gauge boson rapidity distributions at NNLO"*, Phys. Rev. D69 (2004) 094008.

[8] T. Becher, M. Neubert and G. Xu, JHEP **0807**, 030 (2008) [arXiv:0710.0680 [hep-ph]].

[9] M. Bonvini, S. Forte and G. Ridolfi, arXiv:1009.5691 [hep-ph].

[10] S. Catani, G. Ferrera and M. Grazzini, JHEP **1005** (2010) 006 [arXiv:1002.3115 [hep-ph]].

[11] A. D. Martin, W. J. Stirling, R. S. Thorne, and G. Watt, *"Parton distributions for the LHC"*, Eur. Phys. J. C63 (2009) 189-285.

[12] G.Aad et al. The ATLAS Collaboration, *"The ATLAS experiment at the CERN Large Hadron Collider"*, JINST 3: S08003,2008.

[13] , ATLAS Collaboration, *"Readiness of the ATLAS Liquid Argon Calorimeter for LHC Collisions."*, arXiv:0912.2642 [physics.ins-det]

[14] , ATLAS Collaboration, *"Readiness of the ATLAS Tile Calorimeter for LHC Collisions."*, arXiv:1007.5423v1 [physics.ins-det]

[15] M. Cacciari, G. Salam, and G. Soyez, *"The anti-kt jet clustering algorithm"'*, JHEP 0804 (2008) 063, arXiv:0802.1189.

[16] T. Sjostrand, S. Mrenna, and P. Z. Skands, *"PYTHIA 6.4 Physics and Manual"*, JHEP 05 (2006) 026.

[17] A. Sherstnev and R. S. Thorne, *"Parton Distributions for LO Generators"*, Eur. Phys. J. C55 (2008) 553.

[18] The GEANT4 Collaboration, S. Agostinelli et al., *"GEANT4: A simulation toolkit"*, Nucl. Instrum. Meth. A506 (2003) 250.

[19] S. Frixione, P. Nason, and C. Oleari, *"Matching NLO QCD computations with Parton Shower simulations: the POWHEG method"*, JHEP 11 (2007) 070.

[20] A. D. Martin, W. J. Stirling, R. S. Thorne, and G. Watt, *"Parton distributions for the LHC"*, Eur. Phys. J. C63 (2009) 189-285.

[21] ATLAS Collaboration, G. Aad et al., *"ATLAS Monte Carlo tunes for MC09"*, Tech. Rep. ATL-PHYS-PUB-2010-002, CERN, Geneva, Mar, 2010.

[22] M.L. Mangano, M. Moretti, F. Piccinini, R. Pittau and A. Polosa, JHEP **0307** (2003) 001.

[23] S. Frixione, B.R. Wbber, arXiv:hep-ph/0307146v1

[24] JHEP02 (2009) 007

[25] ATLAS Collaboration, *"Measurement of the W -> lnu and Z/gamma* -> ll production cross sections in proton-proton collisions at sqrt(s) = 7 TeV with the ATLAS detector"*, arXiv:1010.2130 [hep-ex], submitted to JHEP (Oct. 11, 2010)

[26] ATLAS Collaboration, *"Measurement of the cross section for jets produced in association with Z bosons"*, ATL-COM-PHYS-2010-884